

Creating CliffSat

Adapting a satellite-derived shoreline algorithm for monitoring coastal cliff erosion

MSc Thesis Hydraulic Engineering
Jelle Freund

Delft University of Technology

Creating CliffSat

Adapting a satellite-derived shoreline
algorithm for monitoring coastal cliff erosion

by

Jelle Freund

TU Delft supervisor:	Dr. Ir. S. de Vries Dr. Ir. J. Timmermans
Haskoning supervisor:	R. Hoegen J. Woerdman
Project Duration:	April, 2025 - August, 2025
Faculty:	Faculty of Civil Engineering and Geo-sciences Delft University of Technology

Cover: Front view of ocean in day light - Freepik

Preface

This thesis represents the final step of my Master's in Hydraulic Engineering and the conclusion of my journey at Delft University of Technology. More than that, it marks the end of my time as a student in Delft.

In my early years here, I was searching for my true passion. During my Bachelor's graduation project, I discovered that this passion lies at the beach. Testing a construction to monitor wave conditions in the surf zone was far outside my comfort zone, but it was an experience I'll never forget. My interest in coastal environments was reaffirmed during my Master's, especially after the first lectures in Coastal Systems—learning about the complex interplay of processes at the beach truly blew my mind.

While searching for a thesis topic, I came across a fascinating project at Haskoning focused on cliff coasts. Since the Master's program primarily emphasizes sandy and muddy coasts, I saw this as a unique opportunity to explore a less familiar coastal environment. What began as a study into the effects of cliffs on the surrounding coastal system quickly evolved into the development of a tool for monitoring coastal cliffs, bringing along new challenges and insights. This thesis reflects a five-month journey that has deepened my understanding of my strengths as an engineer.

I would like to sincerely thank my university supervisors for their guidance throughout this project. Sierd, thank you for the engaging conversations that helped shape the project and for always keeping your door open for my short questions. Joris, I'm grateful that you chose to join the project and for your involvement over the past months — I've learned a great deal from your expertise in remote sensing. Both of you significantly elevated the scientific quality of this thesis.

During my thesis, I was warmly welcomed by Haskoning into the Maritime and Renewables group. The enthusiasm of everyone made going to the office both insightful and enjoyable. A special thanks to Roel and Jelle, who guided me throughout my time at Haskoning. I'm truly impressed by your expertise, and your contributions — both in shaping the project and thinking along with me — were invaluable. Roel, I especially appreciate the time you took each week to discuss my progress.

Finally, I would like to thank my family and friends for their support. In particular, Megan — not only for your encouragement during these months, but also for turning some of my ideas into visuals that greatly enhanced the report. And to my fellow hydraulic engineering friends, it was a pleasure to share this period with you — our coffees, lunches, and thesis discussions made the journey all the more enjoyable.

*Jelle Freund
Delft, August 2025*

Abstract

Coastal cliffs make up over half of the world's shorelines and are susceptible to irreversible erosion. Despite their global prevalence and increasing vulnerability due to sea level rise and coastal development, large-scale and long-term monitoring of cliff retreat remains limited. Traditional measurement methods such as LiDAR and GPS surveys are accurate but costly, labor-intensive, and geographically constrained. Satellite imagery offers a scalable and cost-effective alternative, yet existing algorithms are primarily designed for sandy coastlines and are not suitable for cliff environments.

This study investigates the potential of satellite imagery to monitor cliff erosion by adapting an existing Satellite-Derived Shoreline (SDS) algorithm, CoastSat, into a Satellite-Derived Cliff (SDC) algorithm, CliffSat, answering the main research question: 'How can satellite-derived shoreline detection methods be adapted and applied to extract coastal cliff erosion, and how do these satellite-based measurements compare to in-situ erosion data?'

To address this, CoastSat was modified by incorporating a combined spectral index (NDVI and SwiRed) to distinguish cliff tops from sandy foreshores and other land types. Additionally, composite imagery was used to reduce noise, leveraging the relative stability of cliff lines compared to dynamic shorelines. The algorithm was validated along the Holderness Coast in England — a 60 km stretch of rapidly eroding clay cliffs with biannual in-situ measurements.

Validation was conducted using both single satellite images and yearly composite images. The algorithm's performance was assessed by comparing satellite-derived erosion trends (via linear regression) and total erosion amounts against in-situ data.

- Erosion Trends: Both methods showed similar performance, with a bias of -0.1 meters/year and a standard deviation of 0.7 meters/year — well within acceptable limits (bias < 0.3 meters/year, standard deviation < 0.7 meters/year).
- Total Erosion: The composite method had a slightly higher bias (-0.6 meters) than the single-image method (-0.3 meters), but a notably lower standard deviation (4.7 meters vs. 5.5 meters), especially when recorded erosion was below 10 meters. These results fall within acceptable thresholds derived from other SDS algorithms (bias < 3 meters, standard deviation < 7 meters).

These findings demonstrate that satellite imagery can be effectively used to monitor cliff erosion, with the adapted algorithm performing as well as — or better than — established shoreline detection models. Future research should focus on validating the algorithm across diverse cliff types, exploring alternative spectral indices, and integrating elevation data to enhance accuracy. Additionally, the use of higher resolution satellite imagery may further improve performance, particularly in areas with complex land cover or high erosion rates.

Contents

Preface	i
Abstract	ii
Nomenclature	v
1 Introduction	1
1.1 Context	1
1.2 Knowledge gap	2
1.3 Objective and scope	2
1.4 Research Questions	2
1.5 Research Structure	3
2 Literature review	4
2.1 Coastal cliff erosion processes	4
2.2 Monitoring techniques for coastal applications	6
2.3 Satellite observation missions	8
2.4 Satellite-derived shoreline methods	9
2.5 Spectral indices	12
2.6 Principles and workflow of CoastSat	13
3 Methodology	15
3.1 Development of the satellite-derived cliff line algorithm	15
3.2 Case study: the Holderness Coast	16
3.3 Data processing and collection	17
3.4 Validation criteria	18
4 Results	19
4.1 Outcomes of the satellite-derived cliff line algorithm	19
4.1.1 Spectral index evaluation	19
4.1.2 Creating composite images	24
4.1.3 Overview of workflow	28
4.2 Validation of the algorithm	29
4.2.1 General comparison of algorithms output to in-situ data	29
4.2.2 Comparison of output and data per erosion rate	31
4.2.3 Investigation of errors	32
5 Discussion	35
5.1 Reiteration and interpretation of the results	35
5.2 Reflection on methodological choices	36
5.3 Limitations and uncertainties	37
5.4 Applicability of CliffSat	38
5.5 Wider Contribution	39
6 Conclusion	40
7 Recommendations	42
7.1 Future research and development	42
7.2 Implementation of the algorithm	43
References	44
A Spectral index comparison	48

B	Comparison of the indices used in CoastSat and CliffSat	59
C	Evaluation of thresholding methods	62

Nomenclature

Abbreviation	Definition
BI	Bareness Index
BRBA	Band Ratio for Built-up Area
BSI	Bare Soil Index
DBSI	Dry Bare-Soil Index
ERYC	East Riding of Yorkshire Council
GEE	Google Earth Engine
GPS	Global Positioning System
INDBI	Improved Normalized Difference Built-up Index
LiDAR	Light Detection and Ranging
MNDWI	Modified Normalized Difference Water Index
MSL	Mean Sea Level
NBI	New Built-up Index
NDBI	Normalized Difference Built-up Index
NDVI	Normalized Difference Vegetation Index
NDWI	Normalized Difference Water Index
NIR	Near-Infrared
PDF	Probability Density Function
RGB	Red–Green–Blue
RTK-GPS	Real-Time Kinematic Global Positioning System
SDC	Satellite-Derived Cliff
SDS	Satellite-Derived Shoreline
SWIR	Short-Wave Infrared
VNIR	Visible and Near-Infrared
SwiRed	SWIR–Red Index

Introduction

This chapter introduces the research context, knowledge gap and objectives of the study, leading to the formulation of the research questions. Finally, the chapter presents the proposed structure of the research.

1.1. Context

Coastal regions are highly urbanized land areas, accommodating approximately three billion people worldwide (Bosboom & Stive, 2023). There is a high variability in types of coastal landforms, such as sandy coasts, river deltas, tidal flats, barrier islands, and cliffs (Luijendijk et al., 2018). In this research, the focus is on coastal cliffs, which are present along approximately 52% of the world's coastlines (Young & Carilli, 2019), with high amounts located in for example the west coast of North-America and South-America, and in countries like Japan, New-Zealand and Australia, as can be seen in figure 1.1.

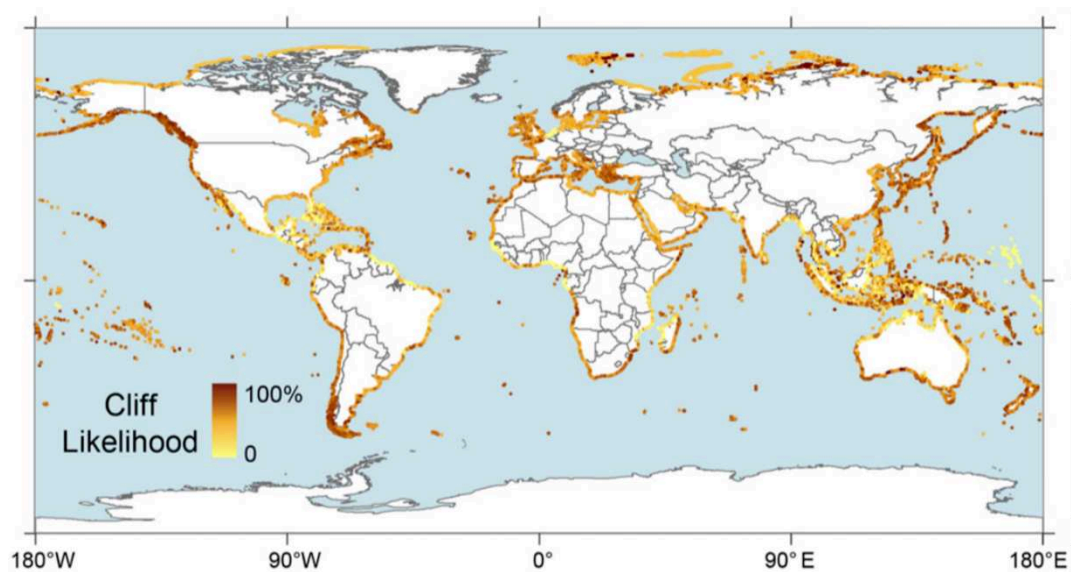


Figure 1.1: A global map of cliff likelihood for coasts around the world, with a brown color representing a high likelihood and a yellow color a low likelihood (Young & Carilli, 2019).

Whereas sandy coasts are able to (slowly) recover after an erosive event (Burvingt & Castelle, 2023), erosion is permanent for coastal cliffs. In recent years, increasing amounts of news articles are reporting cliff erosion, with people losing their homes to the sea in for example England (NOS, 2022), France (NOS, 2023), California (Los Angeles Times, 2022) and Australia (Great Ocean Road Coast and Parks Authority, 2024). Rising sea levels and growing coastal populations are expected to exacerbate these challenges (Dawson et al., 2009).

While extensive research and global databases exist for sandy coastlines (Luijendijk et al., 2018), similar long-term, systematic datasets for cliff coasts are largely absent. Engineering firms like Haskoning have an increasing interest in these kind of datasets, as more people are under threat of cliff erosion. It also shows to be valuable information for how far inland for example cables for offshore wind farms must be installed to prevent them from being exposed. Data is especially scarce in remote or economically constrained regions.

1.2. Knowledge gap

Although high-resolution methods like LiDAR drone surveys and GPS-measurements can accurately measure cliff retreat, they are expensive, labor-intensive, or geographically limited (Westoby et al., 2018). These limitations hinder their use for long-term and large-scale monitoring, particularly in remote or economically constrained regions (Bird, 2008), and the only studies that exist measure either on a short-term or with a coarse temporal resolution (C. S. Earlie et al., 2015; Obu et al., 2017; Swirad & Young, 2022; Young et al., 2021). Therefore, there is a need for alternative approaches that are globally scalable, cost-effective, and capable of capturing long-term trends.

Optical satellite imagery presents a largely untapped potential for the long-term monitoring of cliff retreat. Since the 1980s, global archives of open source satellite imagery have been available (European Space Agency, 2025; Gorelick et al., 2017; NASA, 2025), enabling consistent temporal analysis over multiple decades. Recent developments in image classification and index-based shoreline detection have contributed to a rapid increase of available satellite-derived shoreline (SDS) algorithms (Almeida et al., 2021; Luijendijk et al., 2018; Mao et al., 2021; Sánchez-García et al., 2020; Vos et al., 2019), being able to distinguish water from land, and therefore creating a coastline. However, since cliffs are not always adjacent to water, these algorithms do not work for these cliffs.

One of the SDS-algorithms, CoastSat (Vos et al., 2019), has already been altered using a different index to determine the waterline for a vegetated shore (Lanza et al., 2023), which shows the potential to alter existing algorithms for cliff monitoring. However, such approaches have not yet been thoroughly validated or systematically implemented for cliff monitoring.

1.3. Objective and scope

The objective of this research is to:

'Develop a satellite-derived cliff line algorithm to assess coastal cliff erosion rates on a large spatial scale.'

The scope can be divided into the following items:

- Topic: This research focuses exclusively on coastal cliffs, as these areas are prone to erosion but few research has been done on large spatial - and time scales.
- Geographical: To validate the cliff line detection algorithm, in-situ data from the Holderness Coast in England is used. This case study is introduced in Chapter 3.2.
- Temporal: The study uses both satellite and in-situ data from 2015 to 2025, considering there is consistent imagery from Sentinel-2 available.

1.4. Research Questions

From the research gaps, the main research question for this research is formulated:

'How can satellite-derived shoreline detection methods be adapted and applied to extract coastal cliff erosion, and how do these satellite-based measurements compare to in-situ erosion data?'

From this research question, the following sub-questions are defined:

- What are the principles and techniques of current satellite-derived shoreline detection methods?
- How can satellite-derived shoreline detection methods be adapted for cliff line extraction?
- How accurate is satellite-derived cliff erosion compared to in-situ data?
- What factors influence the accuracy of a satellite-derived cliff line detection method?

1.5. Research Structure

The structure of this research is as follows:

- Chapter 2, Theory: Explores existing knowledge on cliff erosion processes and available monitoring techniques, with a focus on optical satellite-derived shoreline methods.
- Chapter 3, Methodology: Details the approach used to address the research questions, including the methods for modifying and validating the cliff line detection tool.
- Chapter 4, Results: Presents the key findings in relation to the research questions.
- Chapter 5, Discussion: Evaluates the research outcomes, outlines its limitations, and provides the applicability and wider contribution of the research.
- Chapter 6, Conclusion: Summarizes the main findings and provides direct answers to the research questions.
- Chapter 7, Recommendations: Offers suggestions for future research directions and how the algorithm can be implemented in the engineering and research field.

2

Literature review

In this chapter, the theoretical background of topics relevant to this research is explored. This is done by conducting a literature review on the processes responsible for coastal cliff erosion, the available tools to monitor these processes, the principles of satellite imagery and satellite-derived shoreline algorithms, an investigation in spectral indices and the functioning of a tool named CoastSat for processing satellite-derived shorelines.

2.1. Coastal cliff erosion processes

Coastal cliffs erode due to a combination of marine and subaerial processes (Emery & Kuhn, 1982). Marine forcing causes erosion through several mechanisms. Hydraulic action and wave quarrying occur when the energy released by breaking waves is sufficiently large to loosen rock from the cliff (Hall et al., 2008). Additionally, abrasion contributes to cliff erosion as stones or sediments carried by the water impact the cliff face due to wave energy (Kline et al., 2014). These processes reinforce each other, as loosened rock caused by wave quarrying can dislodge additional material (Bird, 2016). The effects of these processes are most significant at the cliff foot and the lower part of the cliff face, depending on the water level, which is influenced by factors such as tides. During storms, significant erosion at the cliff foot due to marine forces can destabilize the top of the cliff face, leading to collapse. Subaerial processes, such as wind and rain, contribute to erosion at the upper parts of the cliff face through direct forcing and other mechanisms, including physical and chemical weathering and temperature fluctuations (C. Earlie et al., 2018). Finally, geophysical processes, such as earthquakes, can cause rapid, event-driven cliff erosion (Bloom et al., 2023). A visual overview of these erosive processes is provided in Figure 2.1.

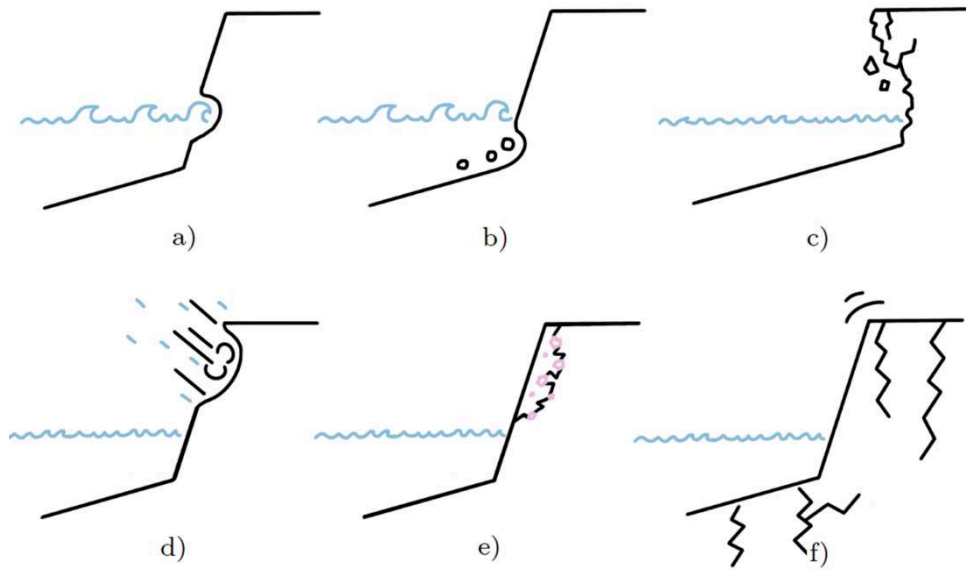


Figure 2.1: A visual representation of erosive processes. a) wave quarrying, b) abrasion, c) cliff face instability, d) physical weathering, e) chemical weather, f) earthquake.

The timescales over which these processes cause cliff erosion varies. Earthquakes and collapses due to instability can occur within seconds (Bloom et al., 2023), while hydraulic action and wave quarrying can cause substantial damage within hours (Swirad & Young, 2022). Abrasion, as well as physical and chemical weathering, are typically longer-term processes, acting over years or even decades (Kline et al., 2014).

The vulnerability of coastal cliffs to erosion depends on both their composition and exposure (Bird, 2016; Kline et al., 2014; Swirad & Young, 2022; Young et al., 2021; Yuan et al., 2024). Cliff composition can be categorized based on rock hardness, ranging from hard materials such as quartzites, sandstones, and granite to weaker mud rocks and unconsolidated sands (Bird, 2008). Generally, the harder and more resistant the rock, the steeper the slope of the cliff. In addition to composition, the exposure of the cliff plays a role in its vulnerability. For instance, if a cliff is situated in a shadow zone — where wave energy is reduced due to refraction or diffraction — the impact of marine forces is smaller, and the cliff erodes at a slower rate (Fellowes et al., 2022).

Table 2.1 presents the most dominant cliff erosion processes, including a brief description of each, the key variables influencing their severity, the types of cliffs most sensitive to each process, and the typical timescale over which each process occurs.

Process	Description	Sensitive cliff types	Drivers	Time scale	Spatial scale
Wave quarrying	Wave energy creates pressure differences, dislodging rocks from the cliff face.	Steep, rocky, high wave exposure cliffs.	Water level, wave forcing.	Hours to days (single storms)	Meters to kilometers
Abrasion	Sediments thrown against the cliff by waves scouring the cliff face.	Soft cliffs in sediment rich areas.	Sediment concentration and size, water level, wave forcing.	Days to years	Centimeters to meters
Mass movement (instability)	Loss of support at the cliff base makes cliff material collapse.	Steep, unsupported cliffs.	Undercutting, rock structure	Seconds (with long preparation time)	Meters to decameters
Physical weathering	Wind, rain and temperature changes causing erosion at the cliff face.	Soft, porous cliffs in variable climates.	Wind speed and direction, precipitation, temperature fluctuations.	Years to decades	Centimeters to meters
Chemical weathering	Chemical reactions causing erosion at the cliff face.	Carbonate rocks (like limestone) in humid coastal areas.	Rainfall acidity, moisture availability, rock mineralogy.	Years to centuries	Centimeters to meters
Earthquakes	Seismic activity that breaks of cliff material.	Steep cliffs in seismically active areas.	Seismic intensity.	Seconds to hours	Hectometers to kilometers

Table 2.1: Cliff erosion processes (Bird, 2016) - wave quarrying (Hall et al., 2008), abrasion (Kline et al., 2014), mass movement (Leisner et al., 2025), physical and chemical weathering (C. Earlie et al., 2018), earthquakes (Bloom et al., 2023) - with a description, key influencing variables, sensitive cliff types, and typical timescales.

All these processes contribute to cliff erosion solely, but their combined influence causes acceleration of erosion rates through feedback loops (Alessio & Keller, 2020). For example, weathering causes more vulnerability for wave action and abrasion, causing 'new' rock to reach the surface, that will start to weather.

2.2. Monitoring techniques for coastal applications

To determine if and how much a coast is eroding, monitoring is essential, and various techniques are currently in use. Historically, beach measurements were conducted using measuring rods, involving manual work on the beach (Emery, 1961). More recently, GPS devices have been employed to perform these measurements more easily and accurately (Harley et al., 2011). Through signals from orbiting satellites, the distance from a certain location to these satellites is obtained and therefore a precise location can be determined (Global GPS Systems, 2022). If a base point, of which the exact location is known, is combined with the GPS technology, the measurement error from the base station is used to improve the accuracy of the GPS data, resulting in a real-time kinematic GPS (RTK-GPS). RTK-GPS devices are used widely in coastal surveying studies (Aagaard et al., 2005; Harley et al., 2011; Larson & Kraus, 1995), by walking a grid with the device on, where it can either record every second or be installed to only measure a fixed point after a certain distance. The advantages are that a high accuracy can be reached while having a high spatial resolution, however due to the process being manual work it is labor intensive and therefore only a small spatial extend and a coarse temporal resolution is obtained (Baptista et al., 2011; Westoby et al., 2018).

Apart from manual monitoring techniques, remote sensing technologies exist and are being used on a global scale. A precise definition of remote sensing is: “The process of detecting and monitoring the physical characteristics of an area by measuring its reflected and emitted radiation at a distance” (U.S. Geological Survey, 2025b). Remote sensing technologies can be separated in three different groups; photogrammetry, LiDAR and satellite imagery (Vitousek et al., 2023; Westoby et al., 2018), where both photogrammetry and LiDAR can be executed from a fixed point or using airborne technologies.

Photogrammetry is the process where a series of photos are taken over a period of time, after which extensive processing leads to a 3D model of the area (Holman & Stanley, 2007). The photos can be obtained from a fixed point, a moving vehicle like a truck or a moving air vehicle like a drone (Harrison et al., 2017; Kregar & Kozmus Trajkovski, 2025; Pianca et al., 2015). The advantages are that the measurement are performed at a high accuracy and spatial resolution. Where the fixed photogrammetry can obtain a high temporal resolution but compromises on spatial extend, the aerial photogrammetry techniques have a low temporal resolution with a more extensive spatial extend (Vitousek et al., 2023). To generate accurate datasets, the equipment is expensive to acquire and it requires skill in processing (Westoby et al., 2018).

LiDAR is a monitoring technique that stands for ‘light detection and ranging’, that measures 3D profiles using active laser scanning (Weitkamp, 2005). LiDAR data can be obtained from a fixed point, but considering the spatial advantage it is generally obtained from an airborne vehicle like a plane or drone (C. S. Earlie et al., 2015; Middleton et al., 2013; Obu et al., 2017; Young et al., 2021). While LiDAR can generate accurate data on a fine spatial resolution, high costs are involved for purchase and maintenance (Vitousek et al., 2023; Westoby et al., 2018).

Where monitoring techniques like RTK-GPS, photogrammetry and LiDAR are all able to obtain a high accuracy on a fine spatial resolution but share disadvantages as high operating costs or a limited temporal resolution or small spatial extend, satellite imagery distinguished itself. Satellites fly around the world all of the time, acquiring weekly images of the whole world with a coarse spatial resolution of 1-30 meters (Pardo-Pascual et al., 2018). While the images of satellites with a relative fine spatial resolution of around 1 meter are expensive to buy, the images with a spatial resolution of 10-30 meters can be obtained freely (Gorelick et al., 2017). Using this, a dataset of coarse resolution data with weekly measurements is available for any region of interest.

In Table 2.2, a brief description, the spatial and temporal solution and the most important advantages and disadvantages of the above mentioned monitoring techniques are presented.

Monitoring technique	Description	Spatial resolution	Temporal resolution	Advantages	Disadvantages
GPS measurements	Repeated measurements of (fixed) ground points.	0.5 meters	Weeks to years	Accurate (5-10 cm)	Labor intensive, small spatial extend.
Fixed photogrammetry	Repeated photos from a fixed point.	0.5 meters	Minutes to hours	Accurate (1-2 m), low labour intensity.	Needs stable reference points, small spatial extend.
Aerial photogrammetry	Photos taken from planes or drones.	0.5 meters	Months to years.	Accurate (1-5 m), big spatial extend, low labour intensity.	Expensive, weather dependent.
Terrestrial LiDAR	Laser scanning from a fixed points to create 3D models	0.1 meters	Months to years	Accurate (0.5 m), low labour intensity	
Airborne LiDAR	Laser scanning to create 3D models.	0.1 meters	Months to years	Accurate (0.5 m), big spatial extend, low labour intensity.	Expensive
Satellite imagery	Use optical or radar data from satellites.	1-30 meters	Days to weeks	Cheap, global spatial extend, much historical data available, easy worldwide access.	Inaccurate (1-30 m).

Table 2.2: Monitoring techniques for coastal erosion, based on Vitousek et al. (2023) and Westoby et al. (2018). RTK-GPS (Aagaard et al., 2005; Larson & Kraus, 1995); Fixed photogrammetry (Holman & Stanley, 2007; Pianca et al., 2015); Aerial photogrammetry (Ford, 2013; Harrison et al., 2017); Airborne LiDAR (Middleton et al., 2013); Satellite imagery (Pardo-Pascual et al., 2018).

Some additional disadvantages are particularly relevant when focusing on cliff erosion. For example, it is dangerous — and sometimes impossible — for people to perform RTK-GPS measurements on the cliff face or near the cliff edge, while airborne photogrammetry and LiDAR both have difficulty to resolve near-vertical topography (Westoby et al., 2018).

Using satellite imagery for monitoring does not suffer from these limitations. Furthermore, it eliminates the risks of vandalism and logistical constraints, and since the 1980s, satellites have been capturing images of the Earth on a bi-weekly basis (U.S. Geological Survey, 2025a), which ensures the availability of long-term historical data. Although the spatial resolution is relatively coarse, satellite imagery enables long-term monitoring of coastlines and the identification of shoreline movement trends. Additionally, satellite data was used to classify coastal regions in the research by Luijendijk et al. (2018), opening the field of coastal science to big data approaches.

Comparing monitoring techniques to coastal change processes, as shown in Figure 2.2, further highlights the potential of satellite imagery for monitoring coastal cliffs. As illustrated, the temporal and spatial scales of satellite imagery largely overlap with those of cliff erosion. Especially for short- to medium-term trends — on the order of decades or less — satellite imagery offers valuable opportunities for large-scale monitoring.

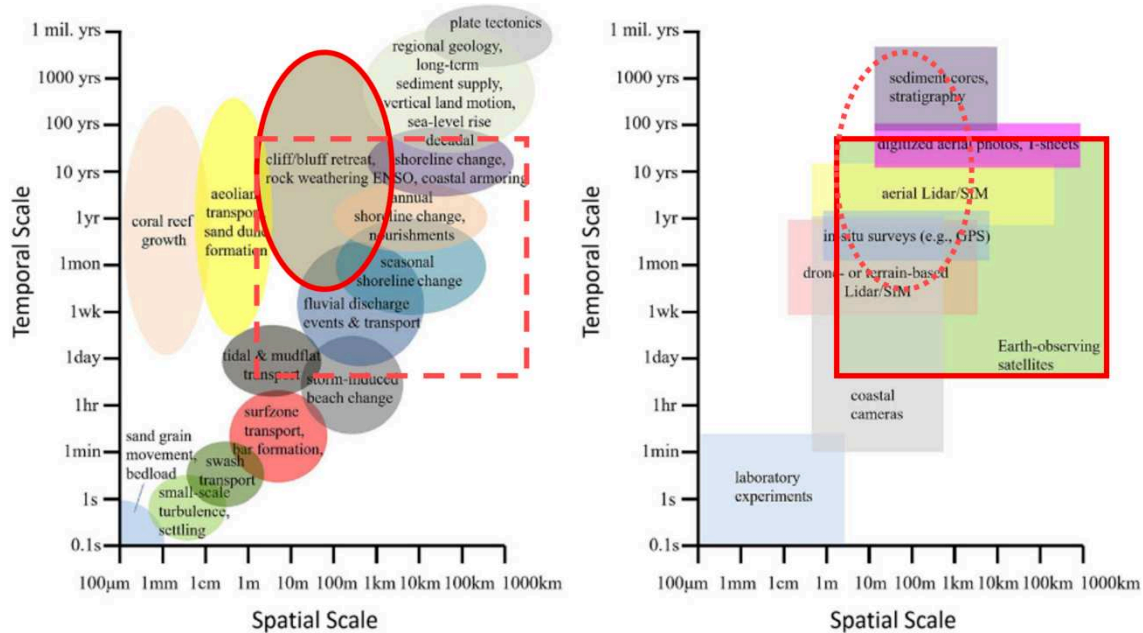


Figure 2.2: A visual representation of the temporal and spatial scales of coastal change processes and monitoring techniques (Vitousek et al., 2023), highlighting cliff erosion and satellite imagery.

2.3. Satellite observation missions

To understand how satellite imagery can be used to monitor coastal developments, it should be evaluated how observational satellites operate. These satellites can be divided into two categories: radar and optical. Radar satellites use electromagnetic waves to monitor the Earth's surface, allowing them to operate in darkness or through cloud cover, as they do not rely on sunlight (European Space Agency, 2024). Optical satellites, on the other hand, use cameras and sensors to register light reflections and create images of the Earth (Space Shift Inc., 2024; U.S. Geological Survey, 2025a). This is comparable to standard cameras, but with a broader range of spectral bands.

Satellite imagery distinguishes itself from other monitoring techniques since the data is freely accessible through open-access sources, such as the Landsat missions (USGS and NASA) and Sentinel missions (ESA). These images can be obtained through various platforms, one of which is Google Earth Engine (GEE), where they are stored collectively (Gorelick et al., 2017). The images have spectral resolutions of 30 and 10 meters respectively (European Space Agency, 2025; U.S. Geological Survey, 2025a), with revisit periods of 16 and 5 days. The revisit period refers to the number of days between successive observations of the same location at the equator, after completing a full global mapping cycle. The 5-day revisit time for Sentinel-2 is achieved through two identical satellites in near-identical, out-of-phase orbits. At higher latitudes, the revisit time decreases due to the swath width, which is the width of the Earth's surface captured in a single satellite pass — essentially how much the satellite can “see” at once.

Both the Landsat satellites as the satellites from the Sentinel-2 mission carry multiple instruments that detect the reflection of different spectral bands, ranging from coastal aerosol, blue, green, and red, as well as visible and near-infrared (VNIR/NIR) and shortwave infrared (SWIR) (European Space Agency, 2025). Additionally, Landsat satellites are equipped with thermal sensors (U.S. Geological Survey, 2025a). An overview of all the relevant variables of the satellites accessible in the GEE are listed in table 2.3.

Satellite	Active years	Resolution	Revisit time	Spectral bands	Swath width
Landsat 5	1984 - 2013	30 meters	16 days	11 bands: blue - SWIR (0.45-2.35 μm) + thermal (10.40-12.50 μm)	185 kilometers
Landsat 7	1999 - 2022	30 meters	16 days	8 bands: blue - SWIR (0.45-2.35 μm) + thermal (10.40-12.50 μm)	185 kilometers
Landsat 8	2013 - active	30 meters	16 days	11 bands: coastal aerosol - SWIR (0.43-2.29 μm) + thermal (10.60-12.51 μm)	185 kilometers
Landsat 9	2021 - active	30 meters	16 days	11 bands: coastal aerosol - SWIR (0.43-2.29 μm) + thermal (10.60-12.51 μm)	185 kilometers
Sentinel-2	2015 - active	10 meters	5 days	13 bands: coastal aerosol - SWIR (0.443-2.19 μm)	290 kilometers

Table 2.3: Overview of the satellites accessible through GEE, with their resolutions, revisit times, spectral bands and swath widths. Landsat information acquired through U.S. Geological Survey (2025a) and NASA (2025), Sentinel-2 through European Space Agency (2025).

As can be seen, the Sentinel-2 satellites provide a finer spatial and temporal resolution compared to the Landsat missions. Furthermore, it was found that Landsat 5 only provides usable imagery until 1995, while due to inaccurate geo-referencing few images are admissible, while Landsat 7 experienced a sensor failure from 2003 onward resulting in data gaps in each image (U.S. Geological Survey, 2025a). Due to these errors limiting the historic database, and the coarse resolution of the Landsat missions that are admissible, it was decided that this research only focuses on Sentinel-2 imagery.

2.4. Satellite-derived shoreline methods

Approximately 40 remote sensing algorithms have been developed to derive satellite-derived shorelines (SDS) (Vos et al., 2023). These algorithms can be categorized into different methodological approaches, such as land/water thresholding, maximum-gradient contouring, and soft classification techniques (Vitousek et al., 2023). They also vary in resolution: some operate at pixel level, while others use sub-pixel resolution, meaning they interpolate information from neighboring pixels to produce smoother contours. An overview of these different methods is given in Figure 2.3.

Some of the SDS-algorithms work using composite images techniques (Almeida et al., 2021; Luijendijk et al., 2018). This technique means using multiple satellite images to obtain a single composite image which has a reduced amount of noise, while also losing information on variability to some extent (Hagenaars et al., 2018). Since cliff coasts have limited seasonal variability - erosion rates can be higher in winter, but cliffs do not 'grow' back in summer - and tides do not influence the location of the cliff top, composite images could show promise to be implemented in a cliff line detection algorithm.

Previous research has shown that most SDS-algorithms using composite images compute an annual mean composite, meaning that all images from one year are merged into a single image by averaging the spectral values of each pixel (Almeida et al., 2021; Luijendijk et al., 2018). In another SDS-algorithm, tests were conducted using different time windows for composites (ranging from 90 days to two years), showing that longer time windows improve the detection of long-term trends, while seasonal variations become less visible (Hagenaars et al., 2018). That study used the 15th percentile value instead of the mean, assuming this approximates the median after cloud filtering.

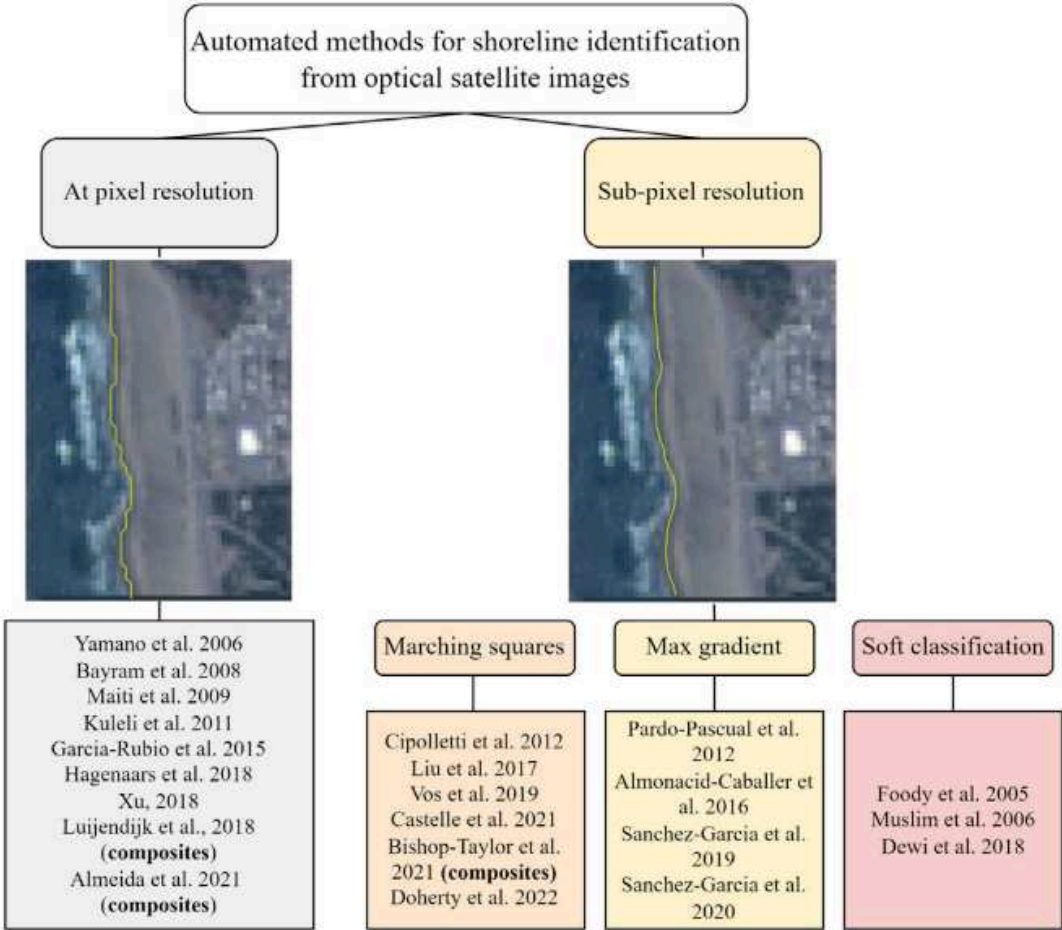


Figure 2.3: A summary of different methods to automatically map shoreline using optical satellite imagery, including an example of shoreline detection at pixel resolution (left) and sub-pixel resolution (right) (Vitousek et al., 2023).

Despite the differences in methodological approaches, as can be seen in Figure 2.3, these algorithms work on the same principles. By defining a region of interest, obtaining satellite imagery of that area resulting in spectral reflectance values for every pixel in every image (Almeida et al., 2021; Luijendijk et al., 2018; Palomar-Vázquez et al., 2023; Vos et al., 2019). From these spectral reflectance values, spectral indices can be calculated, resulting in a shoreline.

In a study conducted by Vos et al. (2023), five established SDS-algorithms were benchmark tested to assess their accuracy. These included CoastSat (Vos et al., 2019), SHOREX (Sánchez-García et al., 2020), ShorelineMonitor (Luijendijk et al., 2018), CASSIE (Almeida et al., 2021), and HighTide-SDS (Mao et al., 2021). The algorithms differ in aspects such as satellite sources, temporal frequency, and whether they are open-source. They were compared based on time-series analyses of the Mean Sea Level (MSL) contour and long-term shoreline trends.

Since one of the goals of this research is to find out how accurate a cliff line detection algorithm is, it is valuable to look at how accurate existing shoreline detection algorithms are, as there are no universally accepted thresholds. In previous studies validating SDS-algorithms, bias and standard deviation are commonly used as performance metrics (Almeida et al., 2021; Palomar-Vázquez et al., 2023; Vos et al., 2019), while there is also a benchmarking study performed on multiple SDS-algorithms by Vos et al. (2023), using these same performance metrics. In Table 2.4, the performance of the above mentioned algorithms is summarized.

SDS-algorithm	Bias (absolute)	Standard deviation (σ)
CoastSat (Vos et al., 2019)	- ($\mu = 1.4$ meters)	7.0 meters
CASSIE (Almeida et al., 2021)	8.3 meters	-
SAET (Palomar-Vázquez et al., 2023)	0.0-1.0 meters	2.6-3.8 meters
Benchmark: CoastSat (Vos et al., 2023)	2.3-12.0 meters	8.2-20.1 meters
Benchmark: SHOREX (Vos et al., 2023)	4.8-27.3 meters	6.9-25.2 meters
Benchmark: CASSIE (Vos et al., 2023)	1.7-6.7 meters	8.6-48.3 meters
Benchmark: ShorelineMonitor (Vos et al., 2023)	0.5-32.9 meters	7.9-20.1 meters
Benchmark: HighTide-SDS (Vos et al., 2023)	5.5-53.7 meters	7.8-22.9 meters

Table 2.4: An overview of an evaluation of SDS-algorithms scoring on statistical performance indicators for shoreline position.

Apart from seeing how existing shoreline detection algorithms score on determining absolute shoreline positions, it is interesting to look into how accurate they describe shoreline trends. From the three individual studies (Almeida et al., 2021; Palomar-Vázquez et al., 2023; Vos et al., 2019) it was not possible to obtain data on shoreline trends, but from the benchmarking tests, data could be obtained (Vos et al., 2023). Graphs were provided that show the shoreline trends to in-situ data, which could be overlaid with a grid to obtain numerical values. An example of this process for the one of the five sites used in the test is shown in Figure 2.4. Based on the erosion trends for all sites and SDS-algorithms investigated by the benchmarking test, the bias and standard deviation were calculated and presented in Table 2.5.

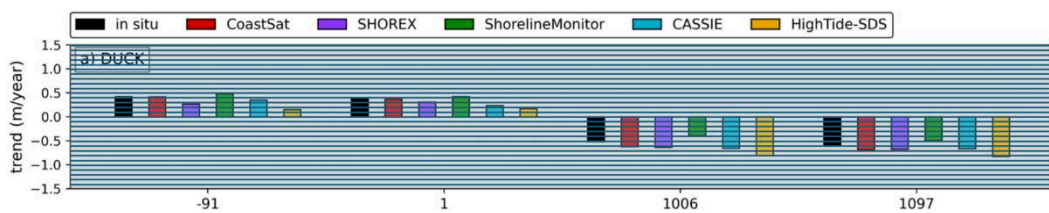


Figure 2.4: A visual representation on how the erosion trend rates were determined for the five benchmarking tests, based on Vos et al. (2023).

SDS-algorithm	Bias	Standard deviation (σ)
CoastSat	0.2 m/year	0.7 m/year
SHOREX	0.3 m/year	0.6 m/year
CASSIE	0.2 m/year	0.7 m/year
ShorelineMonitor	-0.1 m/year	0.6 m/year
HighTide-SDS	0.3 m/year	0.9 m/year

Table 2.5: An overview of an evaluation of SDS-algorithms scoring on statistical performance indicators for shoreline trends, based on Vos et al. (2023).

Since this research aims to develop a cliff line detection algorithm from existing SDS-algorithms, one of the SDS-algorithms should be chosen to do so. Of the five algorithms from the benchmarking tests, which are the most-used algorithms worldwide, ShorelineMonitor and HighTide-SDS rely solely on Landsat imagery, which limits both temporal and spatial resolution. Since SHOREX is not open-source, the two remaining algorithms are CoastSat and CASSIE. CoastSat is more versatile due to its additional supervised classification step (Vos et al., 2019), which CASSIE lacks (Almeida et al., 2021). Furthermore, while they perform similarly regarding shoreline trends, it was found that CoastSat has a lower standard deviation when determining absolute shoreline positions (Vos et al., 2023). Therefore it was decided to use CoastSat as basis to create a cliff line detection algorithm.

2.5. Spectral indices

For obtaining a shoreline, the Normalized Difference Water Index (NDWI) (Gao, 1996) or Modified Normalized Difference Water Index (MNDWI) (Xu, 2006) are used in SDS-algorithms (Almeida et al., 2021; Luijendijk et al., 2018; Palomar-Vázquez et al., 2023; Vos et al., 2019). These indices were optimized to determine the difference between water and different land features. However, when a cliff line needs to be detected, an index is needed to distinguish different land features from each other, since cliffs sometimes have sandy foreshores (Pye & Blott, 2015), while there also should be a land - water separation for if the cliff is directly adjacent to the sea.

In the search for a suitable index to distinguish land features from each other and water, the focus was on distinguishing built environments, vegetation and bare soils from sand and water, as these land types often exhibit similar reflectance values in the five spectral bands used by CoastSat (blue, green, red, NIR, and SWIR) (Vos et al., 2019). Table 2.6 presents a list of spectral indices that describe differences between water and land types using these five bands.

Index	Formula	Purpose	Reference
Modified normalized difference water index	$MNDWI = \frac{SWIR-G}{SWIR+G}$	Highlights water bodies	(Xu, 2006)
Normalized difference built index	$NDBI = \frac{SWIR-NIR}{SWIR+NIR}$	Highlight built-up area	(Zha et al., 2003)
Normalized difference vegetation index	$NDVI = \frac{NIR-R}{NIR+R}$	Highlight vegetation	(Bhandari et al., 2012)
Normalized difference water index	$NDWI = \frac{NIR-G}{NIR+G}$	Highlight water bodies	(Gao, 1996)
Bare soil index 1	$BSI1 = \frac{(SWIR+R)-(NIR+B)}{(SWIR+R)+(NIR+B)}$	Highlight bare soil areas	(Chen et al., 2004)
Bareness index	$BI = R + SWIR - NIR$	Highlight urban area	(Lin et al., 2005)
Band ratio for built-up area	$BRBA = \frac{R}{SWIR}$	Highlight built-up area and bare soil	(Waqar et al., 2012)
New built-up index	$NBI = \frac{SWIR \cdot R}{NIR}$	Highlight built-up area	(Jieli et al., 2010)
SwiRed	$SwiRed = \frac{SWIR-R}{SWIR+R}$	Highlight built-up area	(Capolupo et al., 2020)
Dry bare-soil index	$DBSI = MNDWI - NDVI$	Highlight (dry) bare soil	(Rasul et al., 2018)
Improved normalized difference built-up index	$INDBI = NDBI - NDVI$	Highlight built-up area	(He & Xie, 2010)

Table 2.6: Overview of spectral indices using a combination of blue, green, red, near infrared and short-wave infrared bands, used to detect differences between different land types and water, based on Javed et al. (2021) and Nguyen et al. (2021).

2.6. Principles and workflow of CoastSat

CoastSat is an advanced Python-based algorithm that enables users to generate time series of sandy shoreline positions spanning over 30 years, using publicly available satellite imagery, with a horizontal accuracy of approximately 10 meters (Vos et al., 2019). The algorithm downloads open-access satellite imagery, after which a classifier is trained using a small number of images by manually labeling pixels as water, white-water, sand, or other. This classifier, which can be trained for specific locations, is then used to classify each pixel in all downloaded images. The classification is based on the reflectance values of the blue, green, and red spectral bands, as well as the Normalized Difference Water Index (NDWI) and the Normalized Difference Vegetation Index (NDVI). After pixel classification, the Modified Normalized Difference Water Index (MNDWI) is calculated for each pixel individually. Each pixel now has both a class and an MNDWI value between -1 and 1, with water typically associated with negative values and land with positive values.

A Probability Density Function (PDF) is constructed to compare the distribution of MNDWI values for each class. From this PDF, a threshold is computed using Otsu's thresholding method (Otsu, 1979), which maximizes the inter-class variance between sand and water, as can be seen in Figure 2.6. This threshold represents the boundary between land and water, and the shoreline is defined as the location where the MNDWI equals this threshold, within a spatial buffer around a manually drawn reference shoreline. Using the marching squares algorithm, a sub-pixel resolution is achieved (Cipolletti et al., 2012). The full process is illustrated in Figure 2.5.

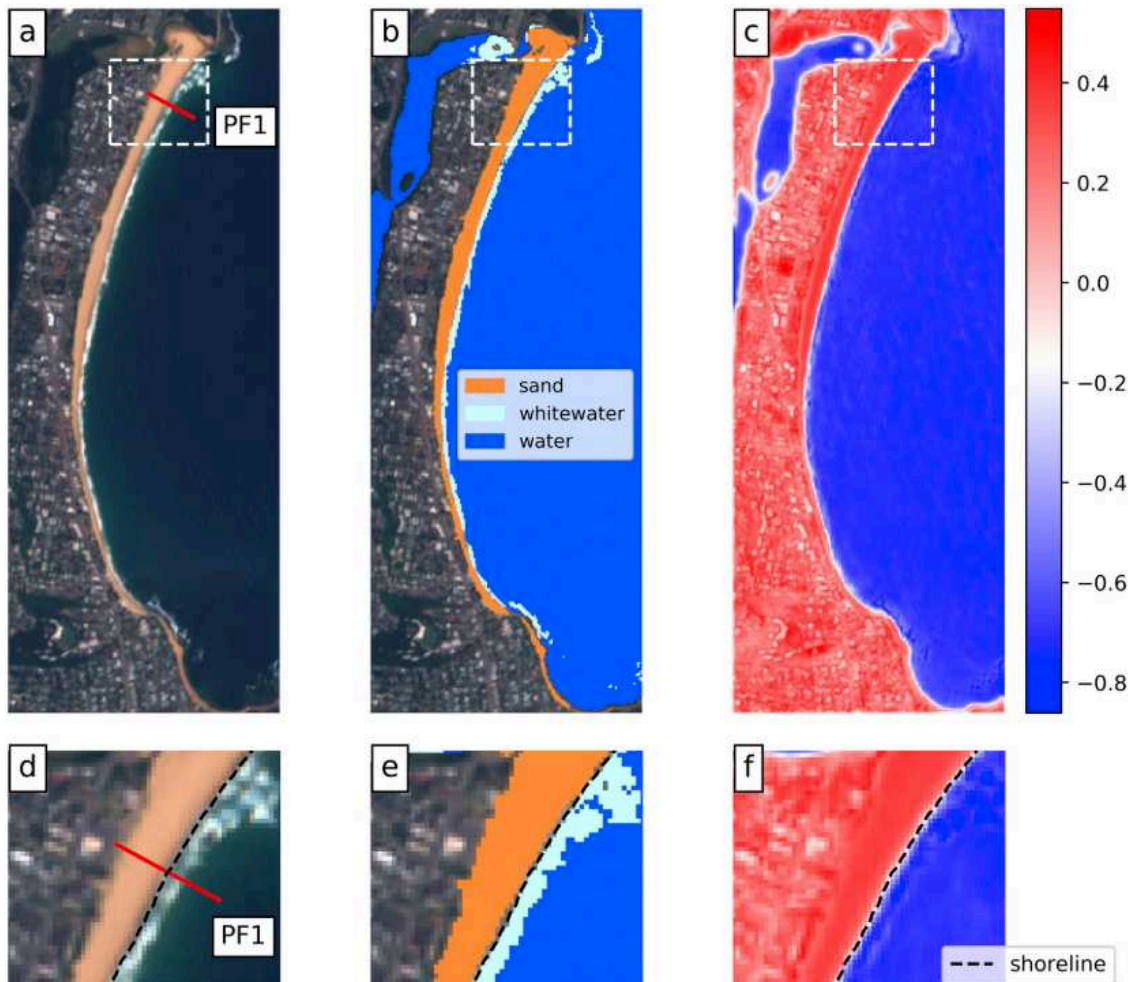


Figure 2.5: Example of the process of CoastSat and its outputs (Vos et al., 2019): a) RGB image of the region of interest (in this case Narrabeen-Collaroy) and transect PF1. b) Output of image classification (sand, water, white-water). c) scale of MNDWI, blue being negative and red positive, with a shoreline on the Otsu-threshold. d), e) and f) a zoomed in views of the region of interest of respectively a), b) and c).

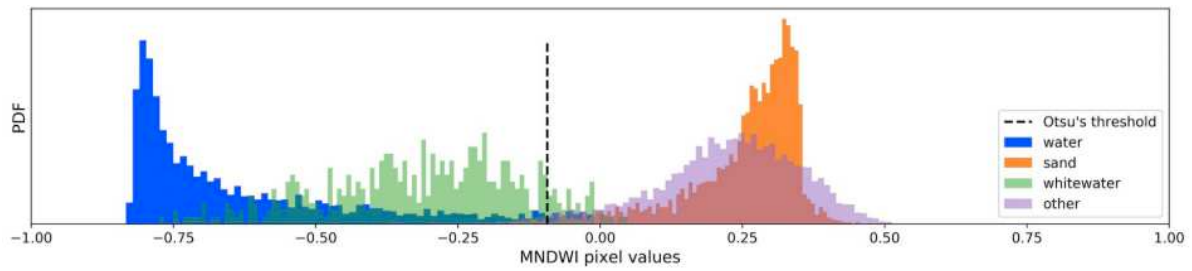


Figure 2.6: An example of a probability density function of MNDWI values for different classes, showing the threshold between water and sand (Vos et al., 2019).

If the process described above is repeated for multiple satellite images, a time series can be created. By manually drawing or loading in transects along the shoreline, the individual shoreline positions per image can be collected per transect. After tidal correction and filtering methods to remove outliers, a time-series of shoreline position is created, an example of which can be seen in figure 2.7.

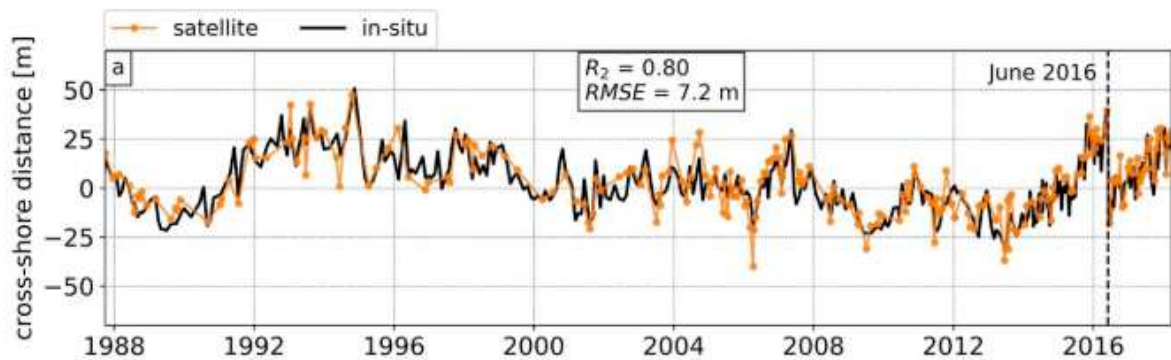


Figure 2.7: An example of a tidally corrected timeseries of shoreline position extracted by CoastSat (orange line) along transect PF1 from Figure 2.5 compared to in-situ data (black line) (Vos et al., 2019).

In recent years, CoastSat has been adapted to detect vegetation in coastal areas (Lanza et al., 2023), by using NDVI instead of MNDWI to delineate the shoreline. In this case, a threshold is determined to distinguish between vegetation and water, potentially enabling shoreline detection in non-sandy environments — making it particularly promising for application to cliff coasts. An example of this output is shown in Figure 2.8.

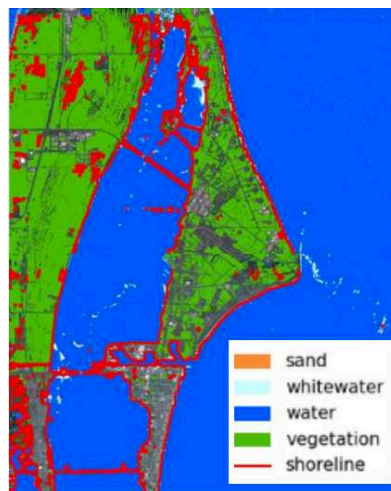


Figure 2.8: Example of CoastSat with the added vegetation index, using NDVI to detect the shoreline (Lanza et al., 2023).

Methodology

This chapter presents the methodology of this research. It begins with a description of proposed modifications made to the existing CoastSat algorithm to enable the detection of cliff erosion. This is followed by the introduction of a case study to which the new algorithm will be applied, after which the method used to compare the algorithm's results with existing data is explained.

3.1. Development of the satellite-derived cliff line algorithm

The objective is to modify CoastSat in such a way that, instead of detecting the coastline, it identifies the clifftop line. A key difference between these two is that for sandy coasts, the coastline is typically defined as the transition from sand to water and is therefore equal to the waterline. For cliff coasts, however, the cliff line may need to be determined relative to the water, or relative to a sandy or rubble foreshore.

From the literature, it was found that CoastSat relies on the reflectance values of the blue, green, red, NIR and SWIR bands to classify pixels into the classes water, white-water, sand or other, after which the MNDWI is used to distinguish sand and water at sub-pixel resolution to determine the waterline. Since sub-pixel resolution is a finer resolution than pixel resolution, it is preferred to maintain that quality. To distinguish multiple land features such as vegetation and built environments from sand and water, however, a different index than the MNDWI is required.

In the search for a suitable alternative index, the focus is on distinguishing vegetation, built environments and bare soils from sand, as these land types often exhibit similar reflectance values in the spectral bands used by the algorithm (blue, green, red, NIR, and SWIR). In Table 2.6 presents a list of spectral indices that describe differences between water and land types using these five bands. These indices will be tested in the algorithm to evaluate their performance, after which a final selection will be made in Chapter 4.

To ensure that a reliable threshold can be determined between “other” land features and sand or water, a new classifier must be trained. In the current CoastSat algorithm, four default classifiers are available, each representing a different type of sandy beach. However, when adapting the algorithm to detect cliff lines, it is also necessary to consider the type of cliff during classifier training. The existing classifiers are not sufficiently specific for this purpose.

Another opportunity for the new satellite derived cliff line (SDC) algorithm is that cliffs are less dynamic and not affected by, for example, tides — unlike beaches - as can be seen in Figure 2.2. Because of this, the use of composite images could be valuable to reduce the spread in measurements. In Chapter 2.4, the use of composite images is explained, stating that the longer time window is chosen, the less seasonal variability is obtained while improving the detection of long-term trends. Since this research focus is on whether a cliff line detection algorithm can accurately determine erosion trends, it is decided to use a time window of one year.

To evaluate whether composite images are a valuable addition to the SDC-algorithm, the algorithm is tested using both individual images and composite images. The composite approach that will be used is a composite with a time window of a year, with a moving window every month. This means that composite A contains images from, for example, January till December, composite B contains images from February till January, and so on. The moving window is chosen to use a moving window to be able to see the change more gradually, and to have more data points, making it easier to filter for errors.

The composite technique that will be used is the mean, as CoastSat already includes a cloud filtering method. This ensures that cloudy images are excluded, making the mean preferable over the median since more information is than captured. Using the mean allows all images to contribute to the composite, resulting in a smoother and more continuous trend. A visual representation of the composite imaging technique is shown in Figure 3.1.

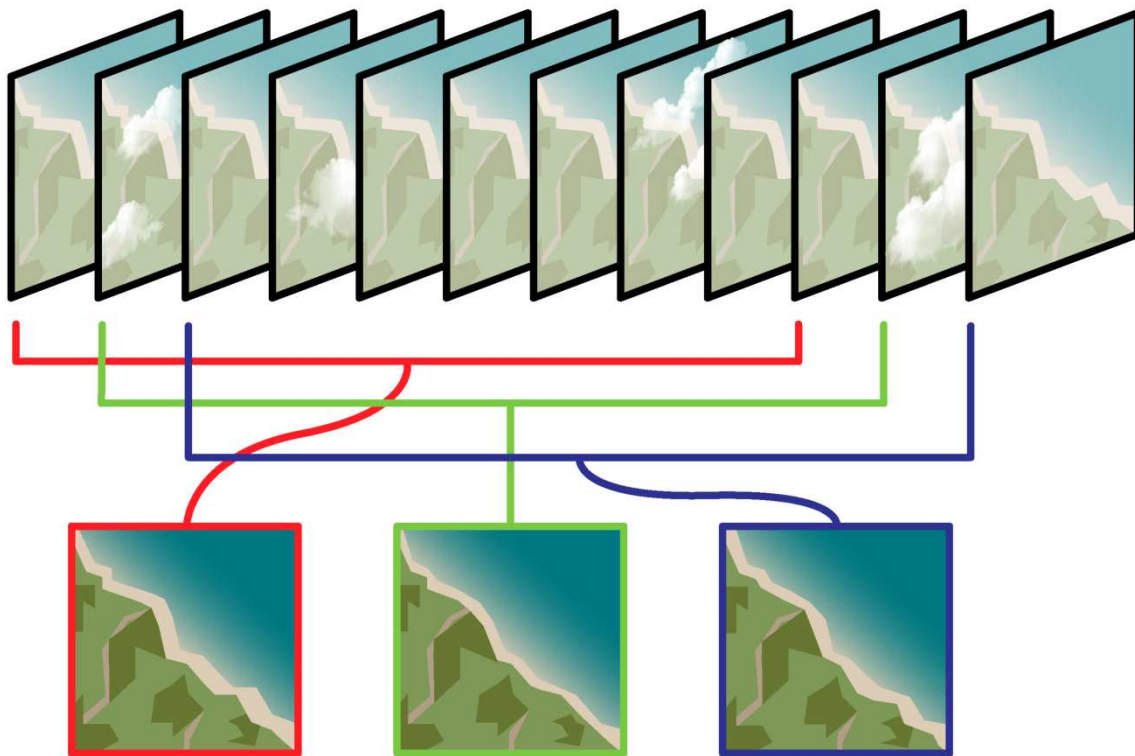


Figure 3.1: A visual representation of the mean composite imaging technique with a sliding window.

3.2. Case study: the Holderness Coast

To validate the new algorithm, a study must be conducted to assess the accuracy of the satellite-derived cliff line in comparison to in-situ measurements. For this purpose, a site is required that exhibits varying erosion rates, different cliff types, and a beach at the foreshore. The Holderness coast was identified as a suitable case study, as it meets all three criteria.

The Holderness coast is located in the East Riding of Yorkshire (East Yorkshire), a ceremonial county on the east coast of England. East Yorkshire has a population of approximately 600,000 people and covers an area of around 2,500 km². The coastline stretches from Bridlington to Easington and is approximately 60 kilometers long. It primarily consists of clay cliffs, with heights ranging from 5 to 35 meters (Pye & Blott, 2015). The exact location is shown in Figure 3.2.

The Holderness coast is particularly suitable for validating the new algorithm due to the findings of earlier research by Pye and Blott (2015). This study showed that total erosion in the area between 1852 and 2013 ranged from 0 to nearly 500 meters, corresponding to average erosion rates of 0 to 4 meters per year. This variation, combined with the diversity of land cover on top of the cliffs (including vegetation, farmland, and urban areas), makes it an ideal site for comparison.

Since 1999, biannual measurements have been conducted to monitor cliff line retreat, using a cross-shore spacing of 500 meters (East Riding Coastal Monitoring Programme, 2024). Initially, these measurements were performed using GPS, but since 2009, aerial LiDAR scans have been used. The current monitoring program is funded until March 2027, with expectations for continuation beyond that date.

The East Riding of Yorkshire Council (ERYC) have shown interest in this research, since they are investigating if they want to expand their measurement campaign by adding more interim results between two LiDAR scans. For that reason, they have agreed to share the latest data from their monitoring campaign, so the algorithm can be validated.

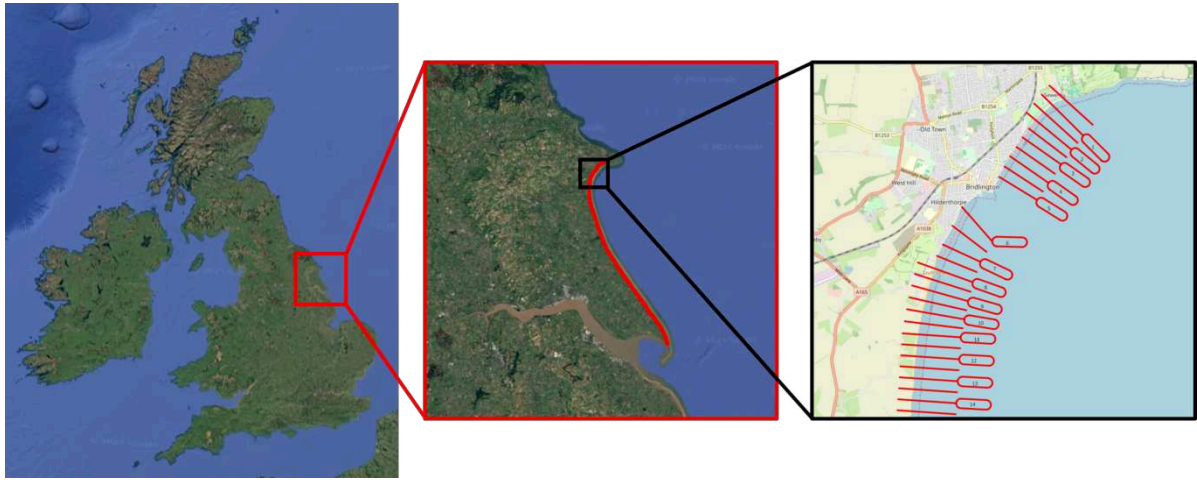


Figure 3.2: Location of the Holderness coast, retrieved from Google Maps (2025), with on the right a representation of how the transects, used to measure erosion rates, are defined.

3.3. Data processing and collection

The East Riding of Yorkshire Council (ERYC) have shared data of 101 transects along the coast, for which per half year the retreat of the cliff top is given in meters. The output that is generated by CoastSat is a timeseries of shoreline positions for any given transect along the coastline. Considering a revisit period of 5 days - the revisit period for Sentinel-2 satellites, this means that over 70 shoreline positions can be obtained per year.

To compare the data to the output of the model, processing steps have to be taken. From the data, a total amount of erosion can be obtained by adding the erosion amounts per half year for the time period of interest. For the algorithm, the total erosion amounts can be obtained by taking the distance between shoreline positions over that same time period. To compare the erosion trend, for both the data and the algorithms output a linear regression trend will be calculated, resulting in a comparable erosion rate in meters per year.

The comparison will be conducted over the period from September 2015 to September 2024. This time period was chosen because Sentinel-2 became operational in June 2015, and first measurement taken after that was in September. Furthermore, September 2024 is the most recent available data. For the composite imaging method the comparison will be from March 2016 to September 2024, considering the yearly composites span a whole year, and thus half a year of range is lost on both ends, and the first measurement was conducted in March 2016. To reach September 2024, the last composite contains data from February 2025. An overview of this is presented in Figure 3.3

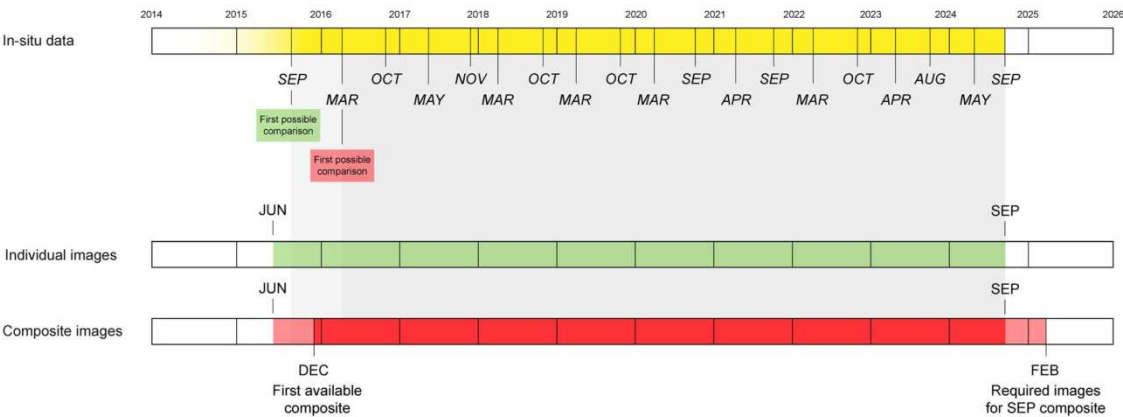


Figure 3.3: A visualization of the time periods for which the single image method and composite method will be compared to the in-situ data.

3.4. Validation criteria

To assess the accuracy of the new algorithm, its results will be compared to the available data from the case study introduced above. From the biannual erosion measurements available for the Holderness coast, both the total amount of erosion and a linear erosion trend can be derived. Therefore, the algorithm should output the total erosion per transect as well as the corresponding linear trend.

To evaluate the accuracy of the algorithm, its performance will be assessed using statistical indicators. In previous studies validating SDS-algorithms, bias and standard deviation are commonly used as performance metrics, as discussed in Chapter 2.4. For this reason, the new SDC-algorithm will also be validated using these two indicators. The bias indicates whether the algorithm systematically over- or underestimates erosion, while the standard deviation reflects the variability of the error.

As there are no universally accepted thresholds for these indicators in coastal monitoring, acceptable limits were derived from the performance of existing SDS-algorithms, as can be seen in Table 2.4 and Table 2.5. From these results can be concluded that acceptable limits for a SDS-algorithm are, for total erosion amounts, a bias below 3 meters and a standard deviation below 7 meters. For erosion trends, the acceptable limit for bias was determined to be 0.3 meters per year, with a standard deviation of 0.7 meters per year.

4

Results

In this chapter, the results of the research are presented. First, the modifications made to the CoastSat algorithm are discussed, including the rationale behind each change. Second, the output of the new algorithm, called CliffSat is compared to the data from the Holderness coast, followed by an evaluation of its performance.

4.1. Outcomes of the satellite-derived cliff line algorithm

To adapt CoastSat for the extraction of the cliff line instead of the shoreline, several modifications are proposed in Chapter 3.1. In this section, the proposed changes are evaluated and the best method is selected on how the modifications are implemented. After this, an overview of the new workflow is given.

4.1.1. Spectral index evaluation

The first required change is the use of a different index to derive a sub-pixel resolution cliff line that separates sand and water from vegetation, built environments, and bare soils. All indices listed in Table 2.6 are implemented in the algorithm, and their performance is evaluated. For this evaluation, two cloud-free images with dry-exposed sand from different seasons are used, to be able to compare all land features without noise. Seasonal variation is included to assess how well the indices perform under changing vegetation conditions.

In Figures 4.1 and Figure 4.2, an example of the results of the comparison is presented. Figure 4.1 shows the probability density function of the index values for the four classes for three different indices (BI, BSI and SwiRed), showing the differences between the indices and how effectively the index is able to separate the classes. In Figure 4.2, all indices that are investigated are shown compared to the satellite image used. All the figures from the indices that are analyzed can be found in Appendix A.

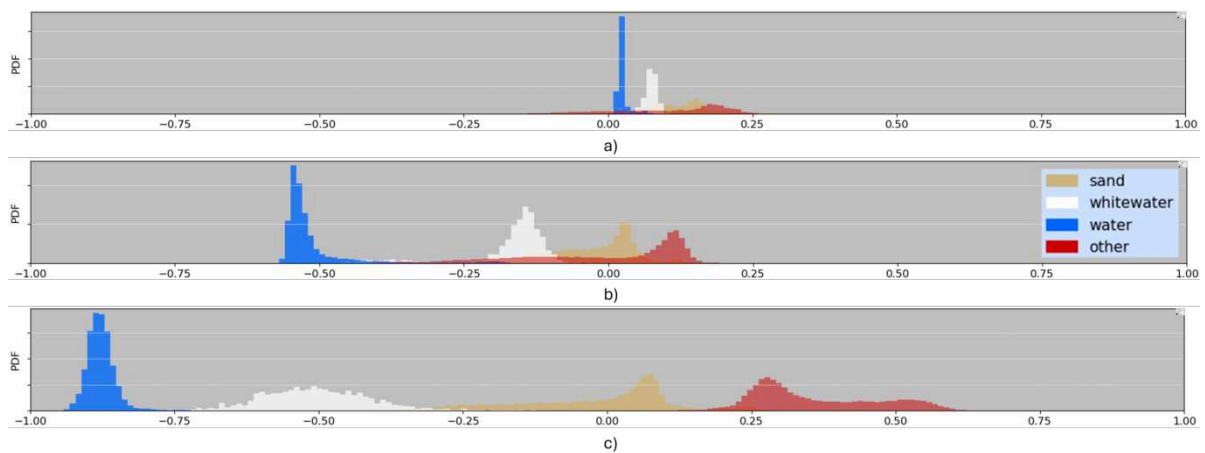


Figure 4.1: An example of the probability density function of three indices separating the four classes, used to determine a threshold resulting in a cliff line for the indices BI (a), BSI (b) and SwiRed (c), showing the differences between how well the indices are able to separate the classes.

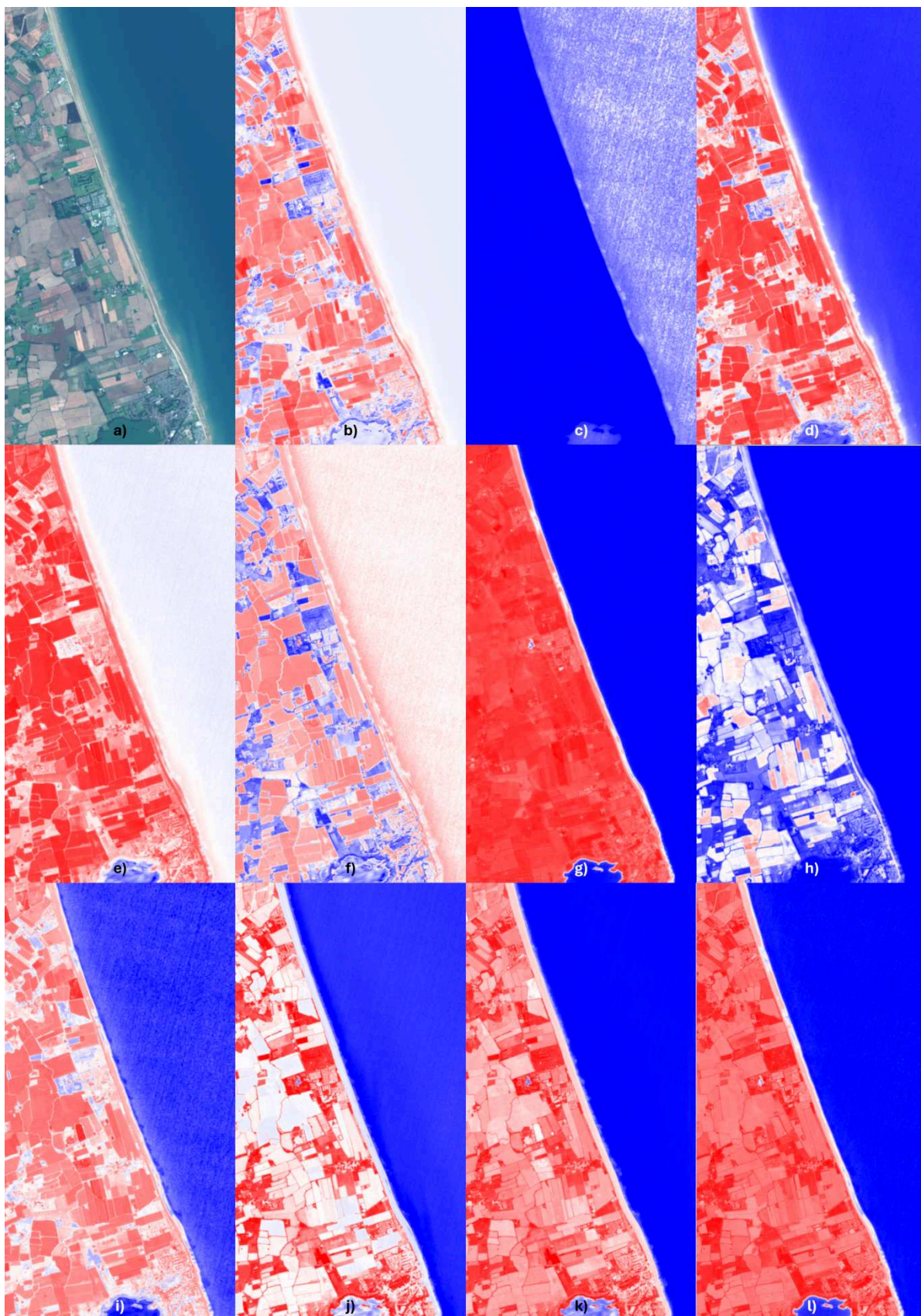


Figure 4.2: Index comparison of a satellite image taken on 17-09-2024 spanning transects 20-45, with a indices BI (b), BRBA (c), BSI (d), DBSI (e), INDBI (f), MNDWI (g), NBI (h), NDBI (i), NDVI (j), NDWI (k), SwiRed (l).

From the full analysis can be concluded that the NDVI, SwiRed and INDBI demonstrate the best performance in distinguishing land features. NDVI clearly separates vegetation from sand and water, while the SwiRed index more effectively distinguishes built environments from sand and water. INDBI performs well in separating built environments from sand, but shows limited contrast between land and water. Seasonal differences are clearly visible: in Figure 4.3, farmlands appear green, while in Figure 4.4, they are more sand-colored, making it harder for the indices to differentiate between land types. It can be seen that the NDVI and SwiRed are less sensitive for these seasonal changes than the INDBI.

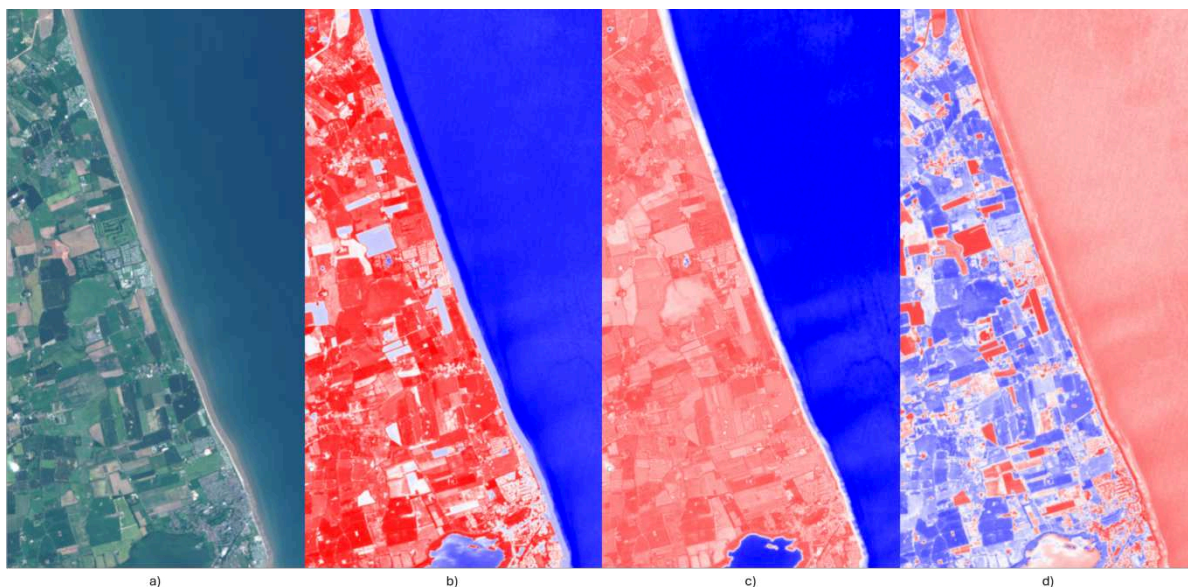


Figure 4.3: Index comparison of a satellite image. a) satellite image taken on 24-06-2024 by Sentinel-2. b) NDVI. c) SwiRed. d) INDBI.

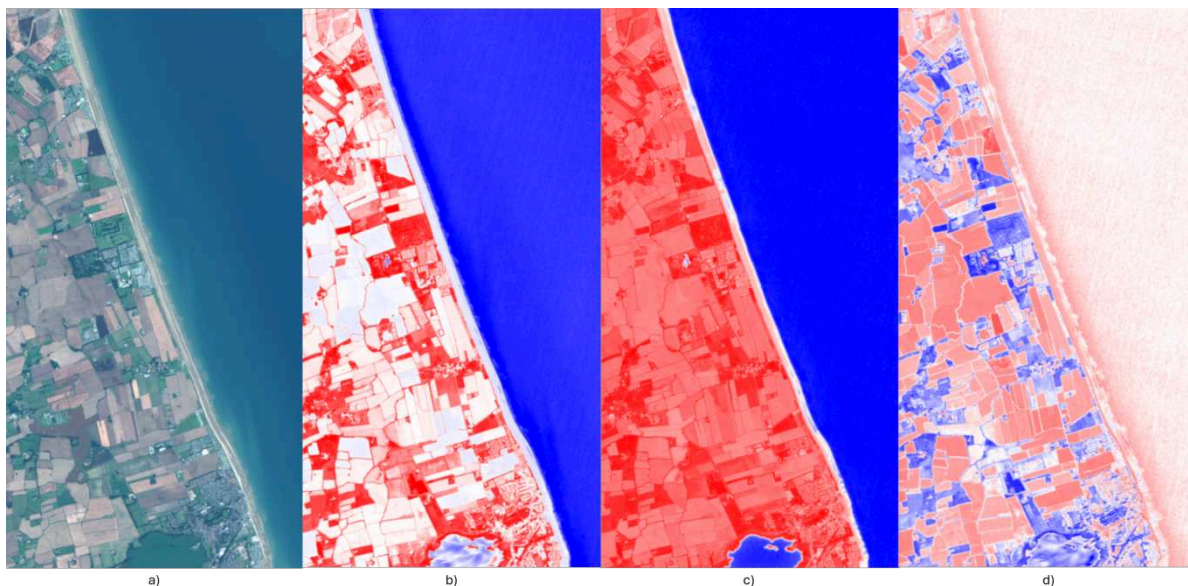


Figure 4.4: Index comparison of a satellite image. a) satellite image taken on 17-09-2024 by Sentinel-2. b) NDVI c) SwiRed d) INDBI

When looking into the probability density function (PDF) of the three indices in Figure 4.5, it can be seen that in the PDF of the INDBI there is significant overlap between the 'other'-class and the other three classes, compared to NDVI and the SwiRed index. This means that the NDVI and SwiRed are better in separating the four classes for this area, resulting in a more distinct threshold to determine the cliff line.

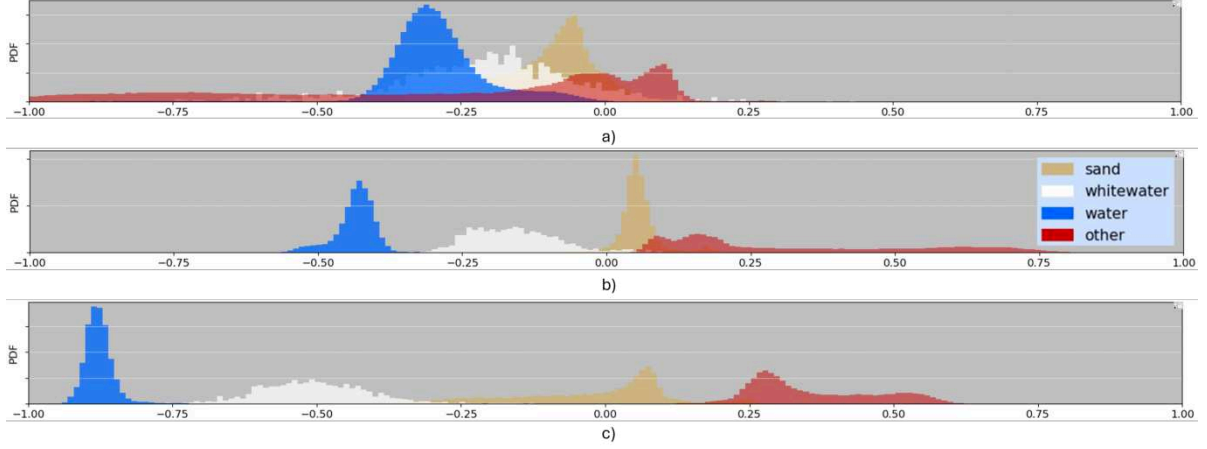


Figure 4.5: The probability density function comparison of INDBI (a), NDVI (b) and SwiRed (c), showing that NDVI and SwiRed are better in distinguishing the four land classes.

For optimal results, it is decided to combine the NDVI and SwiRed indices. This approach enhances the overall distinction between vegetation and sand due to the influence of NDVI, while the SwiRed index improves the separation between sand and built environments. Both indices assign negative values to (white-)water, values around zero to sand, and positive values to various land types, as summarized in Table 4.1.

Index	Water	White-water	Sand	Vegetation	Built environment
NDVI	< -0.4	< -0.3	$-0.1 - 0.2$	$0.3 - 0.9$	$0 - 0.3$
SwiRed	< -0.5	< -0.3	$-0.3 - 0.2$	$0.1 - 0.6$	$0.1 - 0.3$

Table 4.1: Range of values for different classes for the NDVI and SwiRed index. Based on Laksono et al. (2020), Capolupo et al. (2020) and simulations of the model.

To combine the two indices, the most straightforward options are addition, subtraction, multiplication, or division, as other indices are also commonly combined in these ways (Javed et al., 2021). Since both indices assign similar values to the different land features, subtraction and division are not suitable — these operations would result in values clustering around zero for all land types. Therefore, addition and multiplication remain as viable options.

Before the indices can be multiplied, all values must be shifted to positive by adding 1. This ensures that negative values remain negative in relative terms, and positive values remain positive. As a result, addition yields a combined index with a value range from -2 to 2 , while multiplication produces an expected range from -1 to 1 (after subtracting 1 again post-calculation to return to the original scale). The results of both addition and multiplication methods are presented in Table 4.2.

Index	Water	White-water	Sand	Vegetation	Built environment
Addition	< -0.9	< -0.6	$-0.4 - 0.4$	> 0.4	$0.1 - 0.6$
Multiplication	< -0.7	< -0.5	$-0.4 - 0.4$	> 0.4	$0.1 - 0.6$

Table 4.2: Theoretical range of values of the combined indices using addition and multiplication.

From Table 4.2 can be concluded that both methods of combining the indices yield similar results, meaning that no clear preference can be determined based on these values alone. To further assess which method is more suitable, both were implemented over a 10-kilometer stretch of coastline, and the resulting probability density functions (PDF) from the cliff line detection were analyzed.

It was found that the PDF generated using the multiplied indices showed a slightly broader spread within the “sand” and “other” classes, as illustrated in Figure 4.6. Additionally, the (white-)water region was more distinctly defined. These characteristics make the multiplication method slightly more suitable for combining the indices in this context.

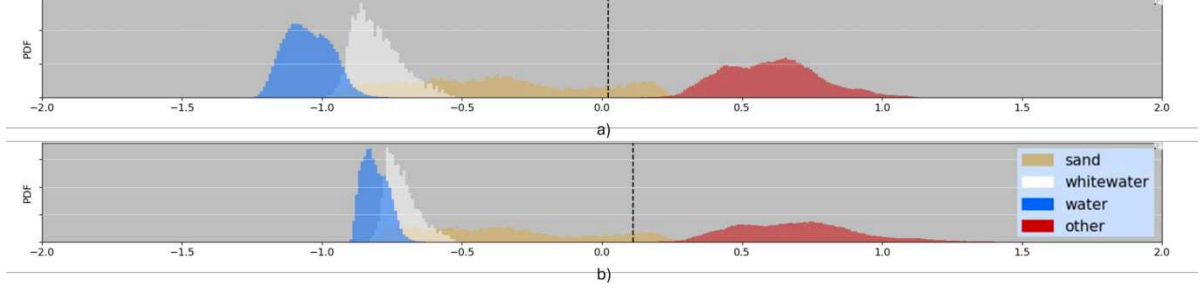


Figure 4.6: Comparison of the probability density function of the two index combination methods. a) addition; b) multiplication.

The index used in the remainder of this research is therefore calculated using the following formula:

$$Index = (NDVI + 1) * (SwiRed + 1) - 1 = \left(\frac{NIR - R}{NIR + R} + 1\right) * \left(\frac{SWIR - R}{SWIR + R} + 1\right) - 1$$

To proof this index is an improvement compared to the index used by CoastSat, MNDWI, the resulting cliff line by the indices of CoastSat (MNDWI) and CliffSat are compared in Figure 4.7, with the probability density functions of the indices presented in Figure 4.8. As visible, the newly found index causes a better distinction between land and sand, creating a clear cliff line compared to the cliff line created when using the MNDWI. In Appendix B, a more elaborate evaluation can be found on how the indices of CoastSat and CliffSat compare and the resulting effect on both shoreline and cliff line detection.

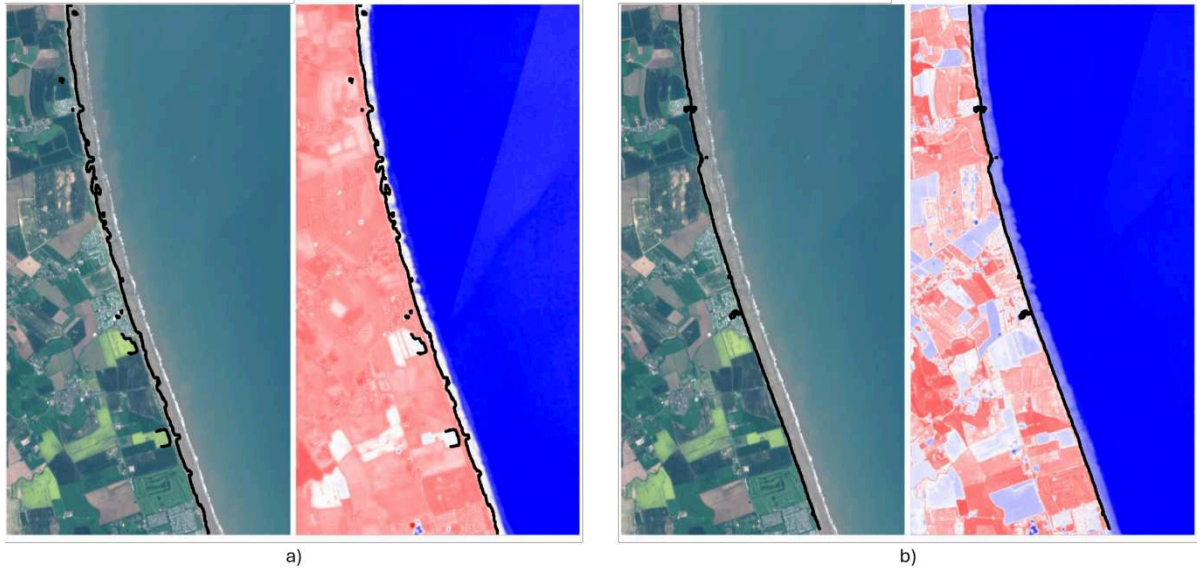


Figure 4.7: A comparison of the MNDWI (a) and newly found index (b) for cliff line extraction for transects 17-28 on 15-05-2018, showing that a more clear cliff line is found when using the new index.

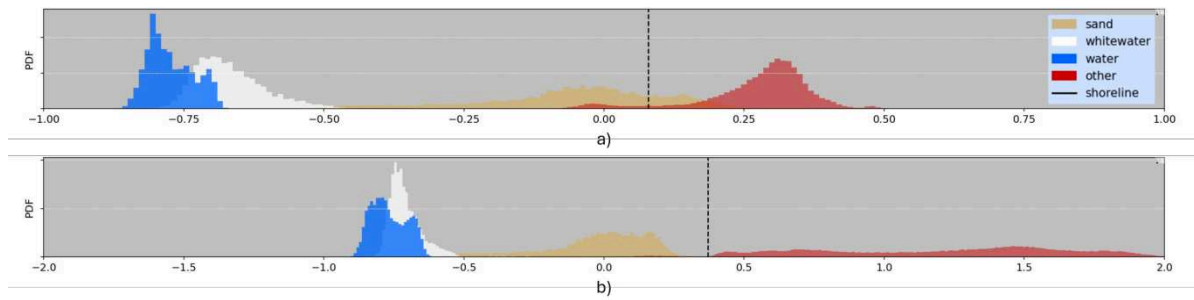


Figure 4.8: A comparison of the probability density functions of the MNDWI (a) and newly found index (b) for transects 17-28 on 15-05-2018, showing that the new index better separates the four classes.

4.1.2. Creating composite images

Now that the index has been identified, the use of composite images can be evaluated. As proposed in Chapter 3.4, the performance of individual satellite images is compared to composite images generated using a moving window per month with a time window of one year. It is decided to use a moving window to be able to see the change more gradually, and to have more data points, making it easier to filter for errors. These tests were carried out over a 10-kilometer stretch of coastline, covering transects 21-40 of the coastline.

The composite technique considered most effective beforehand is the mean composite, in which the average reflectance values of each spectral band per pixel are calculated and used. This method has an advantage over the median composite, as it incorporates all available images. This is beneficial because certain images capture high water levels or storm surges, resulting in water temporarily covering the beach. This effect is also created by the angle of incidence of the satellite. If the satellite takes the image from a certain angle from the cliff, due to the height and steepness of the cliff (a part of) the beach is not visible on the image, as shown in Figure 4.9. However, considering the mean altitude of 786 kilometers and the swath width of 290 for Sentinel-2 (European Space Agency, 2025), a maximum of just 5 meters of horizontal information disappears for a cliff with a height of 30 meters, and so this effect is small compared to the spatial resolution of the satellite.

The effect of water covering the beach causes the sand to be better distinguishable from other land features, considering the water has different reflection coefficients for both the red and infrared bands compared to sand and other land features. Since the amount of images where sand is covered by water is only a fraction of all the images, this would rarely influence the result when using a median composite, while when using the mean, these events contribute to the overall pixel value. Since water has a significantly lower index value, its presence lowers the average index of sandy areas, thereby enhancing the distinction between sand and land.

One issue observed when calculating the mean per pixel is the presence of noise caused by residual clouds that bypassed the cloud filter, resulting in white blurs on certain pixels. To mitigate this, all pixel values outside the range of one standard deviation were excluded when calculating the mean. This effectively removes the darkest and brightest reflections, including remaining cloud artifacts. By applying this filter, the advantage of capturing subtle water effects — improving the separation between sand and land — is retained, while extreme outliers are removed. This makes the filtered mean composite a robust and reliable method for use in the algorithm.

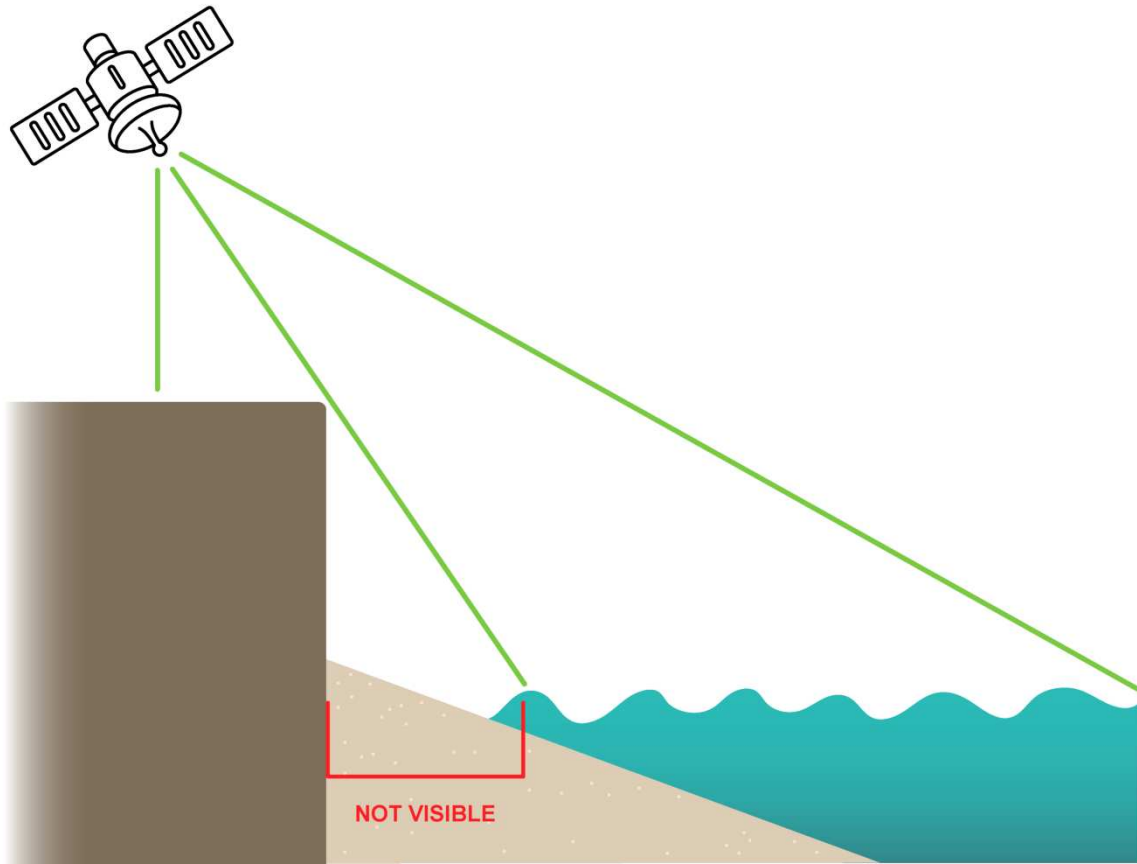


Figure 4.9: A visual presentation on the importance of the angle of incidence of the satellite, resulting in (parts of) the beach being invisible in some images due to the cliff height and steepness.

In Figure 4.10 the two methods - single images and yearly composite images - are shown for one of the 20 evaluated transects (transect 30). As can be seen, the variation between pictures is reduced by using composite images compared to single images, since the images range from 195 to 215 meters for the composite while it ranges from 180 to 220 meters for the single images.

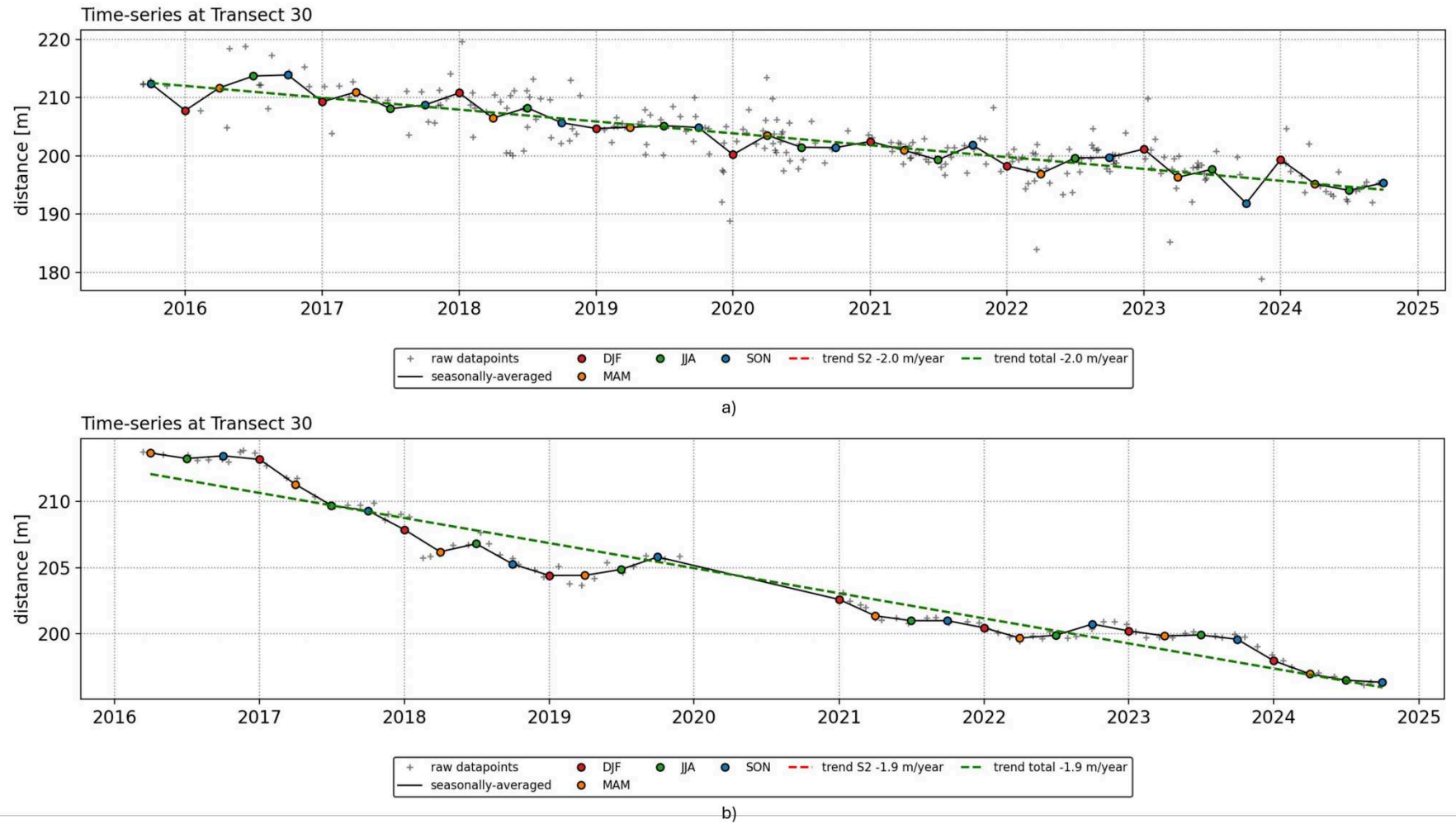


Figure 4.10: A comparison for the time-series of transect 30 for a) single images method and b) composite method, showing more variation around for the single images method.

When comparing the erosion trends derived from the two image techniques for transect 30, it can be seen that there is no significant difference (2.0 meters/year versus 1.9 meters/year), with the actual erosion trend, based on the provided data, was found to be 2.2 meters per year. For the other 19 transects that are evaluated, these same small differences are noticed, and thus it is decided that based on these 20 transects, presented in Figure 4.11, no decision can be made on which method is most accurate. For that reason, both methods will be validated for the entire coast.

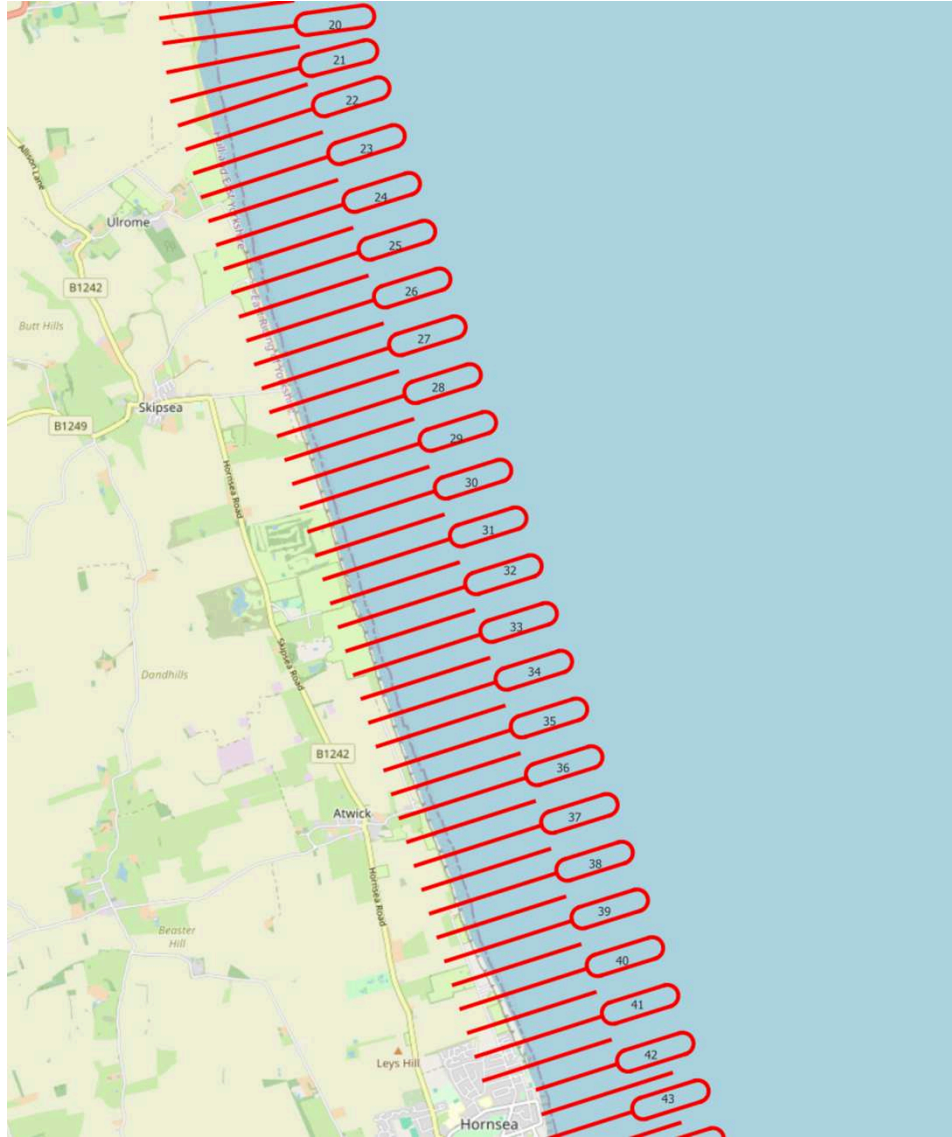


Figure 4.11: An overview of transects 20-40 on an open street map.

4.1.3. Overview of workflow

In Figure 4.12, an overview is given on the workflow of the new algorithm, CliffSat. It is based on the original CoastSat workflow, and one setting determines if the cliff line or shoreline will be determined. Important to note is that it is not yet decided if composite images are indeed a valuable addition, so the workflow is not definite yet. Furthermore, a mechanism is included that if there are no sand pixels present, the threshold is determined between land and water in stead of land and sand.

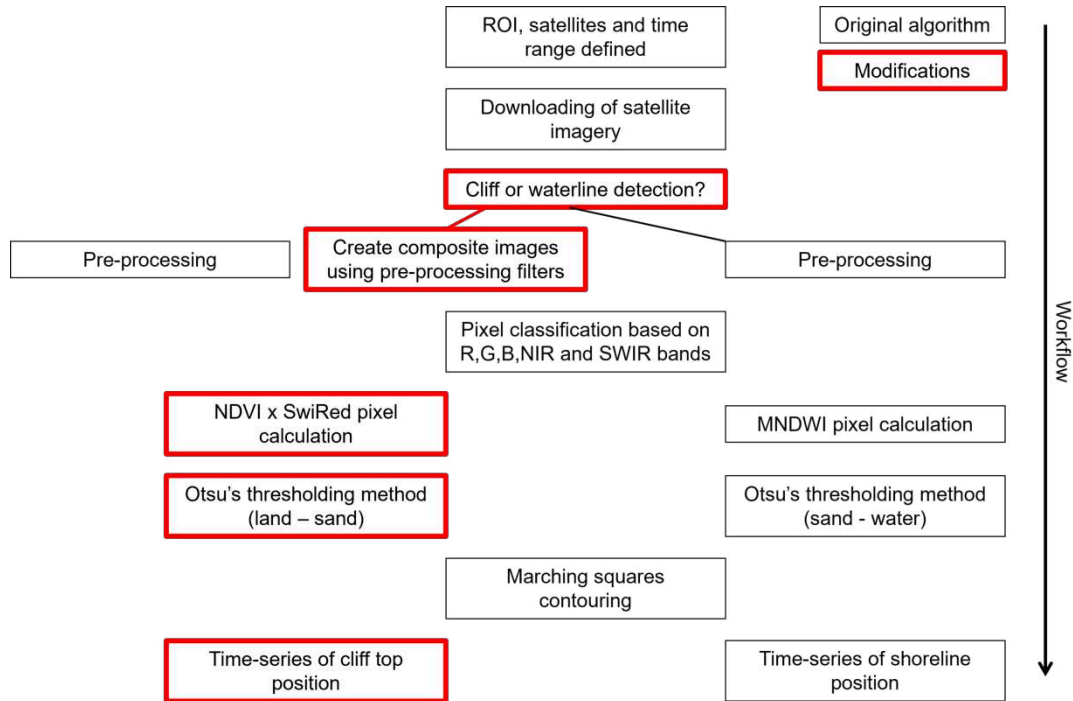


Figure 4.12: An overview of the workflow of the new algorithm, CliffSat, with the black boxes being the original workflow of CoastSat and the red boxes indicating the modifications that were made.

In Figure 4.13, an example is given on how the composite image with classification and new index calculation looks like, all contributing to the cliff line derivation.

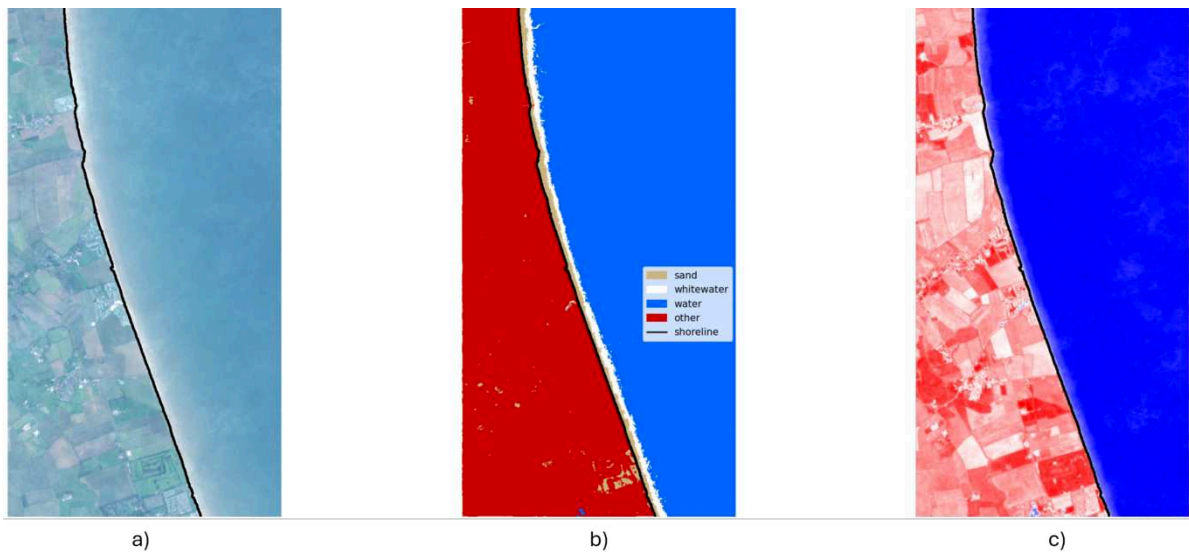


Figure 4.13: An example of the output generated by CliffSat, with the RGB composite image of transect 16-28 (a), pixel classification (b) and index calculation (c), resulting in a cliff line.

4.2. Validation of the algorithm

To validate the algorithm, the results are compared to the data of the Holderness coast. The available dataset consists of 121 cross-shore transects along the coastline, spaced at 500-meter intervals. Of these 121 transects, 20 are not actively monitored, because coastal defenses have been applied, resulting in data of 101 transects. These transects are loaded into the algorithm to ensure that the analysis is performed at the exact same locations as the field measurements.

4.2.1. General comparison of algorithms output to in-situ data

The comparison of the two methods (single image and composite) to the data is conducted for two outputs: the annual erosion trend, and the total amount of erosion recorded. As explained in Chapter 3.3, the single imaging method is compared to in-situ data from September 2015 until September 2024, while the composite method is compared from March 2016 until September 2024. It is found, however, that at the start of the Sentinel-2 mission, few images were admissible due to the fact that just one of the two planned satellites was in the air, resulting in a higher revisiting time, and images did not fulfill requirements regarding the georeferencing, which is used to align the images, meaning the images were filtered out in the process. For these reasons, the starting dates for the comparison are moved from September 2015 to March 2016 (single images) and from March 2016 to May 2017 (composite images), since no measurement was taken in the fall of 2016 due to bad weather.

To be able to compare the trend of the output compared to the trend of the data, the trend for the data is calculated first. This is done using linear regression, an example of which is given in Figure 4.14.

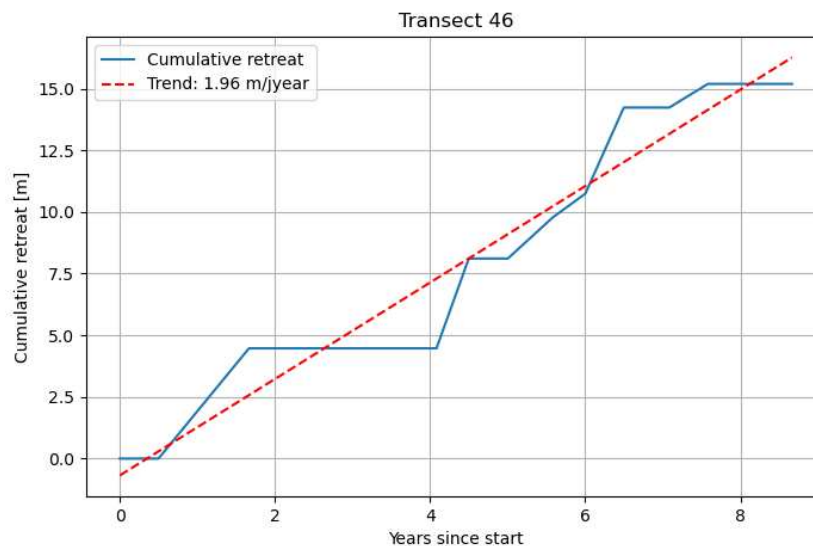


Figure 4.14: An example of how the linear erosion trend compares to the individual data points of a transect, in this case transect 46.

The results of the comparison are presented in Table 4.3 and Table 4.4, showing the bias and standard deviation of the algorithm's output for single images and composites, relative to the provided data. In Figure 4.15 and Figure 4.16, the bias and standard deviation are compared to the SDS-algorithms investigated in Chapter 2.4. All the settings in the algorithm, like the maximum allowed cloud cover in the imagery, the minimum length required for a valid cliff line, or the maximum cross-shore distance allowed between cliff lines across time steps are being kept constant. The total erosion amounts are captured after averaging individual shoreline positions for the month before and after the in-situ measurement, reducing individual errors.

Images used	Bias	Standard deviation (σ)
Single images	0.13 meters/year	0.69 meters/year
Yearly composites	0.14 meters/year	0.69 meters/year

Table 4.3: An overview of the statistical performance indicators for the yearly trend of the model compared to in-situ data.

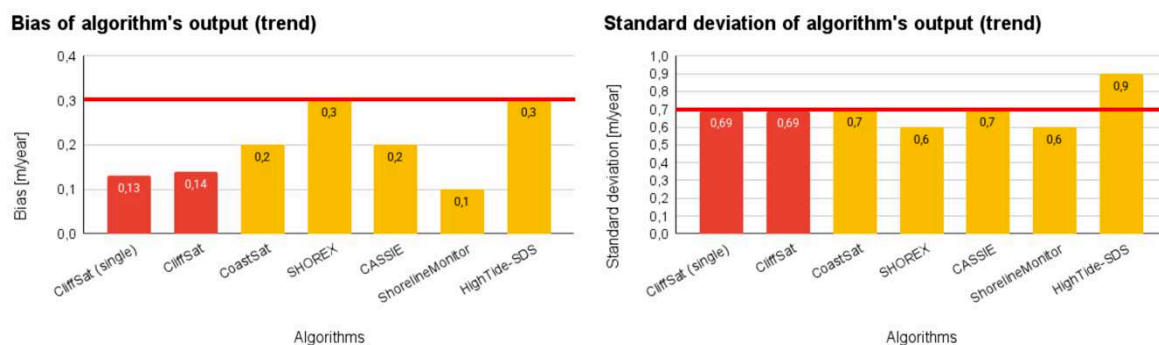


Figure 4.15: A visual presentation of the performance of the algorithm on capturing erosion trends compared to the performance of existing SDS-algorithms, with the red line showing the acceptable limit.

Images used	Bias	Standard deviation (σ)
Single images	-0.3 meters	5.5 meters
Yearly composites	-0.6 meters	4.7 meters

Table 4.4: An overview of the statistical performance indicators for total erosion of the model compared to in-situ data.

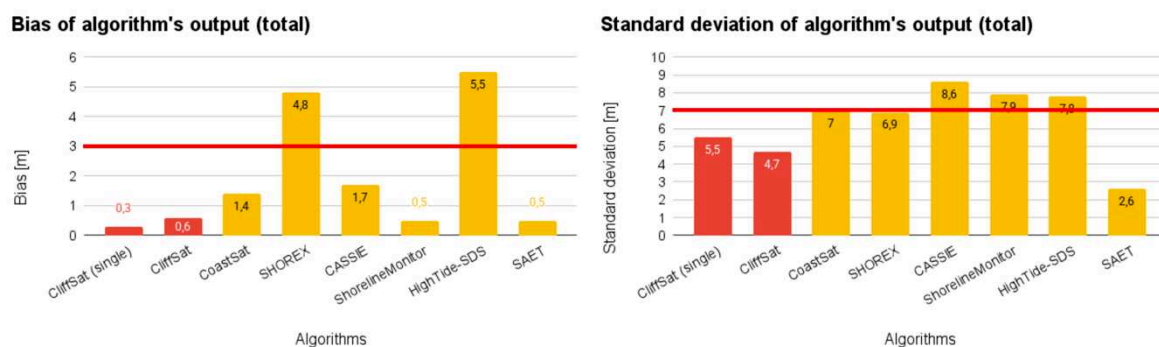


Figure 4.16: A visual presentation of the performance of the algorithm on capturing total erosion amounts compared to the performance of existing SDS-algorithms, with the red line showing the acceptable limit.

From these results, it can be concluded that for the yearly erosion trend, both methods reach the same accuracy, with a bias of 0.1 meters/year and a standard deviation of 0.7 meters/year. Comparing these results to the validation criteria found in Chapter 3.4, stating acceptable limits are a bias below 0.3 meters/year and a standard deviation of 0.7 meters/year or below, CliffSat operates (just) within these limits for both the single image method as the composite method.

For the total erosion amounts, the composite method shows to be more accurate. While the single image method has a slightly lower bias than the composite method, the standard deviation is almost a meter higher, meaning that the single image method has a higher variability than the composite method. Comparing these results to the validation criteria, it can be found that both methods have a much lower bias than the acceptable limit (3 meters), while also the standard deviation is well within the limit (7 meters).

To conclude the analysis of the accuracy of CliffSat for both the single image method and composite method, it can be found that the algorithm meets all validation criteria, while the composite method shows to be more precise when looking at total erosion amounts.

4.2.2. Comparison of output and data per erosion rate

Although the algorithm demonstrates reliable performance, it is important to consider its limitations. One aspect investigated is how the algorithm performs across different erosion magnitudes. Given that the spatial resolution of the satellite imagery used is 10 meters, and the analysis spans a period of 8 years, the data was categorized into two groups:

- Less than 1.2 meter of erosion per year (i.e., less than 10 meters total);
- More than 1.2 meters of erosion per year (over 10 meters total).

The results of this analysis are presented in Table 4.5 and Table 4.6.

Images used	< 1.2 meters/year		> 1.2 meters/year	
	Bias	Standard deviation (σ)	Bias	Standard deviation (σ)
Single images	-0.1 m/y	0.5 m/y	0.3 m/y	0.8 m/y
Yearly composites	-0.1 m/y	0.4 m/y	0.3 m/y	0.8 m/y

Table 4.5: An overview of the statistical performance indicators for erosion trend of the model compared to in-situ data, divided into different amounts of erosion.

Images used	< 10 meters		> 10 meters	
	Bias	Standard deviation (σ)	Bias	Standard deviation (σ)
Single images	-2.4 m	5.7 m	0.9 m	5.4 m
Yearly composites	-1.3 m	4.0 m	0.0 m	5.2 m

Table 4.6: An overview of the statistical performance indicators for total erosion of the model compared to in-situ data, divided into different amounts of erosion.

From these results, it can be concluded that for the erosion trend, the composite method is slightly more accurate for low erosion trends compared to the single image method, while they perform similar for erosion rates over 1.2 meter per year. For the total amount of erosion comparison, it shows that the composite method significantly improves the accuracy for erosion amounts below 10 meters, while the results for the erosion amounts above 10 meters do not show significant differences.

The conclusion can be drawn that the composite image method is more accurate than the single image method when it comes to low amounts of recorded erosion. Considering the observation that there is more variation in shoreline positions for the single image method compared to the composite method (Chapter 4.1.2), this difference can be explained by the fact that the variation that is present for the single images caused by the resolution has a higher influence when the total erosion is less than one pixel of an image (below 10 meters). If erosion rates are high, the difference between the cliff line positions within one composite are larger, causing a less distinct cliff line, and thus the advantage of lower variation disappears.

4.2.3. Investigation of errors

Upon reviewing the output, 13 transects are found where three or all of the four generated outputs (trend and total erosion for each of the two methods) exceed the standard deviation, as shown in Figure 4.17, when compared to the provided data, suggesting that the algorithm - regardless of the imaging method - tends to struggle in the same locations. These transects are further analyzed based on cliff height and the land features near the cliff edge.

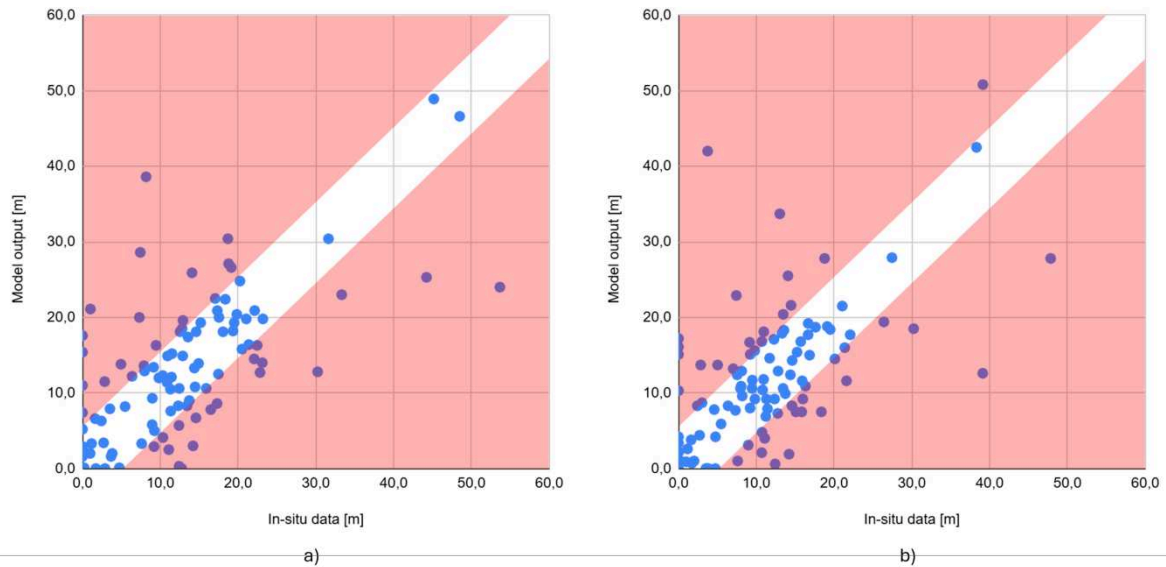


Figure 4.17: A visual representation of the values of total erosion amounts of the data compared to the output of the single image method (a) and the composite method (b).

When examining cliff height, two locations are identified where the cliff exceeds 20 meters over a stretch of five or more transects (East Riding Coastal Monitoring Programme, 2024; Pye & Blott, 2015). Of the 12 transects in these areas, 6 produced results outside the acceptable standard deviation range, indicating that cliff height does influence the model's accuracy. A possible explanation is that, assuming a similar slope across all cliffs, higher cliffs expose more of the cliff face in satellite imagery. This can result in different (generally lower) reflectance values, and thus a different index, introducing noise into the detection. Furthermore, the position of the satellite can cause the image to capture Unfortunately, no data on cliff slope is available to confirm this hypothesis.

Another aspect investigated is the influence of land features near the cliff edge. As discussed earlier in this chapter, the most challenging distinctions are between sand and built environments, or sand and bare soils such as dried farmland. Since the three largest cities along the coast are protected by coastal defense structures and are excluded from the current measurement program, the algorithm's performance in dense urban areas remains unclear. However, among the investigated transects, seven are located near campsites or parking areas at the cliff edge, showing these areas induce noise in the model. The remaining transects are located adjacent to farmland extending to the cliff edge. A closer look at these areas revealed seasonal changes in land cover — even in the yearly composites — where farmland sometimes appear as bare soil, introducing additional noise into the model. An example of this effect is shown in Figure 4.18, comparing the same area (transects 95-99) for composite images in 2017 and 2019.

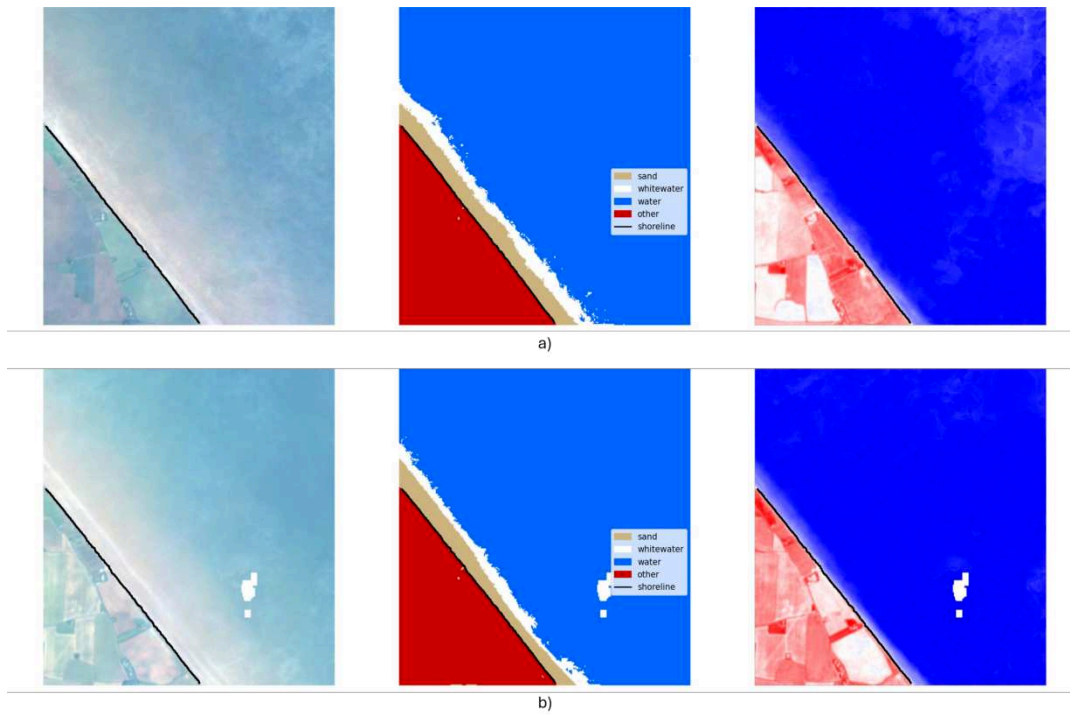


Figure 4.18: A comparison between the composites of December 2017 (a) and December 2019 (b) for transects 95-99. In figure a, it can be seen that the more inland fields have a lower index than the fields near the cliff, while in figure b this is the other way around. These changes in index near the clifftop edge cause noise in the model.

Apart from the cliff characteristics, it is found that errors also occur while finding the index threshold representing the cliff line. Errors in the classifying process cause some land pixels to be classified as sand, resulting in a shift in the threshold to a more positive index value, as can be seen in Figure 4.19. Since this error is dependent on how the pixels are classified, it causes variability in the timeseries, as can be seen in Figure 4.20. A more elaborate investigation into this error can be found in Appendix C.

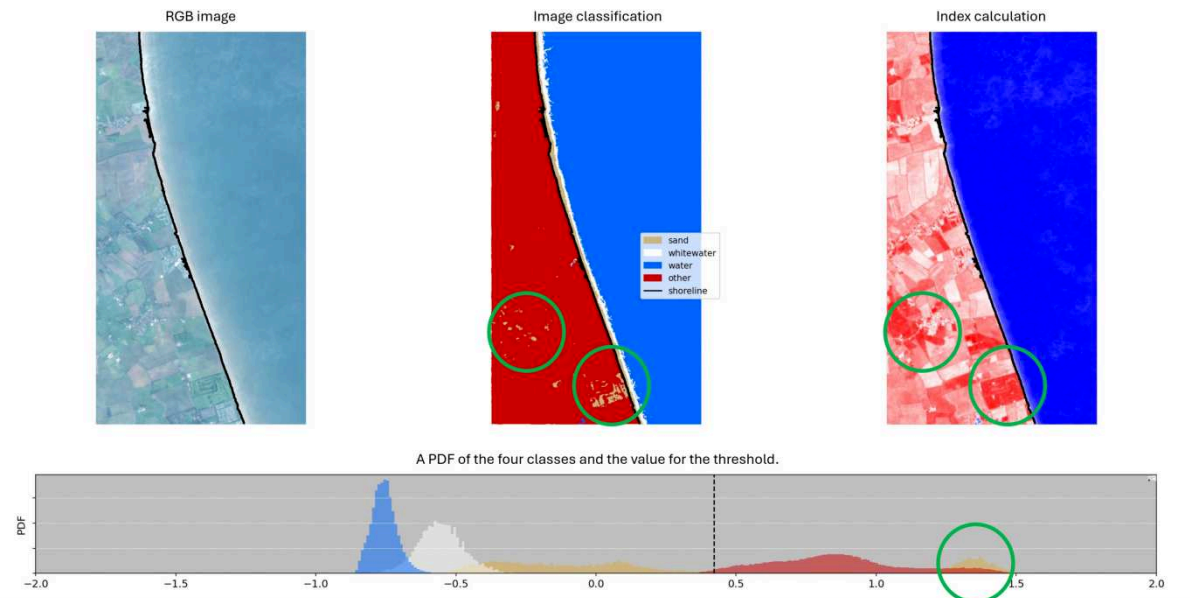


Figure 4.19: An example of the threshold determination for transect 17-28 using Otsu's thresholding method, showing that the threshold found (dashed black line) has a slight error towards 'other' (shown in red) compared to sand (shown in orange), caused by the peak in the sand class around the index value 1.4.

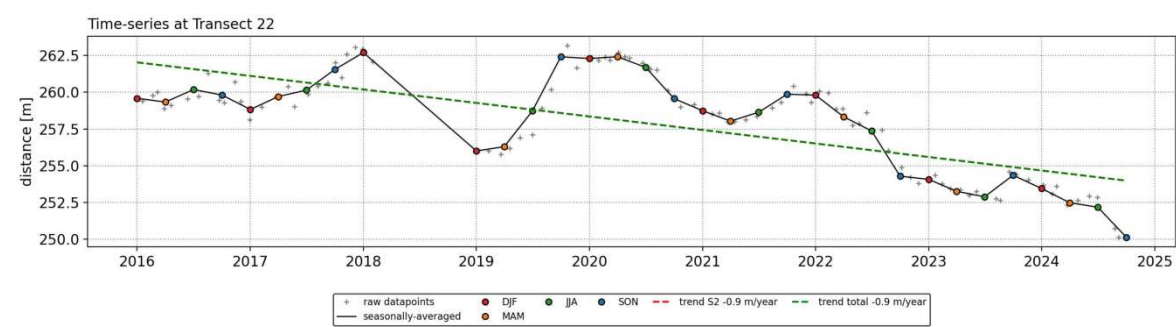


Figure 4.20: An example of variability for the timeseries of transect 22 caused by the error in threshold determination.

5

Discussion

In this chapter, the results of the research are discussed. First, the main findings are reiterated and interpreted, followed by an evaluation of the limitations of both the research and the algorithm and a reflection on the choices made in the research. Finally, the broader contributions and implications of the study are addressed.

5.1. Reiteration and interpretation of the results

In this research, an algorithm called CliffSat was developed to detect the cliff line based on satellite imagery. The algorithm was created based on CoastSat, an existing algorithm to derive shorelines from satellite imagery. First, the index used to determine the waterline (MNDWI) was changed, so a cliff line could be detected, separating the cliff from sand and water. It was found that the combination of NDVI and SwiRed worked best, considering the NDVI highlights vegetation and SwiRed built environment from other land features and water. Apart from the change of index, composite images were included in the algorithm. Using a window of a year that moves for every month, variations due to seasonality was excluded from the images, resulting in more stable results. With a bias of -0.6 meters and a standard deviation of 4.7 meters, the algorithm using yearly composite images was found to be the most accurate compared to using single images, while it also outperformed existing SDS-algorithms compared to their own validation tests.

While the previous chapter focuses on comparing the outputs of the two methods to existing data and comparing the statistical results with existing SDS-algorithms, it should be reflected on what the absolute results represent. Looking at the total erosion over the 8-year period, the absolute results of the algorithm are shown in Table 5.1 and Figure 5.1. The 5 and 10 meter ranges were based on the average standard deviation and the pixel size of the used satellite imagery. It can be concluded that both methods overestimate and underestimate with approximately equal amounts, which confirms the observed bias.

Images used	< -5 m error	> 5 m error	< -10 m error	> 10 m error
Single images	16	14	4	2
Yearly composite	15	12	3	2

Table 5.1: An overview of how big the error was for the two methods, differing in overestimation (< -5 / -10 meters) and underestimation (> 5 / 10 meters).

Measuring the amount of cliff erosion is highly relevant for determining how far from the cliff edge houses or recreational areas can be safely built, as discussed in Chapter 1. When comparing the results, it becomes clear that the least desirable outcome is a significant underestimation by the model compared to provided data, which would imply that the cliff is eroding faster than the model suggests. Looking at the results, just 2 out of 101 transects underestimate the real data more than 10 meters for both the imaging methods.

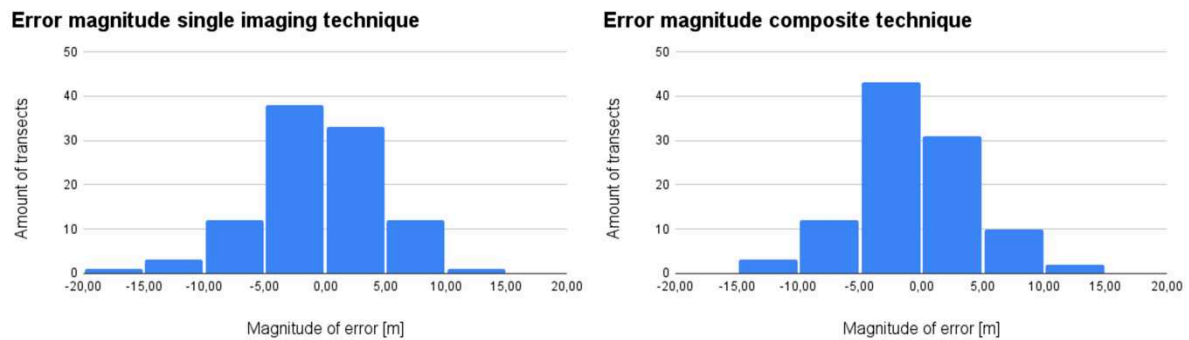


Figure 5.1: A visual representation of the error distribution of the total erosion amounts for the single image method and composite image method.

5.2. Reflection on methodological choices

The first choice that was made was to use CoastSat as the base of CliffSat. This choice was made due to it being the most suitable algorithm as was found in Chapter 2.4. Especially the extra step of classifying the pixels made it more easy to distinguish 'other' land features from sand. However, CoastSat also has its limitations, the most important one being that in CoastSat height is not incorporated, which is an vital aspect of a cliff coast. However, in none of the SDS-algorithms that were considered for this research height was a factor.

Another dominant factor in this research was the search for an index to be used. Although the currently used index has proven to be the reliable within the scope of this study, one could argue that other, yet untested indices might perform even better. To identify the most optimal index, it may be necessary to look beyond the five spectral bands currently utilized in this algorithm. Furthermore, the index that is now used is a combination of two indices, combined using multiplication. There might, however, be a more optimal way to combine these two indices to highlight the correct land features.

Since this study is performed on one case study, the index is specifically chosen for that site. Cliffs around the world, however, vary a lot in composition, and thus spectral reflections. This means that different cliff types need different spectral indices, and so the index used by CliffSat should be adjusted for every site. This is a disadvantage compared to SDS-algorithms, considering these use an index to separate water from land and therefore can be applied for different shorelines around the world.

In this research, composite images were created using a yearly window sliding for every month using the mean after outliers are filtered out. This method was chosen since it limits seasonal variation, while it adds the advantage that sand is sometimes covered by water and thus the distinction between other land features and sand is improved. This method showed consistent results, although there was still variability captured in the images, as shown in Figure 4.18. However, more extensive research can be done on the composite technique that is most effective.

To evaluate the use of composite images for CliffSat, the advantages and disadvantages should be listed. The main advantage is that it is more accurate, especially for sites with low erosion rates. However, due to the time window of a year, the episodic nature of cliff erosion is not captured using composites. Also, if cliffs have high erosion rates, a composite image with a time window of a year captures erosion within the image, making the cliff line less clear. This effect is also present if a cliff is high and the position of the satellite relative to the cliff varies, as shown in Figure 4.9, the position of the cliff between images varies slightly, while these image are combined into one composite. From this can be concluded that using composite images is not necessarily beneficial for every cliff.

5.3. Limitations and uncertainties

An important limitation of this research is that it spans a relatively short time range. Due to the limited period (8.5 and 7.5 years) and the spatial resolution of the satellite imagery used, the noise introduced by pixel size becomes significant, especially for transects with low erosion rates. When looking further back in time, from 2006 to 2024, only 9 of the 101 transects experience less than 10 meters erosion. This means that all other transects experience at least one pixel of erosion in that time period, improving the model's accuracy over time. Furthermore, because a short time range is used in the research, an absolute error of 5 meters in 7.5 years is of a bigger influence than if the error of 5 meters is recorded in 20 years, increasing the accuracy of the prediction of the erosion trend, making it more suitable for applications such as determining safe building distances from the cliff edge.

The short time span of this study also introduces uncertainty in the erosion trends calculated from the provided data. These trends were derived using linear regression, which can be misleading for transects where episodic erosion occurs. In such cases, the linear trend may deviate from the actual total erosion, as illustrated by two examples in Figure 5.2. Since only two measurements per year are available, peaks in erosion are not always captured by the linear regression trend. In contrast, the model — based on more frequent satellite observations — tends to reflect these variations more clearly, resulting in a linear trend that more closely approximates the total erosion divided by the number of years. Therefore, one could argue that comparing total erosion rather than the linear trend provides a more reliable basis for validating the model against the data.

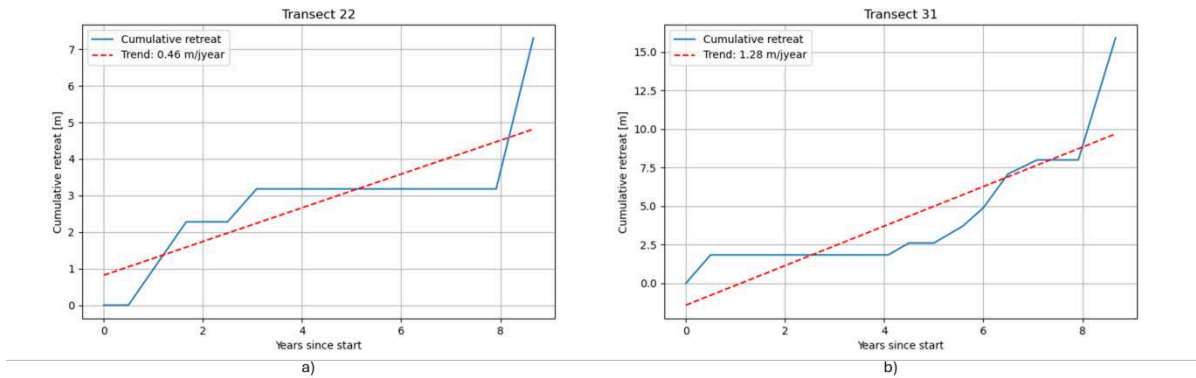


Figure 5.2: A visual representation of distribution of the erosion trend (a) and total erosion (b) for the single image method, divided per erosion rate.

Another limitation of this research is that it only covers one type of cliff coast. It is, however, also valuable to consider how this algorithm can be applied world wide. At present, it is optimized for cliffs with vegetation or built environments on top. However, there are many different types of cliffs all over the world. This study was performed for a clay cliff, while there are also numerous different types of rocky cliffs. Although rocky cliffs tend to be more resilient against erosion, it is still desirable to develop an algorithm capable of monitoring such cliffs. To achieve this, alternative indices may prove to be more robust. This implies that the type of cliff must be manually determined in order to select the appropriate index for monitoring.

Since cliffs are typically high with a steep slope, a limitation of the algorithm is that it does not take height into account. Currently, the model operates on two-dimensional imagery, while cliffs are characterized by a rapid increase in elevation. If cliff height is incorporated in the algorithm, cliffs that have similar spectral reflectance values compared to the beach, can still be distinguished. When incorporating cliff height, the absolute height of the cliff is not critical; rather, it is the elevation difference between the cliff and the adjacent beach or sea that matters.

5.4. Applicability of CliffSat

This research shows that there is potential for CliffSat to be able to determine cliff lines, however it is important to investigate how CliffSat can be applied. Looking at the temporal and spatial scale of the model and comparing it to coastal processes as presented in Figure 5.3, it can be seen that the spatial and temporal scale of the algorithm largely overlap with the spatial and temporal scale of (short-term) cliff retreat. However, storm induced changes and episodic events are not captured by CliffSat.

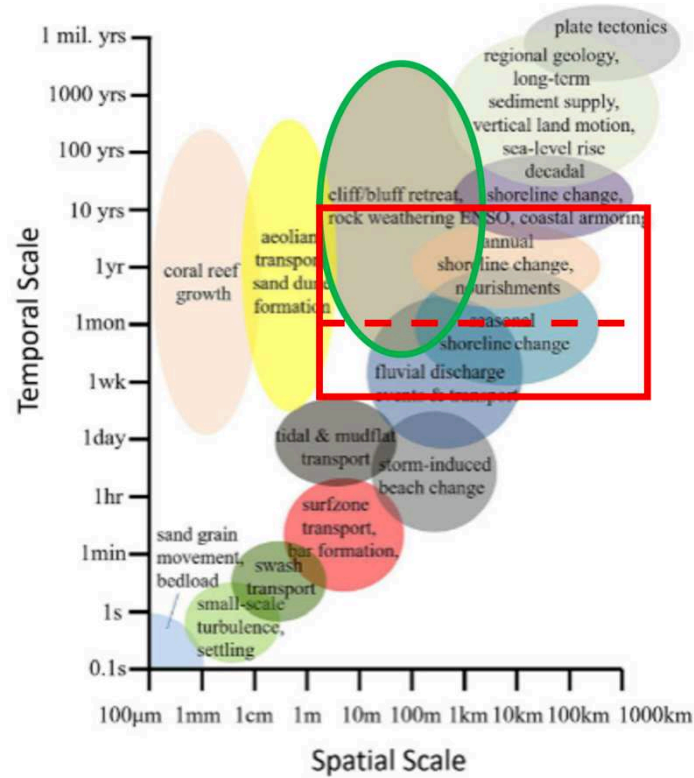


Figure 5.3: A visual representation of the temporal and spatial scale of coastal change processes and CliffSat, based on (Vitousek et al., 2023). In red, the single image technique is shown, in dashed red the composite technique is shown, having a reduced temporal scale.

Because of the temporal and spatial limitations of CliffSat, it is difficult to draw conclusions on what cliff erosion processes, presented in Table 2.1, are dominant for a specific location using the algorithm. The effect of large storms or earthquakes will only be captured if the resulting erosion is over several meters, while it will then still be difficult to find the exact date of the event due to spatial and temporal constraints.

Due to the spatial resolution of the images used, the algorithm can not compete with for example LiDAR measurements on accuracy. However, due to the relatively high temporal resolution of the satellites used, a timeseries can be created and first insights can be obtained on the behavior of a cliff. The algorithm can therefore well be used to determine if a cliff is stable or eroding, and can even give a first estimate on the erosion rates.

To be able to use CliffSat on a new site, a new classifier has to be trained and an investigation will have to be performed to determine the most suitable index to separate the classes. After this, CliffSat can be used to investigate the cliffs behavior. To observe if the cliff is stable or erosive, it is recommended to use composite images. If the cliff shows to have high erosion rates it can be decided to use single images, showing more seasonal variation.

5.5. Wider Contribution

To put this research into perspective, the wider contribution is elaborated. In addition to the overview provided of cliff erosion processes, current monitoring techniques, and the analysis of various spectral indices, the two most significant contributions are: (1) the conclusions regarding the essential components of a successful satellite-derived cliff line algorithm, and (2) the evaluation of a first version of such an algorithm, including potential improvements.

This research could mark the beginning of a new trend in which satellite-based cliff monitoring becomes a widely adopted technique globally. Given its cost-free nature, it currently offers an initial insight into the behavior of coastal cliffs within a system. In the future, as the algorithm is refined or new algorithms are developed, and the accuracy of SDC-algorithms improves, satellite monitoring could potentially become the primary data source for research and engineering projects. It offers the capability to provide long-term insights into coastal systems, which is essential for sustainable planning and management.

Conclusion

Currently, a wide range of satellite-derived shoreline (SDS) algorithms are being used and developed globally, differing in both methodology and output. For instance, some algorithms generate shorelines at pixel resolution, while others achieve sub-pixel resolution using various techniques. Additionally, some rely on single satellite images, whereas others use composite images to mitigate daily or seasonal variations.

Despite these differences, most algorithms are based on similar principles. Satellite images are loaded into the algorithm, after which reflectance values for each spectral band are calculated per pixel. From these values, spectral indices are derived to distinguish between land and water. Based on this separation, a waterline is extracted, followed by optional post-processing steps.

To adapt a SDS-algorithm for cliff line extraction, the most critical modification is the use of a different spectral index. SDS-algorithms typically use MNDWI and NDWI, which are optimized for distinguishing land from water. However, coastal cliffs often feature sandy foreshores and diverse land cover types on the cliff top. Therefore, an index is needed that can differentiate between various land features, sand, and water. This study found that a combination of NDVI — effective in separating vegetation from other land features and water — and the SwiRed index — optimized for detecting built environments — is most effective in distinguishing the cliff top from the beach and sea.

While already present in some SDS-algorithms, the use of composite images is particularly beneficial for cliff line extraction. Since cliffs are relatively stable systems with minimal daily variation (except in cases of sudden collapse), combining multiple images helps eliminate noise from daily and seasonal changes, resulting in a more robust algorithm.

The new SDC-algorithm, called CliffSat, was applied to the Holderness coast in England, resulting in a comparison of 101 transects along the shoreline for which biannual LiDAR data was available. The model was tested using two different approaches: single images and yearly composites. The composite was generated by averaging reflection values for every pixel after filtering out the most significant outliers.

The two methods were evaluated using two metrics: the yearly erosion trend derived from linear regression, and the total amount of erosion measured over the 8-year period. For the yearly trend, both methods performed similarly in terms of bias and standard deviation. For total erosion, the composite method had a slightly higher bias than the single images method, while the standard deviation of the composite was a lot lower, especially for when the erosion recorded by the data was below 10 meters.

When compared to existing SDS-algorithms, the results show that both methods used for CliffSat exhibit a comparable bias and standard deviation for the yearly trend, indicating that they fall within the acceptable performance range. For total erosion, the composite method achieved the lowest standard deviation among all SDS-algorithms used for comparison, while the single-image method also remained within acceptable limits.

Given that CliffSat is based on the SDS-algorithm CoastSat, a direct comparison is particularly relevant. CliffSat and CoastSat performed similarly in estimating yearly erosion trends. However, when evaluating total erosion, both imaging methods of CliffSat outperformed CoastSat — both in its own validation tests and in benchmarking studies conducted in other research.

A deeper analysis of the algorithm's performance revealed several factors influencing its accuracy. Cliff height was found to be a significant factor, with higher cliffs resulting in less accurate model output. Additionally, built environments, campsites, and parking lots were more susceptible to noise in the time series, leading to lower accuracy. Seasonal effects also played a role: farmlands that become bare soil during certain seasons reduced the contrast between sand and the cliff, introducing higher errors into the model.

To conclude, the answers to the sub-questions collectively address the main research question:

How can satellite-derived shoreline detection methods be adapted and applied to extract coastal cliff erosion, and how do these satellite-based measurements compare to in-situ erosion data?

By applying a different combination of spectral indices than those used in existing SDS-algorithms and by creating composite images, it is possible to extract cliff lines from satellite data. The accuracy achieved in comparison to in-situ data falls within the range of existing SDS-algorithms for monitoring erosion trends. Moreover, CliffSat demonstrates improved performance in estimating total erosion rates, making it a valuable tool for long-term coastal monitoring.

Recommendations

In this chapter, recommendations for future research and development are presented. Additionally, the potential for practical implementation of the algorithm is discussed.

7.1. Future research and development

As briefly discussed in Chapter 5, one of the key areas for future research is the spectral index used for cliff line detection. Given the wide variety of cliff types and surface characteristics around the world, it is unlikely that a single index will be suitable for all cases. Therefore, more extensive research into spectral indices is needed to ensure the algorithm can be applied globally. A logical starting point would be to analyze the reflectance values of different land features across spectral bands, which could lead to the development of new, more specialized indices. For example, for fully vegetated cliffs, the NDVI has already proven to be effective. Ideally, a database is made with specific indices for all different cliff types, so that if the cliff type of a new region of interest is established, the right index can be found to run the algorithm.

Another improvement that could be made is the integration of cliff height into the algorithm. This addition could help resolve ambiguities between detecting the cliff top and the cliff face, thereby improving accuracy. However, it is recommended to continue using spectral indices in parallel, as they may offer better performance for cliffs with a low height. By combining height-based and index-based detection, the algorithm could achieve optimal accuracy for medium-height cliffs, while still maintaining reliable performance for both high and low cliffs with distinct surface reflectance characteristics.

Additionally, more research can be conducted on the threshold determination. Currently, Otsu's thresholding method is used by the algorithm to find a threshold between land and sand. However, it was found that due to errors in the classification process, the threshold calculation is influenced, resulting in variation in the cliff line position. To eliminate this variation, apart from extensively training a classifier, a new thresholding method should be found that is more robust against errors in the classification process.

Beyond algorithmic improvements, another direction for development is the use of higher-resolution satellite imagery. As concluded in this study, the observed error margins are closely related to the spatial resolution of the satellite data. This suggests that using finer-resolution imagery could enhance accuracy. A key strength of the current algorithm is its accessibility and cost-effectiveness, so any improvements in resolution should ideally not introduce significant costs. Fortunately, higher-resolution imagery is already available for free under certain conditions, such as for research or educational purposes (Planet Labs PBC, 2025), indicating that this improvement could be implemented in the near future.

7.2. Implementation of the algorithm

To conclude this research, it is important to consider how CliffSat can be practically applied by engineering firms such as Haskoning, or for academic and research purposes. Based on the results, it can be concluded that the algorithm performs with a level of accuracy comparable to widely used SDS-algorithms. This makes it suitable for providing an initial understanding of how a coastal cliff system behave over time. However, it is not yet accurate enough to support definitive conclusions — such as determining whether a cliff is entirely stable or calculating precise erosion rates — based solely on its output.

Another aspect of implementation is becoming familiar with the algorithm's settings. Several parameters can be adjusted to influence the results, such as the maximum allowed cloud cover in the imagery, the minimum length required for a valid cliff line, or the maximum cross-shore distance allowed between cliff lines across time steps. By experimenting with these parameters and analyzing their impact on the output, users can fine-tune the algorithm for specific locations. If this process is repeated across multiple sites with available ground-truth data, the model can be continuously calibrated and validated.

Finally, it is worth exploring additional applications for the algorithm. Since it is designed to detect the boundary between sand or water and other land features, it could potentially be adapted to monitor other coastal systems. For example, it may be used to track the development of mangroves with sandy or muddy foreshores, or to observe changes in dune vegetation, as illustrated in Figure 7.1.

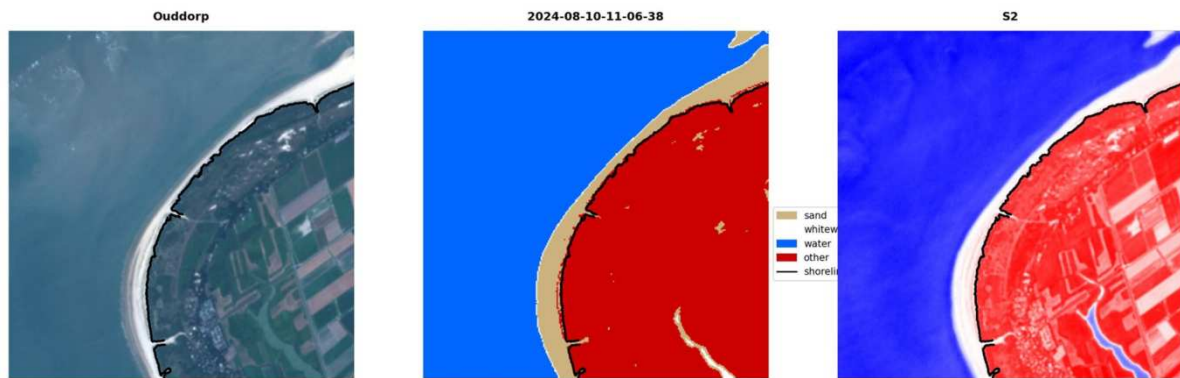


Figure 7.1: Output of CliffSat for a location in the Netherlands, Ouddorp, showing that the algorithm is able to detect the vegetation line in dune systems, without changing any settings, proving this could be another purpose the algorithm can fulfill.

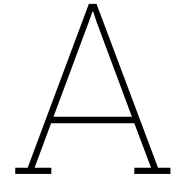
References

- Aagaard, T., Kroon, A., Andersen, S., Sørensen, R. M., Quartel, S., & Vinther, N. (2005). Intertidal beach change during storm conditions; Egmond, The Netherlands. *Marine Geology*, 218(1-4), 65–80. <https://doi.org/10.1016/j.margeo.2005.04.001>
- Alessio, P., & Keller, E. A. (2020). Short-term patterns and processes of coastal cliff erosion in Santa Barbara, California. *Geomorphology*, 353. <https://doi.org/10.1016/j.geomorph.2019.106994>
- Almeida, L. P., Efraim de Oliveira, I., Lyra, R., Scaranto Dazzi, R. L., Martins, V. G., & Henrique da Fontoura Klein, A. (2021). Coastal Analyst System from Space Imagery Engine (CASSIE): Shoreline management module. *Environmental Modelling and Software*, 140. <https://doi.org/10.1016/j.envsoft.2021.105033>
- Baptista, P., Cunha, T., Bernardes, C., Gama, C., Ferreira, Ó., & Dias, A. (2011). A Precise and Efficient Methodology to Analyse the Shoreline Displacement Rate. *Journal of Coastal Research*, 27(2), 223–232. <https://doi.org/10.2112/09-1187.1>
- Bhandari, A., Kumar, A., & Singh, G. (2012). Feature Extraction using Normalized Difference Vegetation Index (NDVI): A Case Study of Jabalpur City. *Procedia Technology*, 6, 612–621. <https://doi.org/10.1016/j.protcy.2012.10.074>
- Bird, E. (2008). *Coastal Geomorphology: An Introduction*.
- Bird, E. (2016). *Coastal Cliffs: Morphology and Management*. Springer. <https://doi.org/10.1007/978-3-319-29084-3>
- Bloom, C. K., Singeisen, C., Stahl, T., Howell, A., & Massey, C. (2023). Earthquake contributions to coastal cliff retreat. *Earth Surface Dynamics*, 11(4), 757–778. <https://doi.org/10.5194/esurf-11-757-2023>
- Bosboom, J., & Stive, M. (2023, January). *Coastal dynamics*. (1.2). Delft University of Technology. <https://doi.org/10.5074/T.2021.001>
- Burvingt, O., & Castelle, B. (2023). Storm response and multi-annual recovery of eight coastal dunes spread along the Atlantic coast of Europe. *Geomorphology*, 435. <https://doi.org/10.1016/j.geomorph.2023.108735>
- Capolupo, A., Monterisi, C., & Tarantino, E. (2020). Landsat Images Classification Algorithm (LICA) to automatically extract land cover information in Google Earth Engine environment. *Remote Sensing*, 12(7). <https://doi.org/10.3390/rs12071201>
- Chen, W., Liu, L., Zhang, C., Wang, J., Wang, J., & Pan, Y. (2004). Monitoring the seasonal bare soil areas in beijing using multitemporal tm images. *IGARSS 2004. 2004 IEEE International Geoscience and Remote Sensing Symposium*, 5, 3379–3382 vol.5. <https://doi.org/10.1109/IGARSS.2004.1370429>
- Cipolletti, M. P., Delrieux, C. A., Perillo, G. M., & Cintia Piccolo, M. (2012). Superresolution border segmentation and measurement in remote sensing images. *Computers and Geosciences*, 40, 87–96. <https://doi.org/10.1016/j.cageo.2011.07.015>
- Dawson, R. J., Dickson, M. E., Nicholls, R. J., Hall, J. W., Walkden, M. J., Stansby, P. K., Mokrech, M., Richards, J., Zhou, J., Milligan, J., Jordan, A., Pearson, S., Rees, J., Bates, P. D., Koukoulas, S., & Watkinson, A. R. (2009). Integrated analysis of risks of coastal flooding and cliff erosion under scenarios of long term change. *Climatic Change*, 95(1-2), 249–288. <https://doi.org/10.1007/s10584-008-9532-8>
- Earlie, C., Masselink, G., & Russell, P. (2018). The role of beach morphology on coastal cliff erosion under extreme waves. *Earth Surface Processes and Landforms*, 43(6), 1213–1228. <https://doi.org/10.1002/esp.4308>
- Earlie, C. S., Masselink, G., Russell, P. E., & Shail, R. K. (2015). Application of airborne LiDAR to investigate rates of recession in rocky coast environments. *Journal of Coastal Conservation*, 19(6), 831–845. <https://doi.org/10.1007/s11852-014-0340-1>
- East Riding Coastal Monitoring Programme. (2024, August). Programme background. <https://coastalmonitoring.org/eastriding/>

- Emery, K. O., & Kuhn, G. G. (1982, July). *Sea cliffs: Their processes, profiles, and classification* (tech. rep.). <http://pubs.geoscienceworld.org/gsa/gsabulletin/article-pdf/93/7/644/3444719/i0016-7606-93-7-644.pdf>
- Emery, K. (1961). A simple method of measuring beach profiles. *Limnology and oceanography*, 6, 90–93. <https://doi.org/10.5894/rgci283>
- European Space Agency. (2024, November). How do radar satellites work? [ESA Multimedia]. https://www.esa.int/ESA_Multimedia/Videos/2024/11/How_do_radar_satellites_work
- European Space Agency. (2025). Sentinel-2. https://www.esa.int/Applications/Observing_the_Earth/Copernicus/Sentinel-2
- Fellowes, T. E., Vila-Concejo, A., Gallop, S. L., Harley, M. D., & Short, A. D. (2022). Wave shadow zones as a primary control of storm erosion and recovery on embayed beaches. *Geomorphology*, 399. <https://doi.org/10.1016/j.geomorph.2021.108072>
- Ford, M. (2013). Shoreline changes interpreted from multi-temporal aerial photographs and high resolution satellite images: Wotje Atoll, Marshall Islands. *Remote Sensing of Environment*, 135, 130–140. <https://doi.org/10.1016/j.rse.2013.03.027>
- Gao, B.-C. (1996). *Naval Research Laboratory, 4555 Overlook Ave* (tech. rep.). ©Elsevier Science Inc.
- Global GPS Systems. (2022, August). Rtk gps: Understanding real-time kinematic gps technology [Global GPS Systems]. <https://globalgpsystems.com/gnss/rtk-gps-understanding-real-time-kinematic-gps-technology/>
- Google Maps. (2025, June). East riding of yorkshire, google maps. https://www.google.nl/maps/place/East+Riding+of+Yorkshire,+Verenigd+Koninkrijk/@52.3734597,-2.9134822,6.84z/data=!4m6!3m5!1s0x47d61ff4fb633759:0x718657d37a09419c!8m2!3d53.8215889!4d-0.7189977!16zL20vMDE0MTYy?hl=nl&entry=tту&g_ep=EgoyMDI1MDUyOC4wIKXMDSoASAFQAw%3D%3D
- Gorelick, N., Hancher, M., Dixon, M., Ilyushchenko, S., Thau, D., & Moore, R. (2017). Google Earth Engine: Planetary-scale geospatial analysis for everyone. *Remote Sensing of Environment*, 202, 18–27. <https://doi.org/10.1016/j.rse.2017.06.031>
- Great Ocean Road Coast and Parks Authority. (2024, October). Authority monitoring recent coastal erosion [Great Ocean Road Coast and Parks Authority]. <https://www.greatoceanroadauthority.vic.gov.au/Latest-News/Authority-monitoring-recent-coastal-erosion>
- Hagenaars, G., de Vries, S., Luijendijk, A. P., de Boer, W. P., & Reniers, A. J. (2018). On the accuracy of automated shoreline detection derived from satellite imagery: A case study of the sand motor mega-scale nourishment. *Coastal Engineering*, 133, 113–125. <https://doi.org/10.1016/j.coastaleng.2017.12.011>
- Hall, A. M., Hansom, J. D., & Jarvis, J. (2008). Patterns and rates of erosion produced by high energy wave processes on hard rock headlands: The Grind of the Navir, Shetland, Scotland. *Marine Geology*, 248(1-2), 28–46. <https://doi.org/10.1016/j.margeo.2007.10.007>
- Harley, M. D., Turner, I. L., Short, A. D., & Ranasinghe, R. (2011). Assessment and integration of conventional, RTK-GPS and image-derived beach survey methods for daily to decadal coastal monitoring. *Coastal Engineering*, 58(2), 194–205. <https://doi.org/10.1016/j.coastaleng.2010.09.006>
- Harrison, A. J., Miller, B. M., Carley, J. T., Turner, I. L., Clout, R., & Coates, B. (2017). *NSW Beach Photogrammetry: A New Online Database and Toolbox* (tech. rep.). www.nswbpd.wrl.unsw.edu.au
- He, C., & Xie, D. (2010, December). *IMPROVING THE NORMALIZED DIFFERENCE BUILD-UP INDEX TO MAP URBAN BUILD-UP AREAS BY USING A SEMIAUTOMATIC SEGMENTATION APPROACH* (tech. rep.).
- Holman, R. A., & Stanley, J. (2007). The history and technical capabilities of Argus. *Coastal Engineering*, 54(6-7), 477–491. <https://doi.org/10.1016/j.coastaleng.2007.01.003>
- Javed, A., Cheng, Q., Peng, H., Altan, O., Li, Y., Ara, I., Huq, E., Ali, Y., & Saleem, N. (2021). Review of spectral indices for urban remote sensing. *Photogrammetric Engineering and Remote Sensing*, 87(7), 513–524. <https://doi.org/10.14358/PERS.87.7.513>
- Jieli, C., Manchun, L., Yongxue, L., Chenglei, S., & Wei, H. (2010). Extract residential areas automatically by new built-up index. *2010 18th International Conference on Geoinformatics*, 1–5. <https://doi.org/10.1109/GEOINFORMATICS.2010.5567823>

- Kline, S. W., Adams, P. N., & Limber, P. W. (2014). The unsteady nature of sea cliff retreat due to mechanical abrasion, failure and comminution feedbacks. *Geomorphology*, 219, 53–67. <https://doi.org/10.1016/j.geomorph.2014.03.037>
- Kregar, K., & Kozmus Trajkovski, K. (2025). Combining UAV Photogrammetry and TLS for Change Detection on Slovenian Coastal Cliffs. *Drones*, 9(4). <https://doi.org/10.3390/drones9040228>
- Laksono, A., Saputri, A. A., Pratiwi, C. I. B., Arkan, M. Z., & Putri, R. F. (2020). Vegetation covers change and its impact on Barchan Dune morphology in Parangtritis Coast, Indonesia. *E3S Web of Conferences*, 200. <https://doi.org/10.1051/e3sconf/202020002026>
- Lanza, A., Sullenberger, R. M., Chen, J. G., & Hopkins, J. (2023, September). *EXPANDING COAST-SAT SHORELINE DETECTION ALGORITHM TO TRACK COASTAL VEGETATION AND URBAN CHARACTERISTICS FROM SATELLITE DATA* (tech. rep.).
- Larson, M., & Kraus, N. C. (1995). *Prediction of cross-shore sediment transport and temporal scales at different spatial* (tech. rep.).
- Leisner, M. M., de Paula, D. P., de Carvalho, R. G., Holanda Bastos, F. d., Albuquerque, M. d. G., Vasconcelos, Y. G., Leal-Alves, D. C., & Onofre de Moraes, J. (2025). Mass movement hazard assessment of active coastal cliffs (Northeast Brazil). *Ocean and Coastal Management*, 263. <https://doi.org/10.1016/j.ocecoaman.2025.107596>
- Lin, H., Wang, J., Liu, S., Qu, Y., & Wan, H. (2005). Studies on urban areas extraction from Landsat TM images. *International Geoscience and Remote Sensing Symposium (IGARSS)*, 6, 3826–3829. <https://doi.org/10.1109/IGARSS.2005.1525743>
- Los Angeles Times. (2022, August). The california coast is disappearing under the rising sea. our choices are grim [Los Angeles Times]. <https://www.latimes.com/projects/la-me-sea-level-rise-california-coast/>
- Luijendijk, A., Hagenaars, G., Ranasinghe, R., Baart, F., Donchyts, G., & Aarninkhof, S. (2018). The State of the World's Beaches. *Scientific Reports*, 8(1). <https://doi.org/10.1038/s41598-018-24630-6>
- Mao, Y., Harris, D. L., Xie, Z., & Phinn, S. (2021). Efficient measurement of large-scale decadal shoreline change with increased accuracy in tide-dominated coastal environments with Google Earth Engine. *ISPRS Journal of Photogrammetry and Remote Sensing*, 181, 385–399. <https://doi.org/10.1016/j.isprsjprs.2021.09.021>
- Middleton, J. H., Cooke, C. G., Kearney, E. T., Mumford, P. J., Mole, M. A., Nippard, G. J., Rizos, C., Splinter, K. D., & Turner, I. L. (2013). Resolution and accuracy of an airborne scanning laser system for beach surveys. *Journal of Atmospheric and Oceanic Technology*, 30(10), 2452–2464. <https://doi.org/10.1175/JTECH-D-12-00174.1>
- NASA. (2025). Landsat science satellites. <https://landsat.gsfc.nasa.gov/satellites/>
- Nguyen, C. T., Chidthaisong, A., Diem, P. K., & Huo, L. Z. (2021). A modified bare soil index to identify bare land features during agricultural fallow-period in southeast asia using landsat 8. *Land*, 10(3), 1–18. <https://doi.org/10.3390/land10030231>
- NOS. (2022, February). Klimaatverandering: Het britse dorp dat wordt opgeslokt door de zee [NOS Nieuws]. <https://nos.nl/artikel/2419295>
- NOS. (2023, March). Normandische kust bedreigd: Regio wil bewoners en bedrijven verhuizen [NOS Nieuws]. <https://nos.nl/artikel/2465745-normandische-kust-bedreigd-regio-wil-bewoners-en-bedrijven-verhuizen>
- Obu, J., Lantuit, H., Grosse, G., Günther, F., Sachs, T., Helm, V., & Fritz, M. (2017). Coastal erosion and mass wasting along the Canadian Beaufort Sea based on annual airborne LiDAR elevation data. *Geomorphology*, 293, 331–346. <https://doi.org/10.1016/j.geomorph.2016.02.014>
- Otsu, N. (1979). A Threshold Selection Method from Gray-Level Histograms. *Transactions on systems, man, and cybernetics*, 1, 62–66.
- Palomar-Vázquez, J., Pardo-Pascual, J. E., Almonacid-Caballer, J., & Cabezas-Rabadán, C. (2023). Shoreline Analysis and Extraction Tool (SAET): A New Tool for the Automatic Extraction of Satellite-Derived Shorelines with Subpixel Accuracy. *Remote Sensing*, 15(12). <https://doi.org/10.3390/rs15123198>
- Pardo-Pascual, J. E., Sánchez-García, E., Almonacid-Caballer, J., Palomar-Vázquez, J. M., de los Santos, E. P., Fernández-Sarriá, A., & Balaguer-Beser, Á. (2018). Assessing the accuracy of automatically extracted shorelines on microtidal beaches from landsat 7, landsat 8 and sentinel-2 imagery. *Remote Sensing*, 10(2). <https://doi.org/10.3390/rs10020326>

- Pianca, C., Holman, R., & Siegle, E. (2015). Shoreline variability from days to decades: Results of long-term video imaging. *Journal of Geophysical Research: Oceans*, 120(3), 2159–2178. <https://doi.org/10.1002/2014JC010329>
- Planet Labs PBC. (2025). Planet: Daily satellite data and insights. <https://www.planet.com/>
- Pye, K., & Blott, S. J. (2015). Spatial and temporal variations in soft-cliff erosion along the Holderness coast, East Riding of Yorkshire, UK. *Journal of Coastal Conservation*, 19(6), 785–808. <https://doi.org/10.1007/s11852-015-0378-8>
- Rasul, A., Balzter, H., Ibrahim, G. R., Hameed, H. M., Wheeler, J., Adamu, B., Ibrahim, S., & Najmaddin, P. M. (2018). Applying built-up and bare-soil indices from Landsat 8 to cities in dry climates. *Land*, 7(3). <https://doi.org/10.3390/land7030081>
- Sánchez-García, E., Palomar-Vázquez, J. M., Pardo-Pascual, J. E., Almonacid-Caballer, J., Cabezas-Rabadán, C., & Gómez-Pujol, L. (2020). An efficient protocol for accurate and massive shoreline definition from mid-resolution satellite imagery. *Coastal Engineering*, 160. <https://doi.org/10.1016/j.coastaleng.2020.103732>
- Space Shift Inc. (2024). Satellites – technology overview [Space Shift]. <https://www.spcsft.com/en/technology-en/satellites-en/>
- Swirad, Z. M., & Young, A. P. (2022). Spatial and temporal trends in California coastal cliff retreat. *Geomorphology*, 412. <https://doi.org/10.1016/j.geomorph.2022.108318>
- U.S. Geological Survey. (2025a). Landsat satellite missions. <https://www.usgs.gov/landsat-missions/landsat-satellite-missions>
- U.S. Geological Survey. (2025b). What is remote sensing and what is it used for? <https://www.usgs.gov/faqs/what-remote-sensing-and-what-it-used>
- Vitousek, S., Buscombe, D., Vos, K., Barnard, P. L., Ritchie, A. C., & Warrick, J. A. (2023). The future of coastal monitoring through satellite remote sensing. *Cambridge Prisms: Coastal Futures*, 1. <https://doi.org/10.1017/cft.2022.4>
- Vos, K., Splinter, K. D., Palomar-Vázquez, J., Pardo-Pascual, J. E., Almonacid-Caballer, J., Cabezas-Rabadán, C., Kras, E. C., Luijendijk, A. P., Calkoen, F., Almeida, L. P., Pais, D., Klein, A. H., Mao, Y., Harris, D., Castelle, B., Buscombe, D., & Vitousek, S. (2023). Benchmarking satellite-derived shoreline mapping algorithms. *Communications Earth and Environment*, 4(1). <https://doi.org/10.1038/s43247-023-01001-2>
- Vos, K., Splinter, K. D., Harley, M. D., Simmons, J. A., & Turner, I. L. (2019). CoastSat: A Google Earth Engine-enabled Python toolkit to extract shorelines from publicly available satellite imagery. *Environmental Modelling and Software*, 122. <https://doi.org/10.1016/j.envsoft.2019.104528>
- Waqar, M. M., Mumtaz, R., & Hussain, E. (2012). Development of new indices for extraction of built-up area and bare soil from landsat. <https://doi.org/10.4172/scientificreports.136>
- Weitkamp, C. (2005, July). *Lidar: Range-resolved optical remote sensing of the atmosphere*. Springer New York.
- Westoby, M. J., Lim, M., Hogg, M., Pound, M. J., Dunlop, L., & Woodward, J. (2018). Cost-effective erosion monitoring of coastal cliffs. *Coastal Engineering*, 138, 152–164. <https://doi.org/10.1016/j.coastaleng.2018.04.008>
- Xu, H. (2006). Modification of normalised difference water index (NDWI) to enhance open water features in remotely sensed imagery. *International Journal of Remote Sensing*, 27(14), 3025–3033. <https://doi.org/10.1080/01431160600589179>
- Young, A. P., Guza, R. T., Matsumoto, H., Merrifield, M. A., O'Reilly, W. C., & Swirad, Z. M. (2021). Three years of weekly observations of coastal cliff erosion by waves and rainfall. *Geomorphology*, 375. <https://doi.org/10.1016/j.geomorph.2020.107545>
- Young, A. P., & Carilli, J. E. (2019). Global distribution of coastal cliffs. *Earth Surface Processes and Landforms*, 44(6), 1309–1316. <https://doi.org/10.1002/esp.4574>
- Yuan, R., Kennedy, D. M., Stephenson, W. J., & Finlayson, B. L. (2024). The influence of weathering processes on microtopographic changes of sandstone under simulated upper intertidal conditions from weekly to monthly scales. *Geomorphology*, 455. <https://doi.org/10.1016/j.geomorph.2024.109209>
- Zha, Y., Gao, J., & Ni, S. (2003). Use of normalized difference built-up index in automatically mapping urban areas from TM imagery. *International Journal of Remote Sensing*, 24(3), 583–594. <https://doi.org/10.1080/01431160304987>



Spectral index comparison

In this section, the spectral index comparison is performed. This comparison is done based on the visual distinction in index, visible in the right picture for every image, and the PDF, visible at the bottom of every image. This comparison is executed for eleven different indices. In this appendix, two different seasons are presented (June and September).

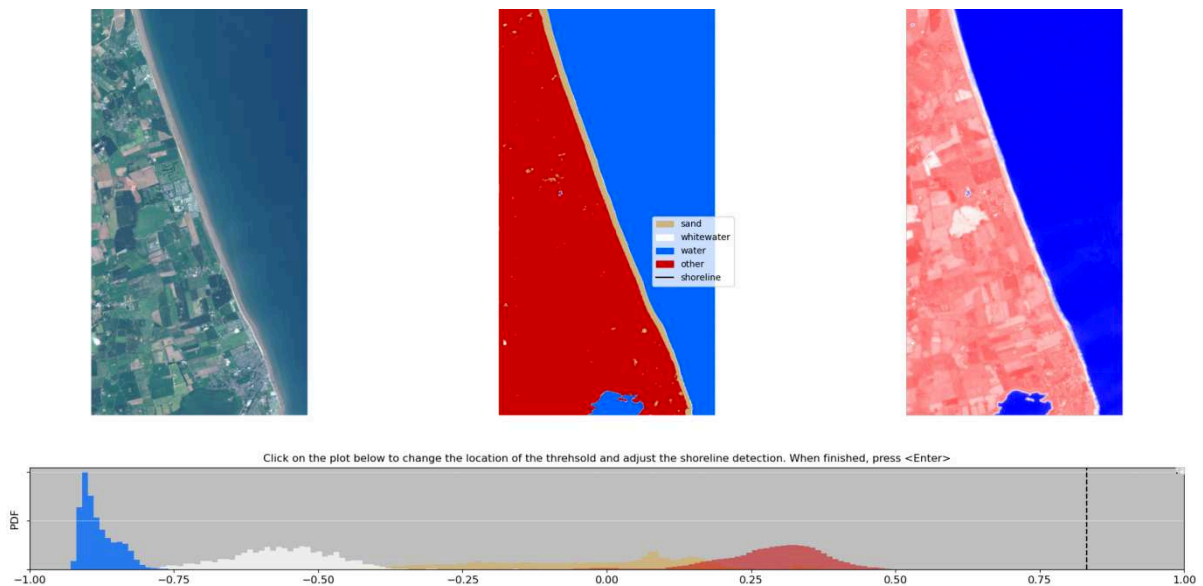


Figure A.1: MNDWI 24-06-2024

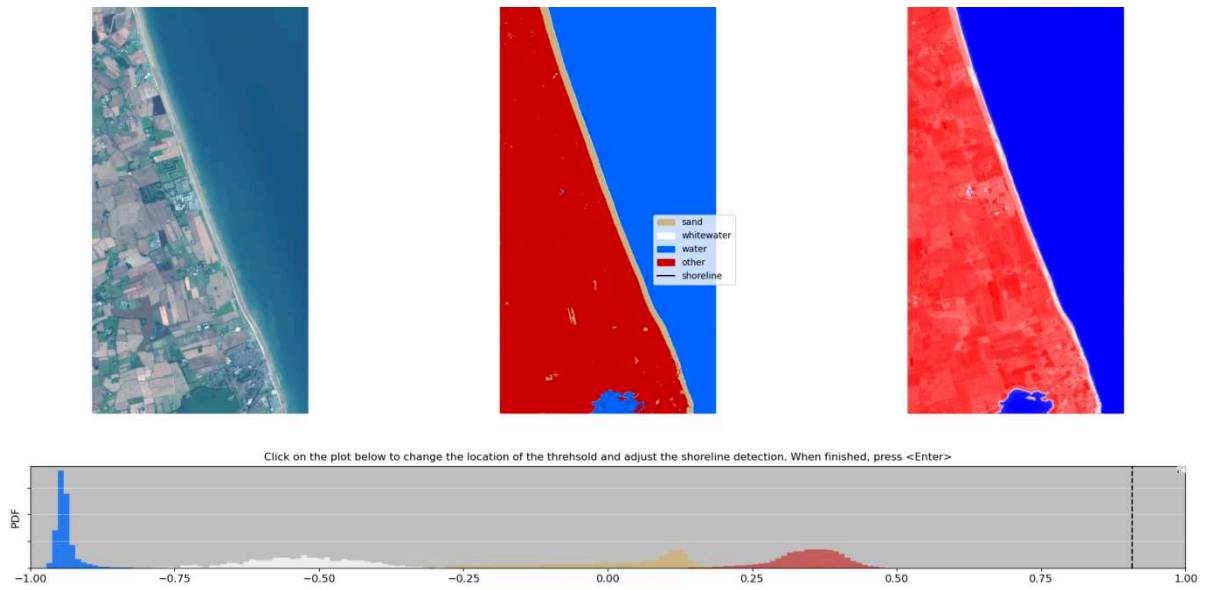


Figure A.2: MNDWI 17-09-2024

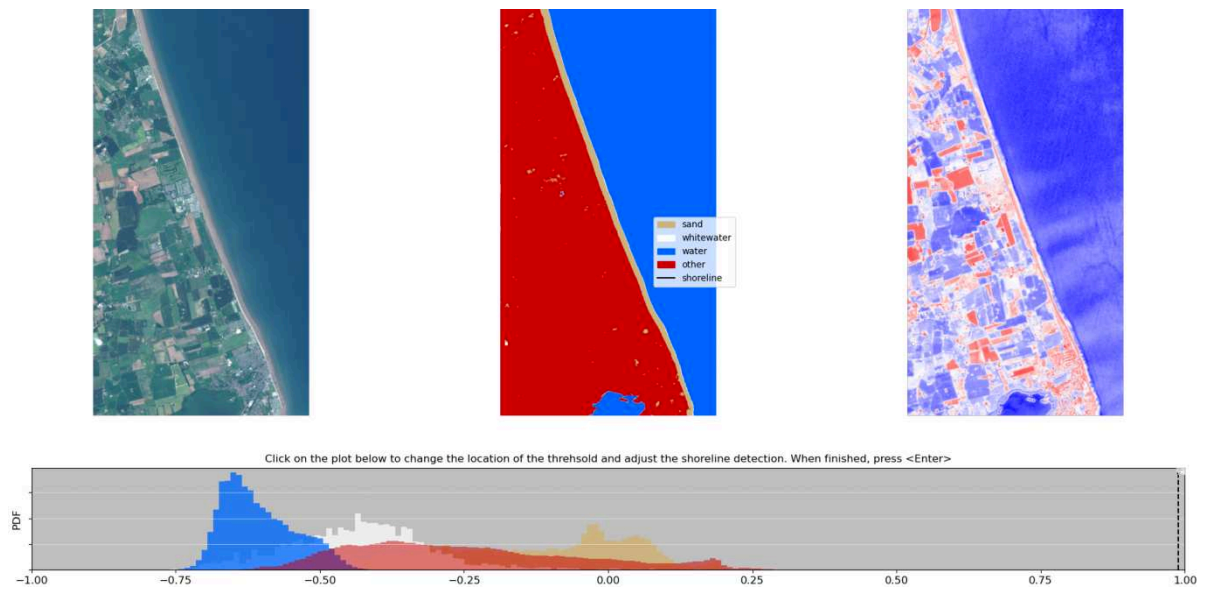


Figure A.3: NDBI 24-06-2024

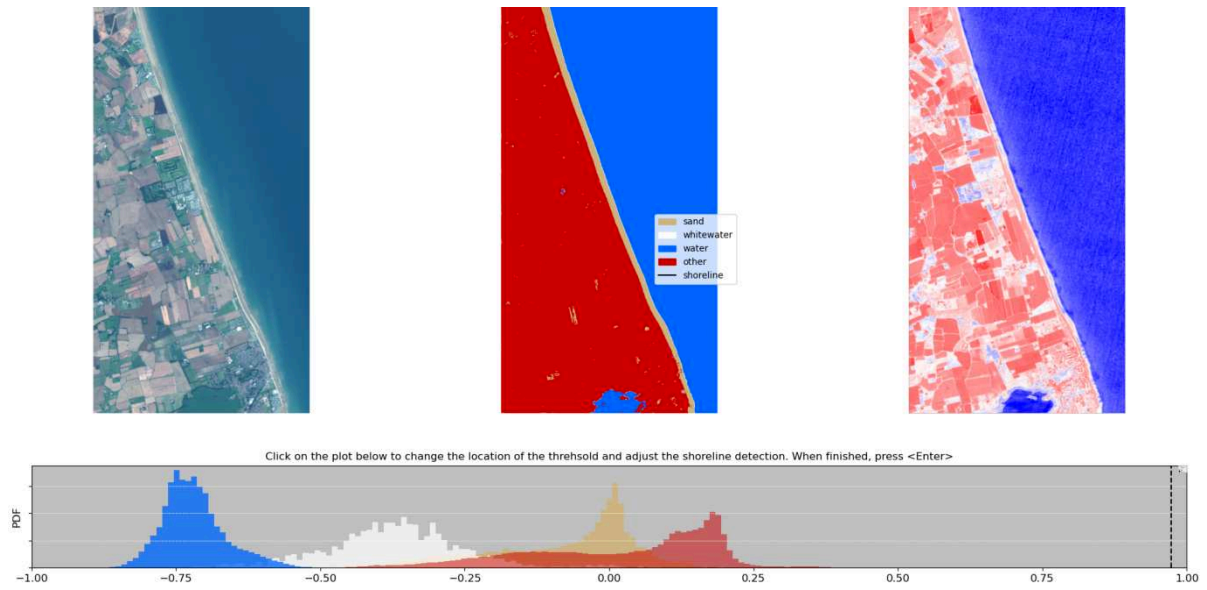


Figure A.4: NDBI 17-09-2024

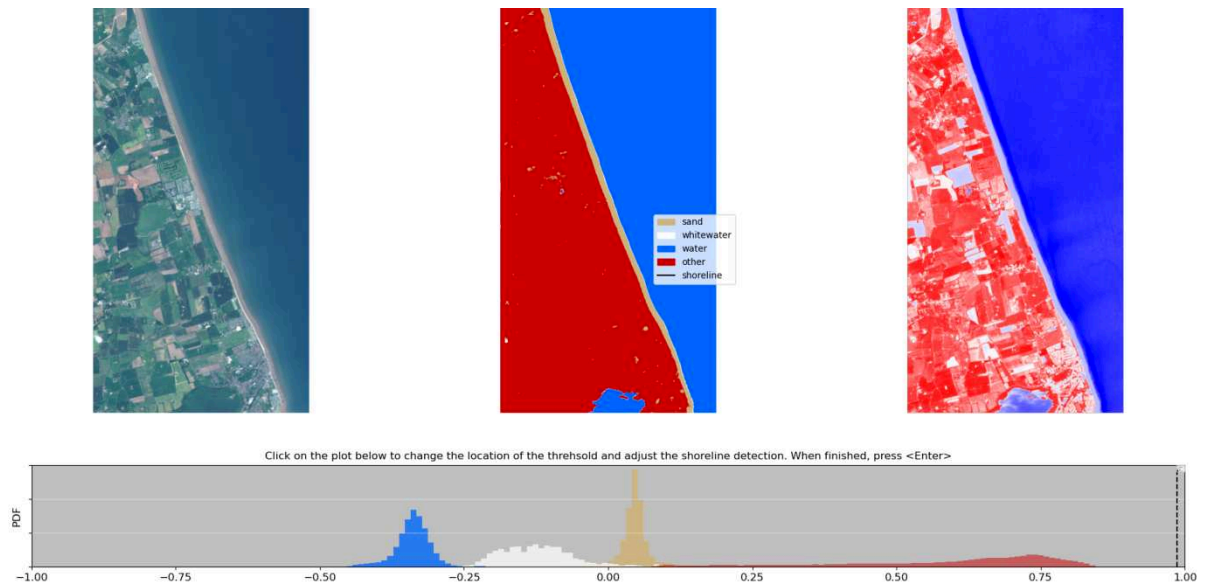


Figure A.5: NDVI 24-06-2024

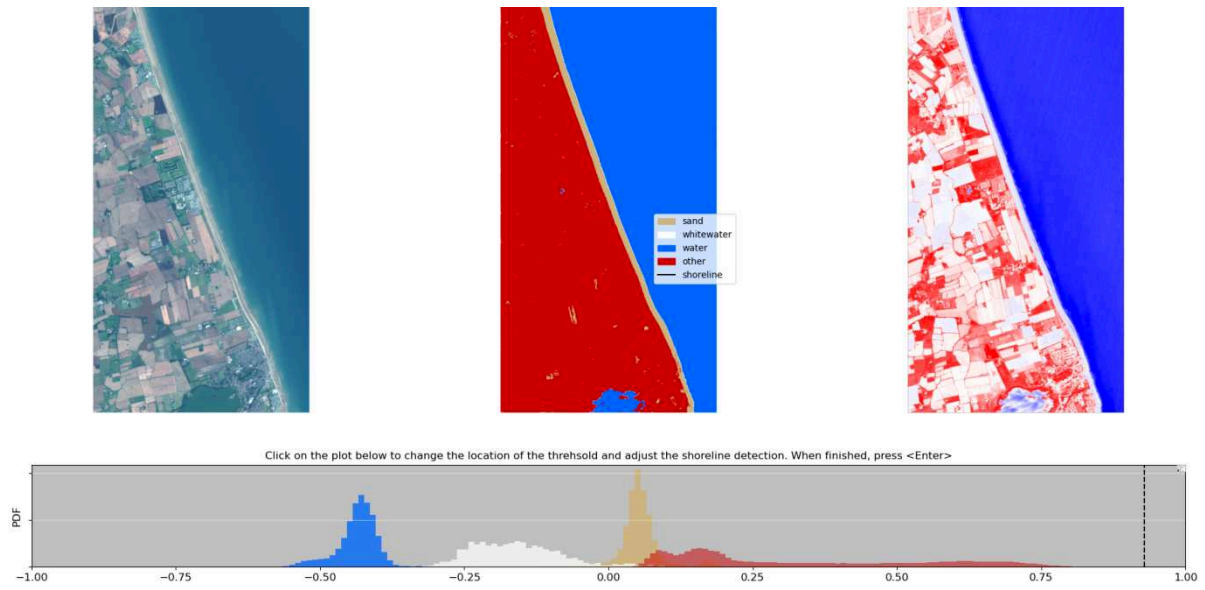


Figure A.6: NDVI 17-09-2024

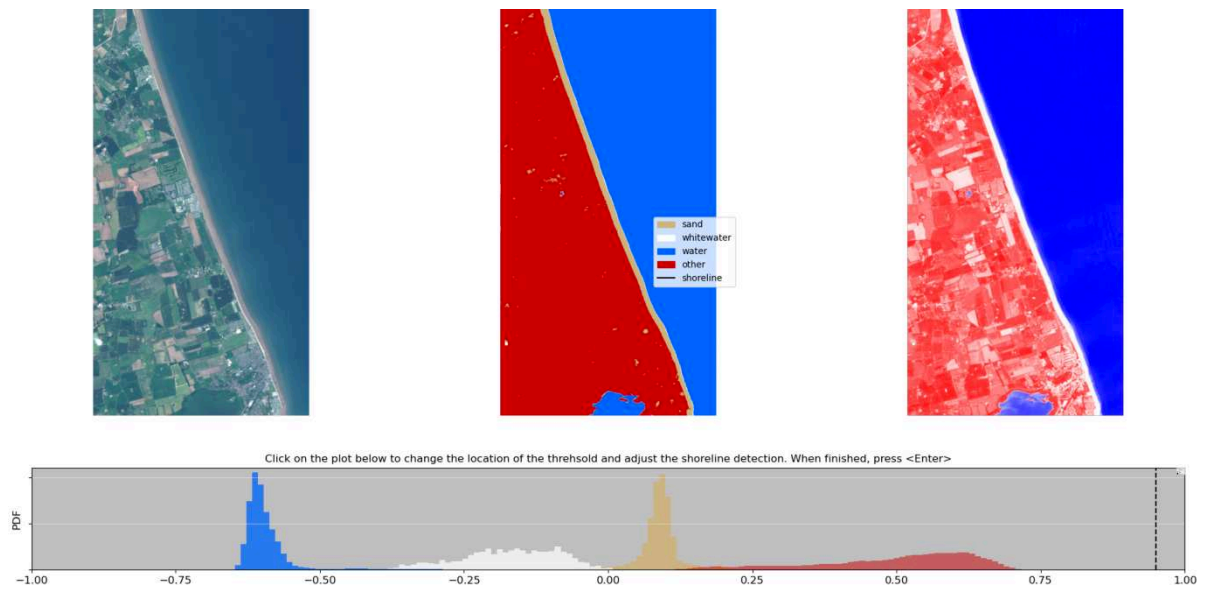


Figure A.7: NDWI 24-06-2024

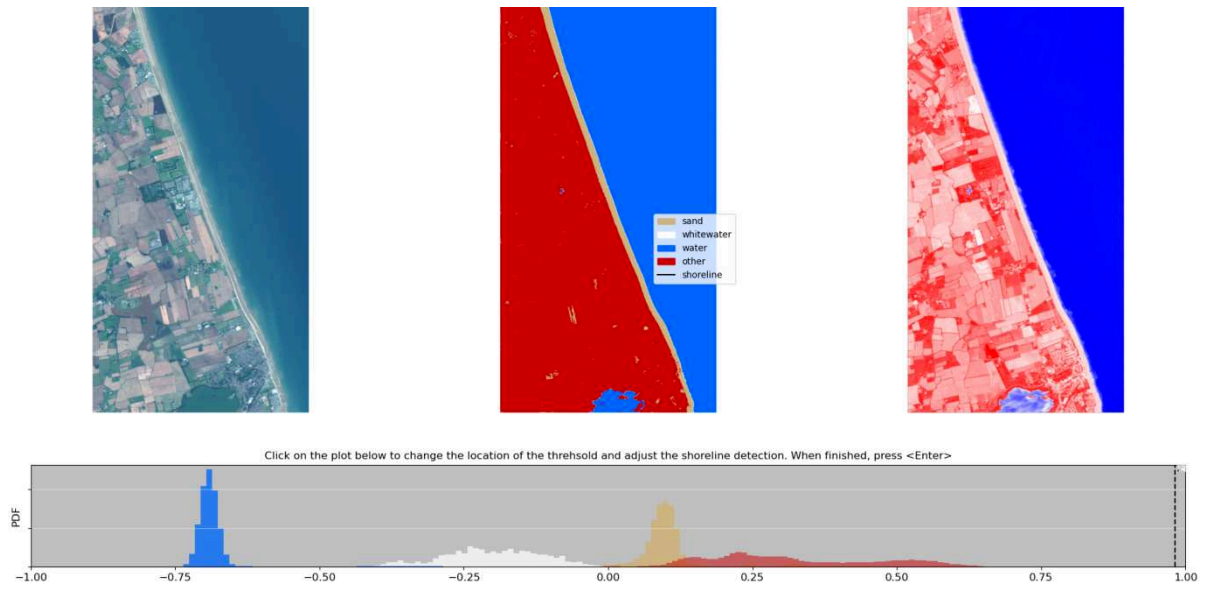


Figure A.8: NDWI 17-09-2024

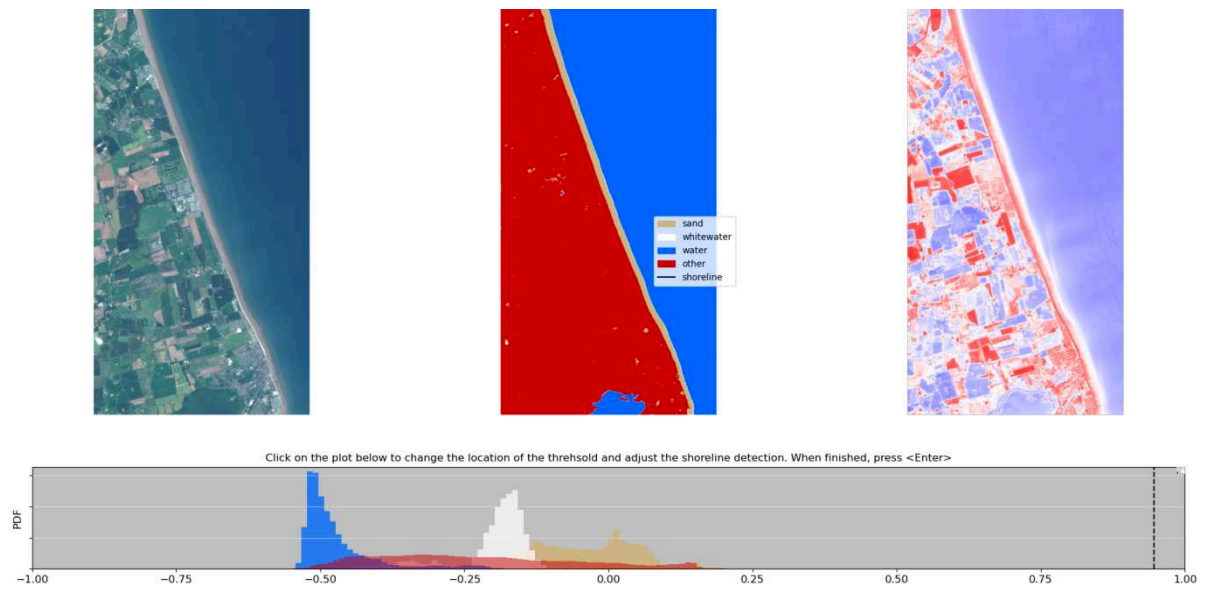


Figure A.9: BSI 24-06-2024

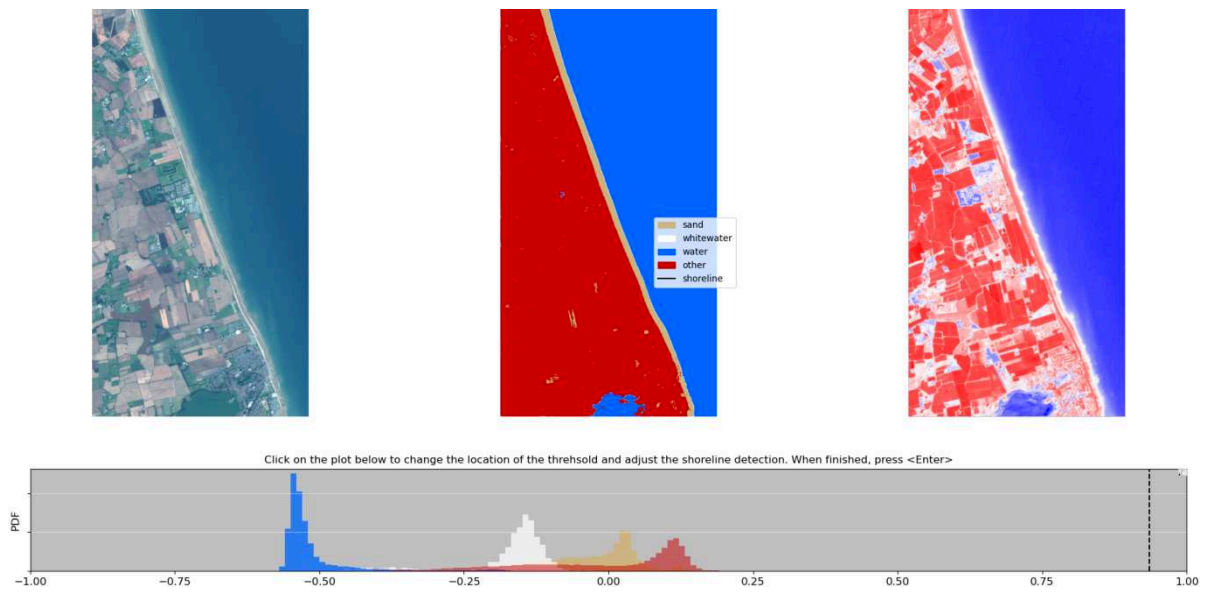


Figure A.10: BSI 17-09-2024

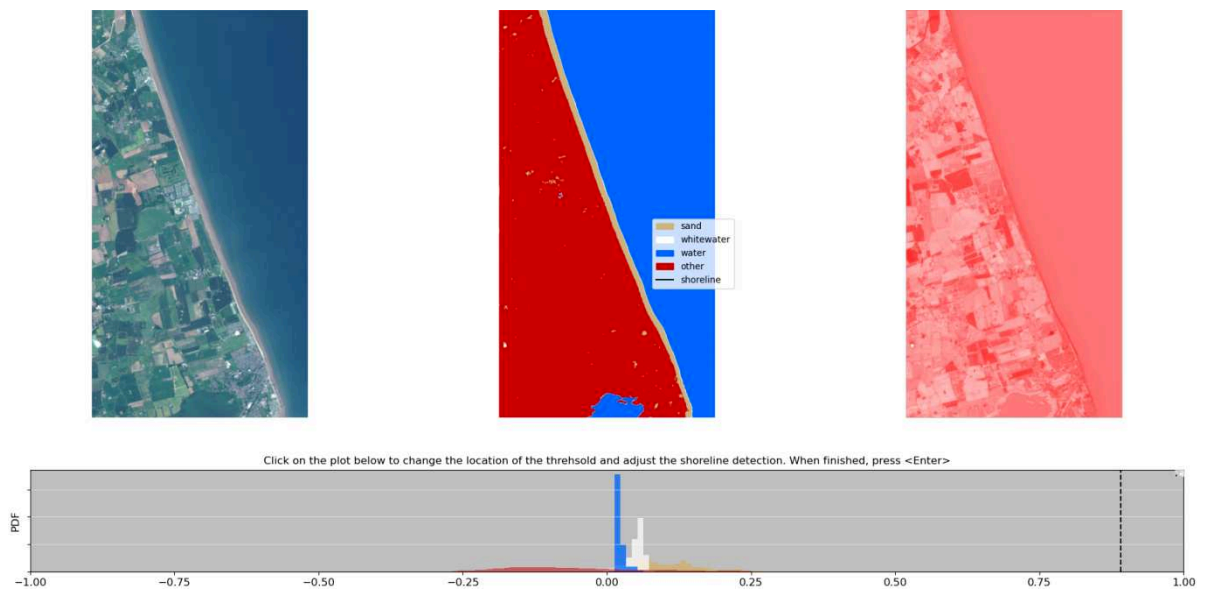


Figure A.11: BI 24-06-2024

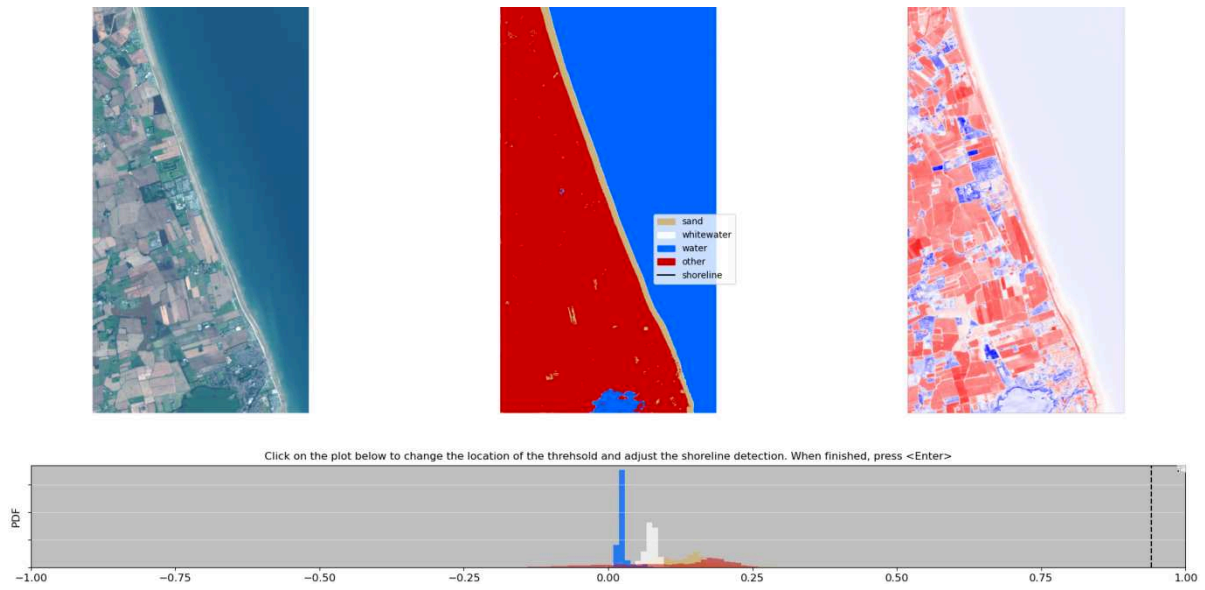


Figure A.12: BI 17-09-2024

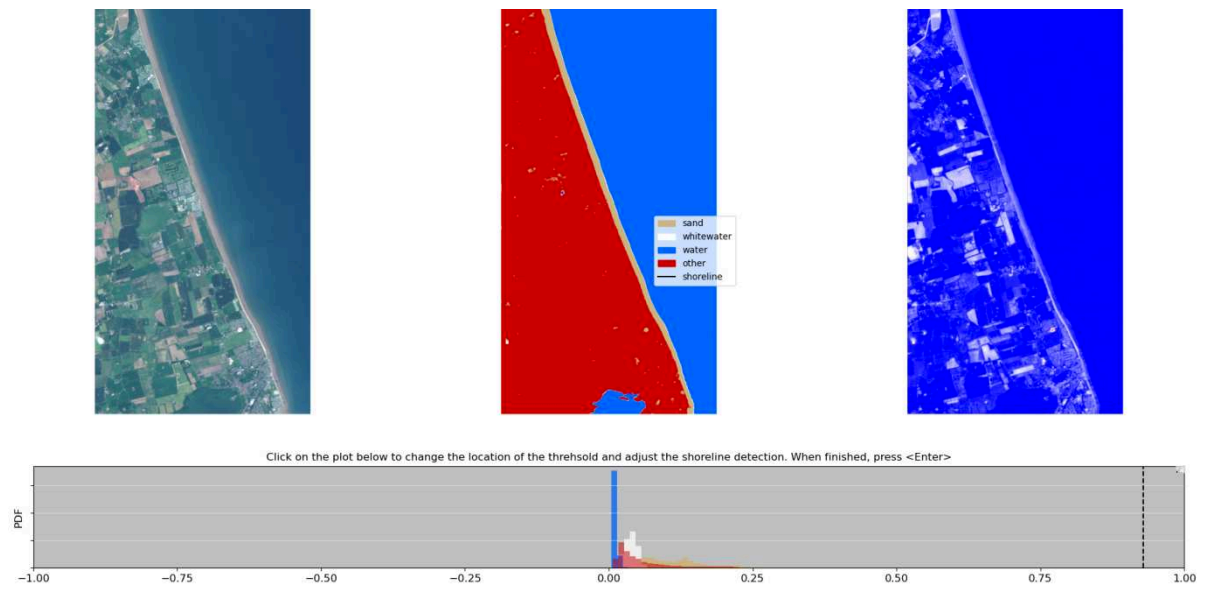


Figure A.13: NBI 24-06-2024

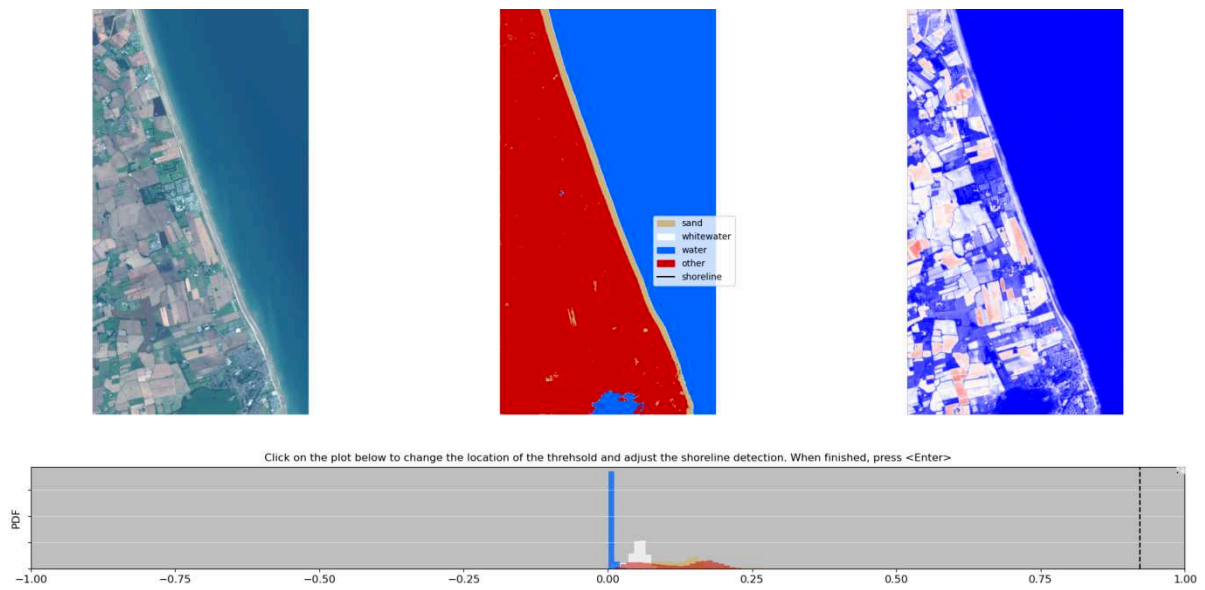


Figure A.14: NBI 17-09-2024

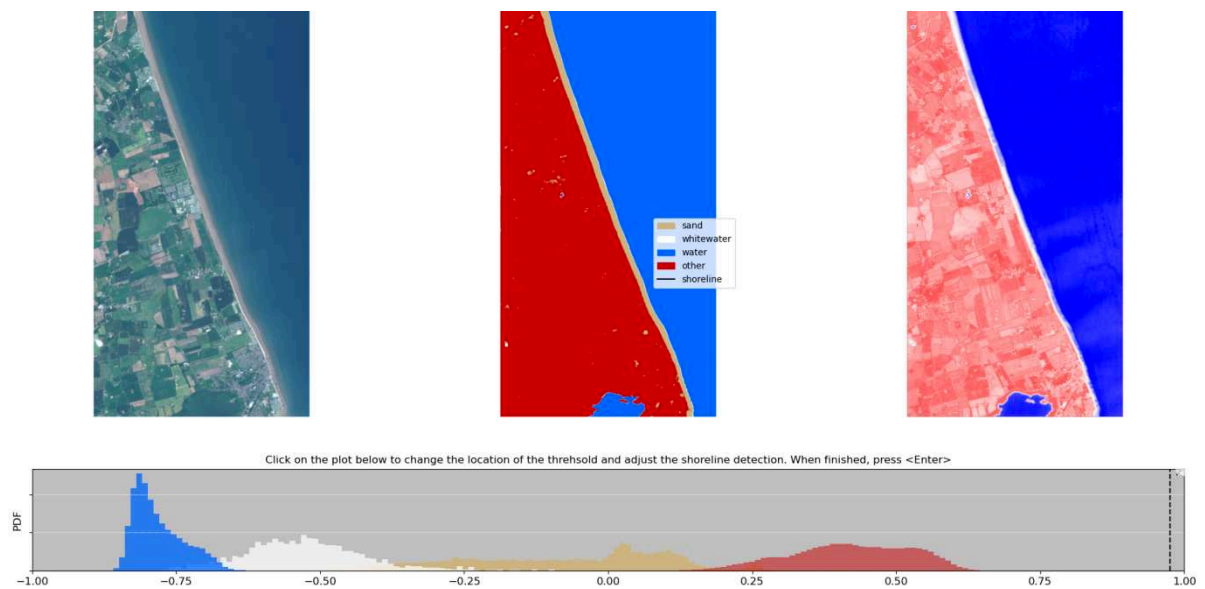
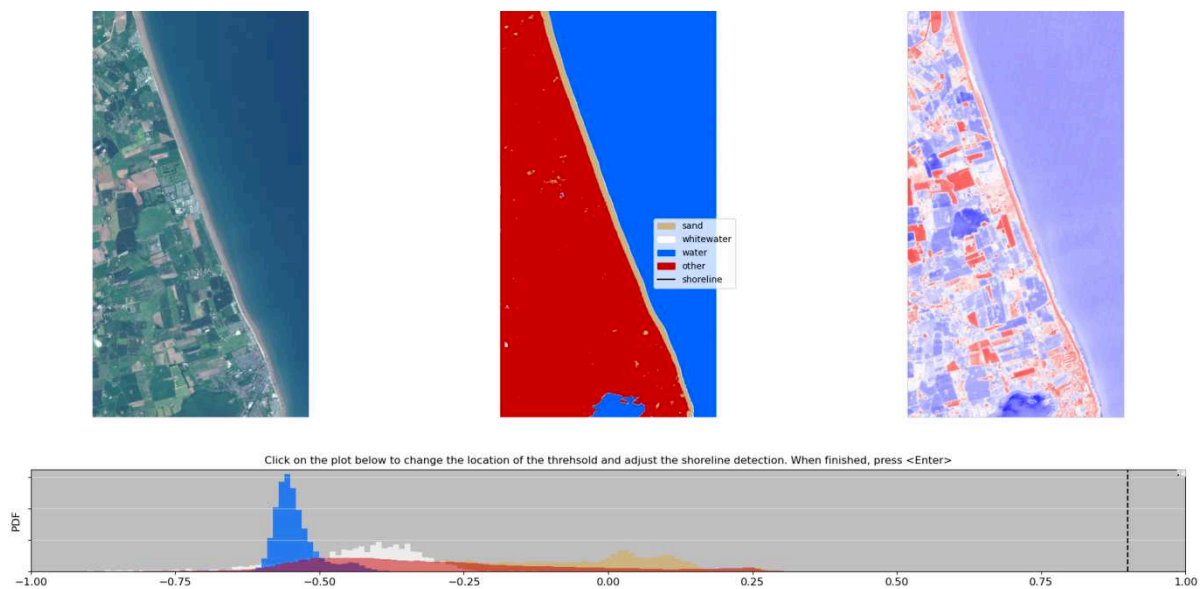
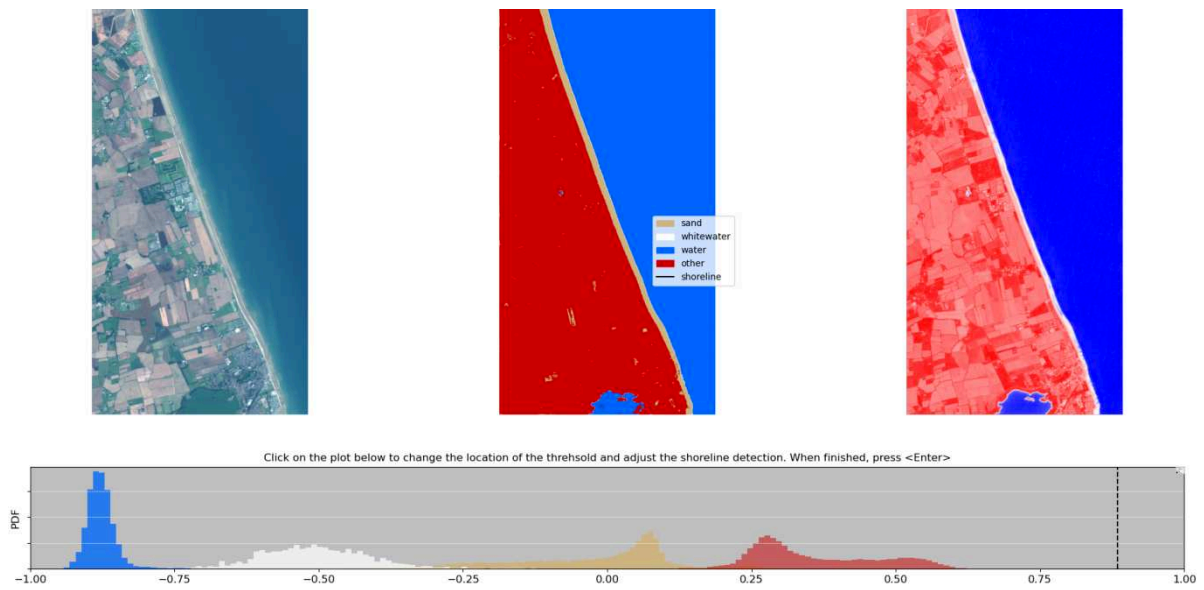
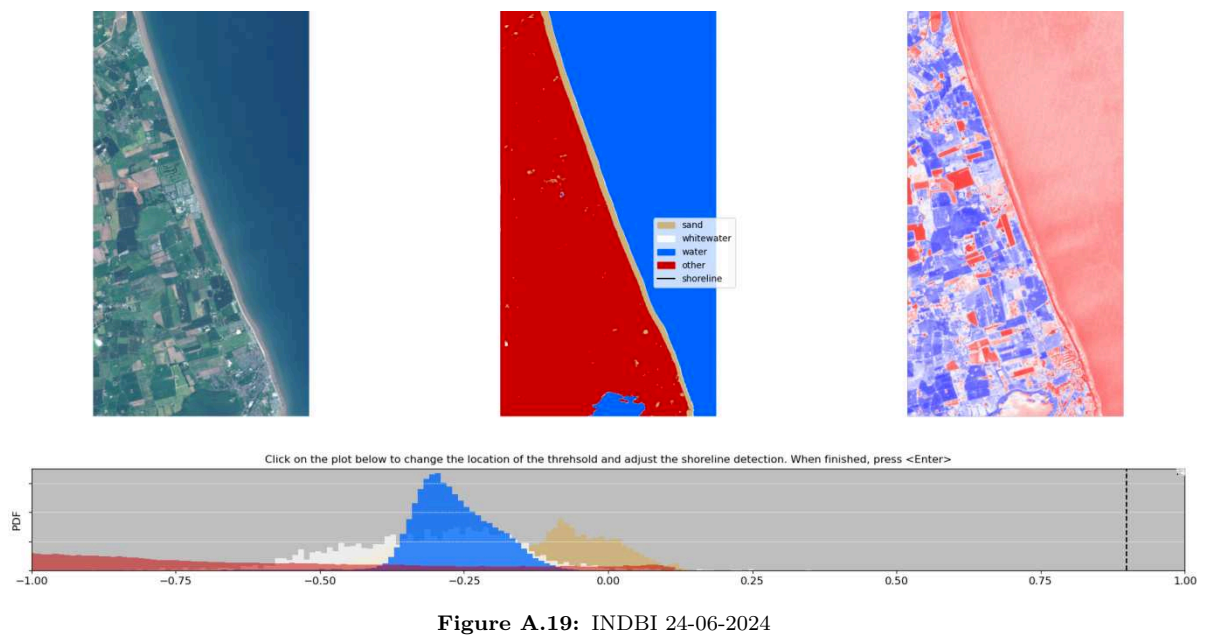
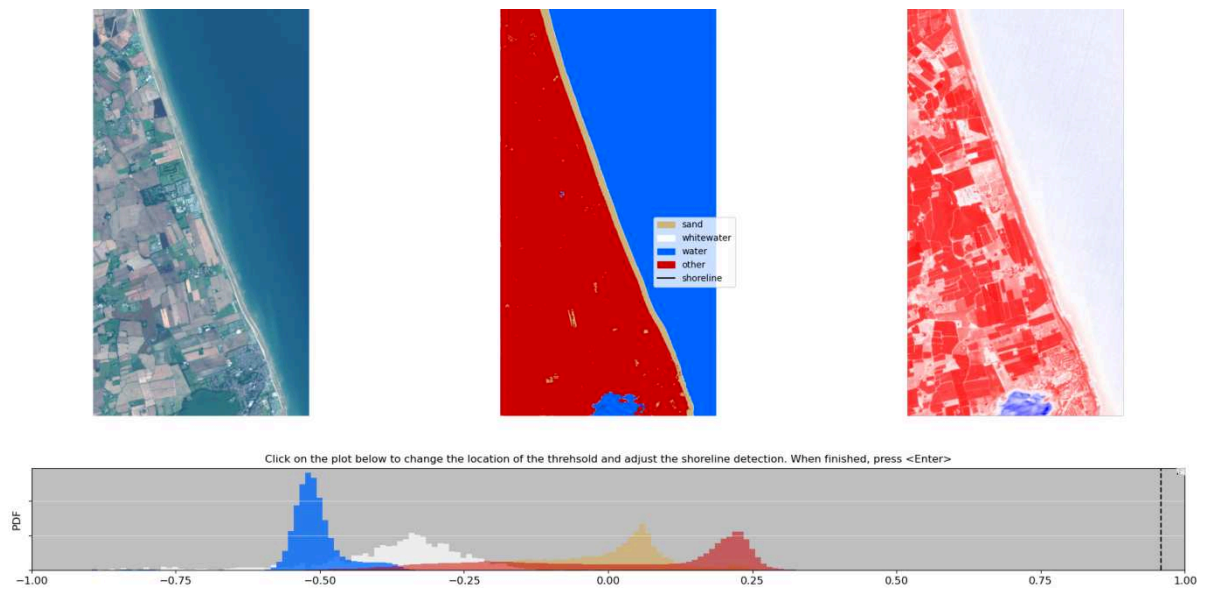


Figure A.15: SwiRed 24-06-2024





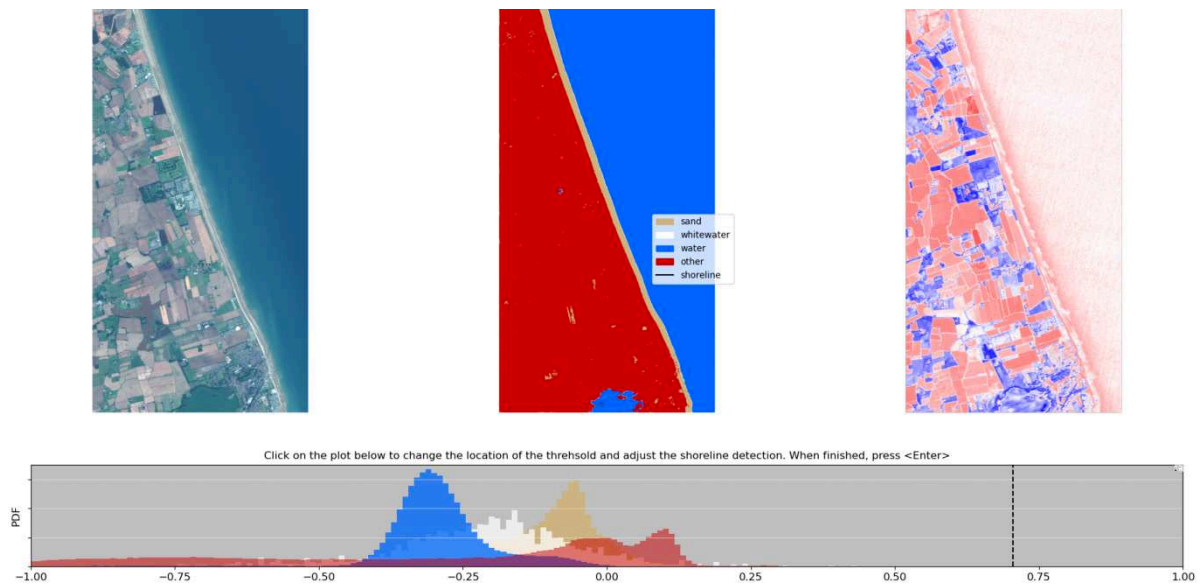


Figure A.20: INDBI 17-09-2024

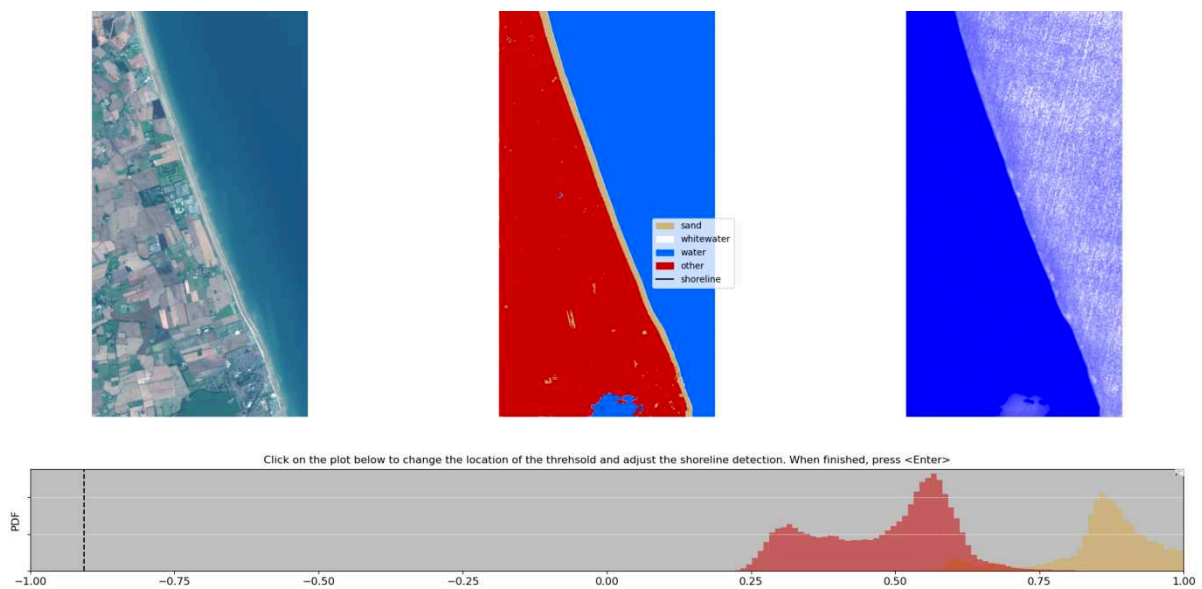


Figure A.21: BRBA 17-09-2024

B

Comparison of the indices used in CoastSat and CliffSat

In this section, the indices of CoastSat and CliffSat are compared. This is done by using both models to derive both the waterline and cliff line, and compare the output to each other.

In Figure B.1 CoastSat, using the MNDWI, is presented for detecting the waterline. In Figure B.2, the waterline is detected by CliffSat, using a combination of the NDVI and SwiRed. As visible, the waterlines found by both algorithms are comparable. This is caused by the fact that the index used in CliffSat not only separates land from sand, but also sand from water.

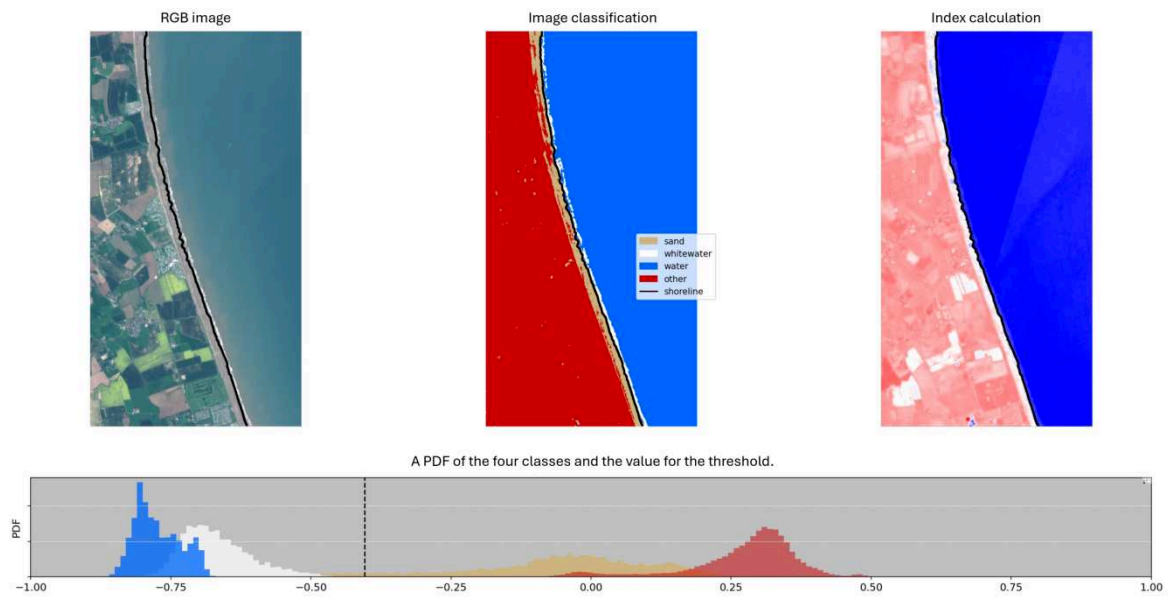


Figure B.1: An example of the waterline detection by CoastSat on 15-05-2018.

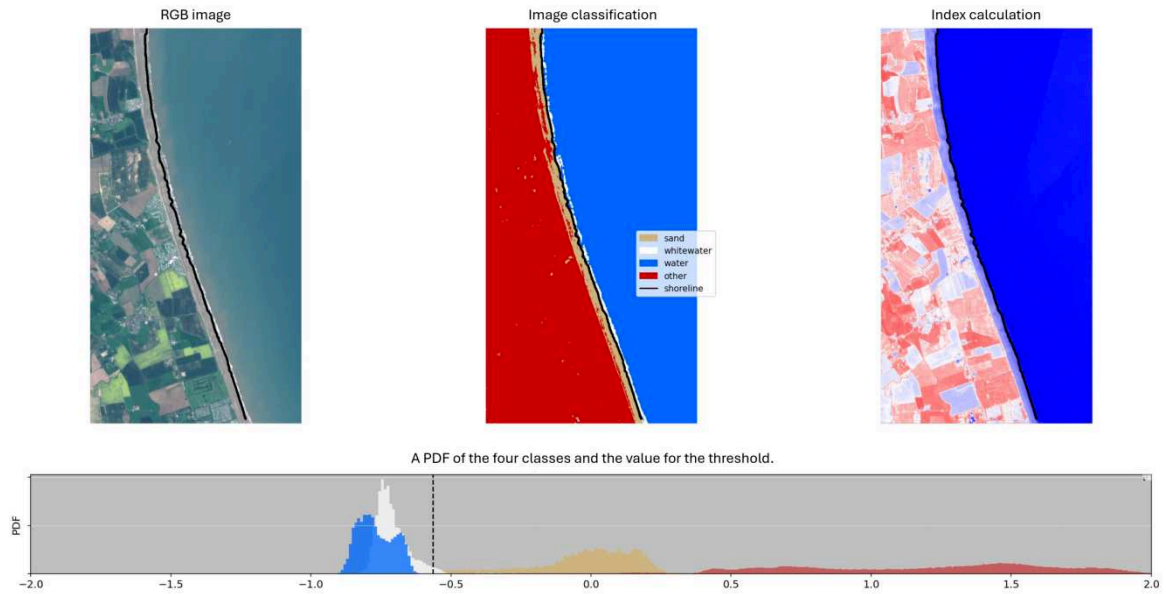


Figure B.2: An example of the waterline detection by CliffSat on 15-05-2018.

In Figure B.3, CoastSat is used to derive the cliff line, while in Figure B.4, CliffSat is used to derive the cliff line. As visible, the cliff line derived by CoastSat is not located on the actual cliff line, and there is a lot of noise present compared to the cliff line derived by CliffSat. This is due to the overlap of index values between land and sand, caused by the fact that the MNDWI is good at separating water from land, but not designed to separate land features from each other.

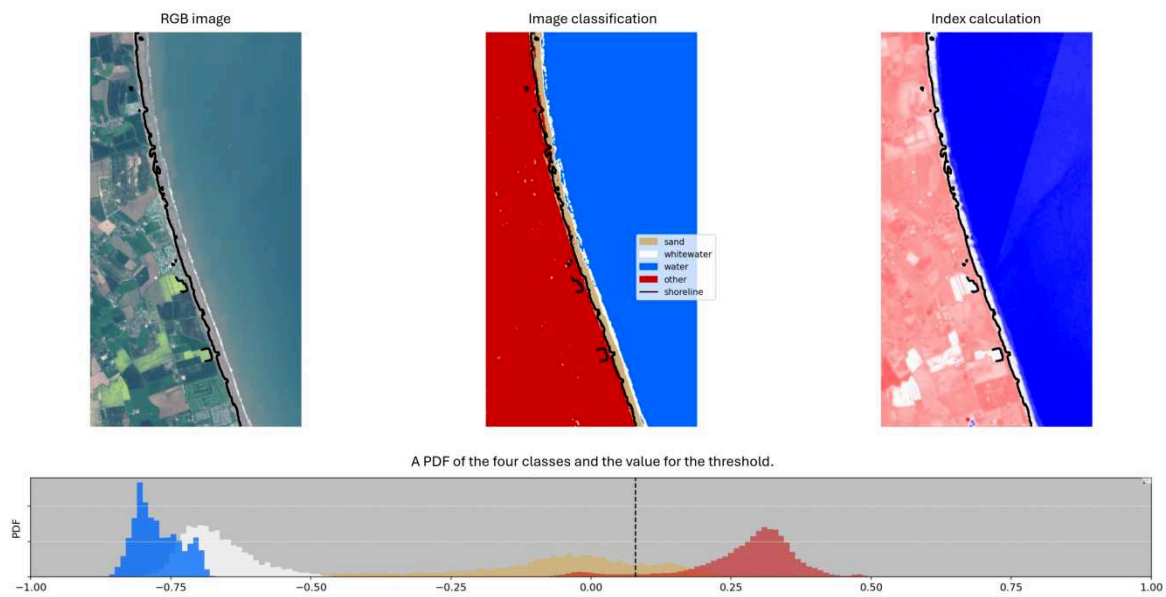


Figure B.3: An example of the cliff line detection by CoastSat on 15-05-2018.

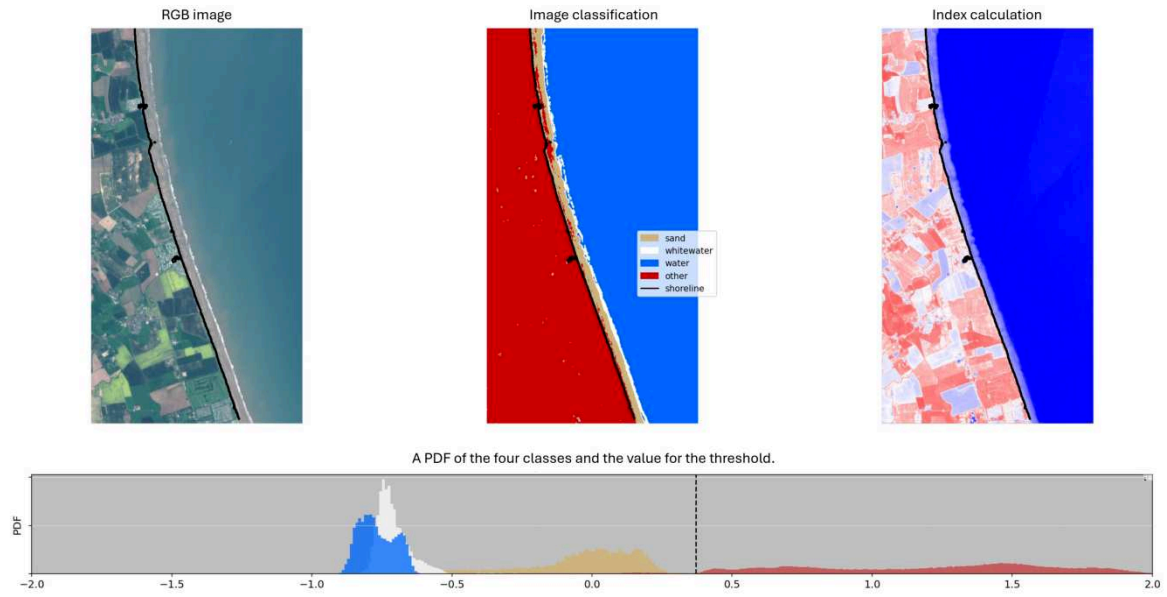


Figure B.4: An example of the cliff line detection by CliffSat on 15-05-2018.

From this can be concluded that the index used in CoastSat is only suitable to detect the waterline, where the index used in CliffSat is able to detect both the waterline as the cliff line. This proves that this newly found index is

Evaluation of thresholding methods

In this section, the error caused in the current thresholding method is evaluated. Both the reason and effects of this error is looked into, after which solutions to minimize the effects are given.

In the classification step of the algorithm, sometimes mistakes are made, and pixels are classified incorrectly. In this case, the mistake that is most often made, is that pixels from 'other' land features are classified as sand. These mistakes during the classification process influence the distribution of the sand pixels for the calculated index, as can be seen in the probability density function. An example of this is given in Figure C.1.

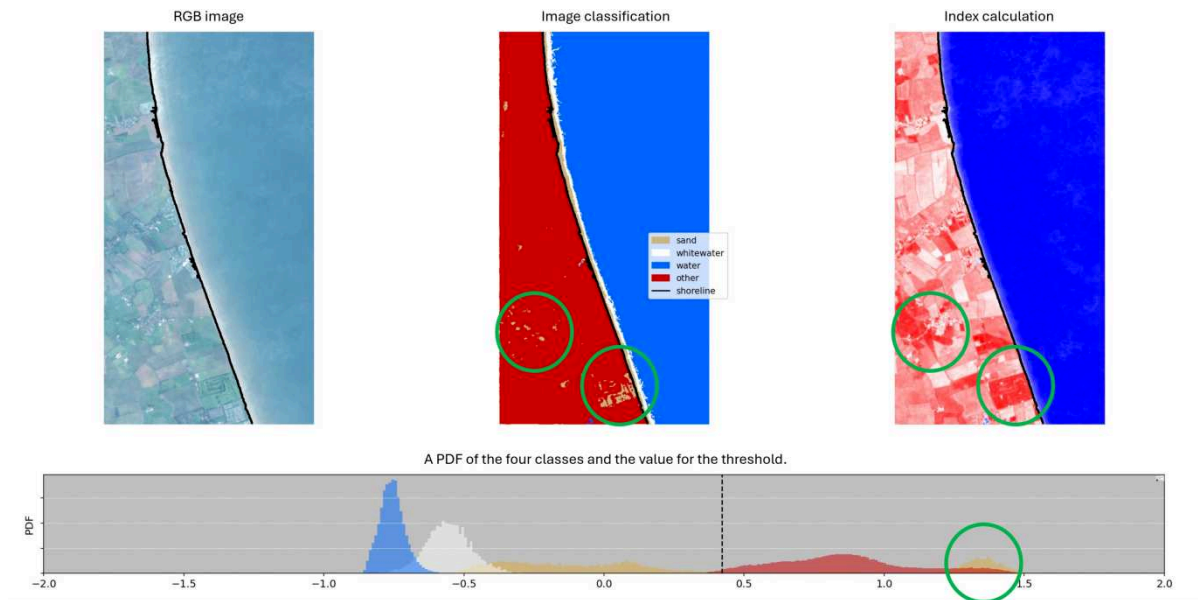


Figure C.1: An example of the threshold determination for transect 17-28 using Otsu's thresholding method, showing that the threshold found (dashed black line) has a slight error towards 'other' (shown in red) compared to sand (shown in orange), caused by the peak in the sand class around the index value 1.4.

The variance for the land and sand class, used for the threshold calculation, is influenced by this peak of sand pixels in the PDF around the value 1.4, causing the threshold to shift towards a more positive value. The result of this shift is that the cliff line is projected more landward, considering the index of land is more positive than of sand. Since this mistake in the classification process varies per image, the location of the cliff line also varies per image. This can be seen in Figure C.2

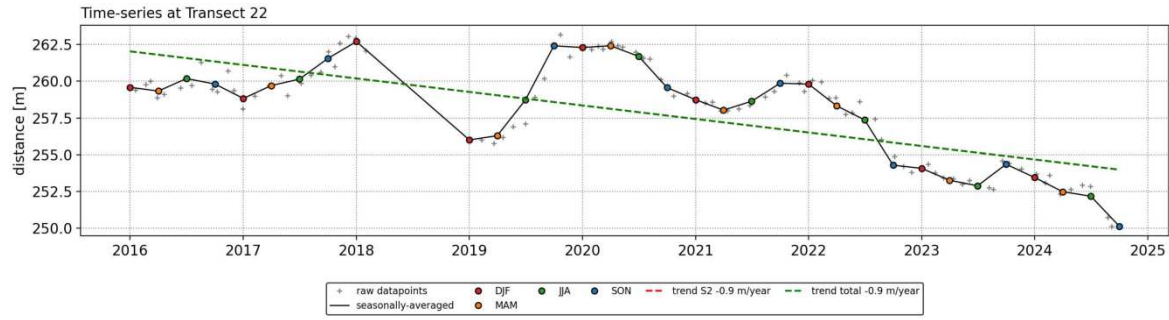


Figure C.2: An example of variability for the timeseries of transect 22 caused by the error in threshold determination.

To confirm the variability in the timeseries is caused by this error and to get an insight into the magnitude of this error, multiple images are evaluated and compared to the timeseries of a transect visible in that image. For this analysis, transect 22 was chosen to compare to, considering small erosion amounts and a high variability in the individual cliff line positions, making it a suitable transect to see if the variability is in line with the classification and thresholding error.

In Figure C.3 the timeseries of transect 22 is given, with yellow markers to show what single images are evaluated. If the variability is indeed a result from errors in the classification and threshold calculation, it will be visible that images that are underneath the trend line have more misclassified sand pixels, causing the cliff line to become more landward. If the image has a distance greater than the trend, less misclassified sand pixels should be present.

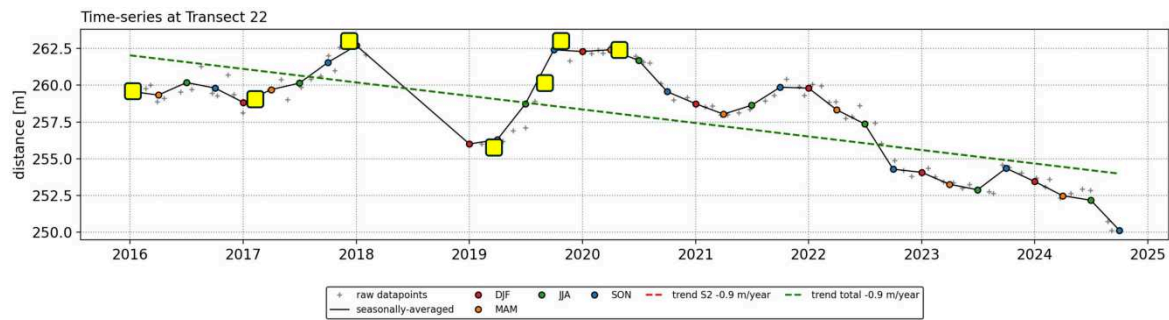


Figure C.3: An example of variability for the timeseries of transect 22 caused by the error in threshold determination, with the yellow marks representing single images that are evaluated.

If the variability is indeed caused by the error in the classification process and the subsequent threshold calculation, it is expected that the image of early 2016 and 2017 show more misclassified sand pixels than the image of late 2017. Again, the image of early 2019 should show more misclassified sand pixels than the images of late 2019 and early 2020. The same should be seen for the images of 2021 and 2022; late 2022 should contain the most wrongly classified sand pixels, compared to late 2021. Underneath, the images are presented that were used for this analysis. In green circles, the areas where the sand pixels are most often mistakenly classified are highlighted with green circles, as well as the location in the probability density function where these pixels cause a peak.

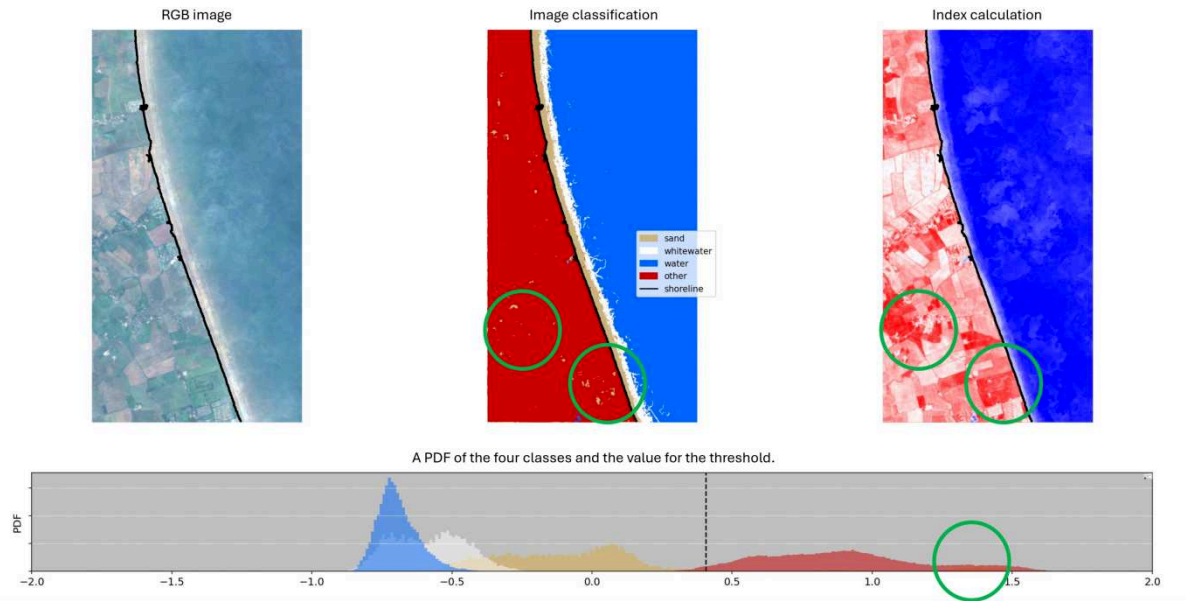


Figure C.4: A composite image of January 2016 used for finding the influence of mistakes in the classifying process, causing a variability in the timeseries.

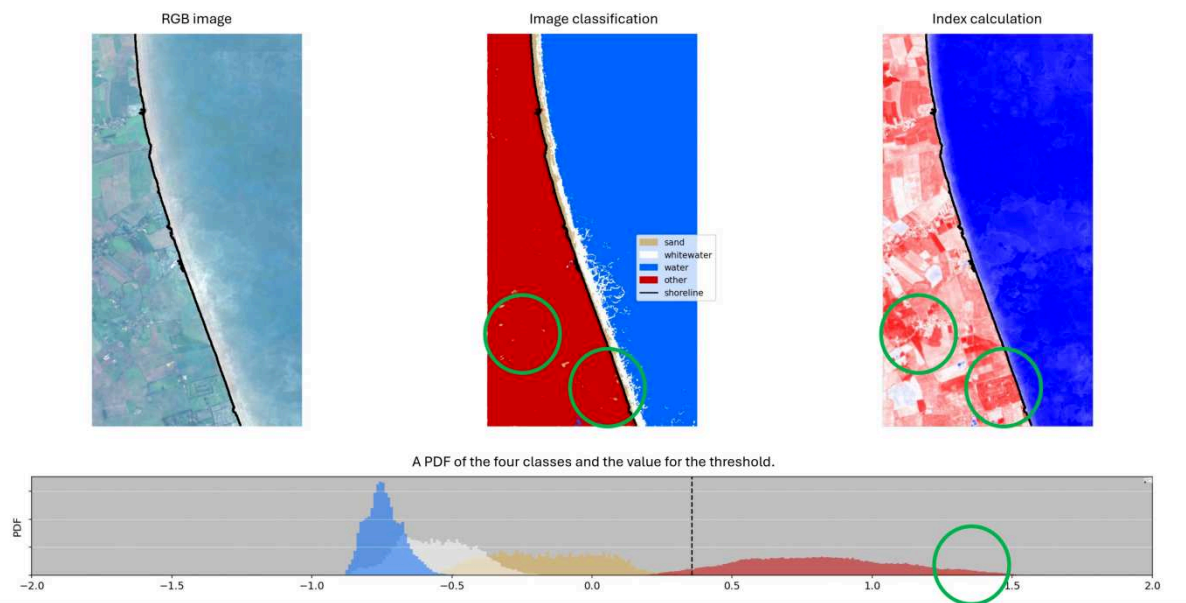


Figure C.5: A composite image of January 2017 used for finding the influence of mistakes in the classifying process, causing a variability in the timeseries.

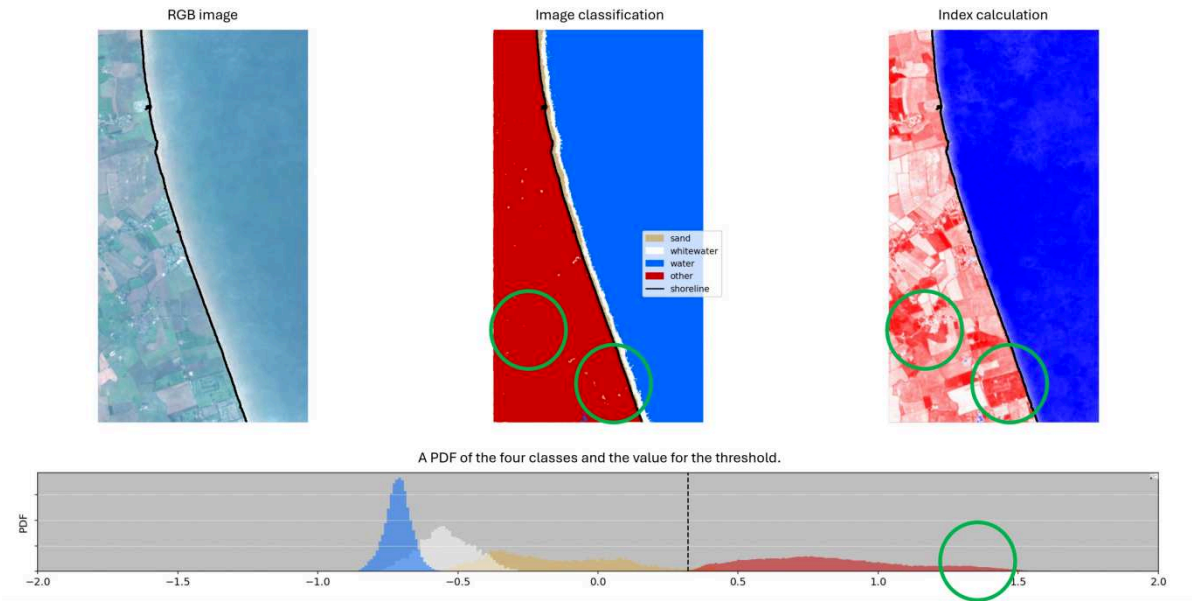


Figure C.6: A composite image of December 2017 used for finding the influence of mistakes in the classifying process, causing a variability in the timeseries.

As can be seen, there is indeed a difference in the amount of sand pixels that are classified incorrectly. Especially for the image of January 2016 (Figure C.4), there are more mistakes made during the classification process than in December 2017 (Figure C.6), showing that the variability can indeed be caused by this classification. A peak in sand pixels around an index value of 1.4 in the probability density function is not observed. It is however visible that the threshold determined for December 2017 is more in the middle between sand and 'other' than the threshold determined for both images from January.

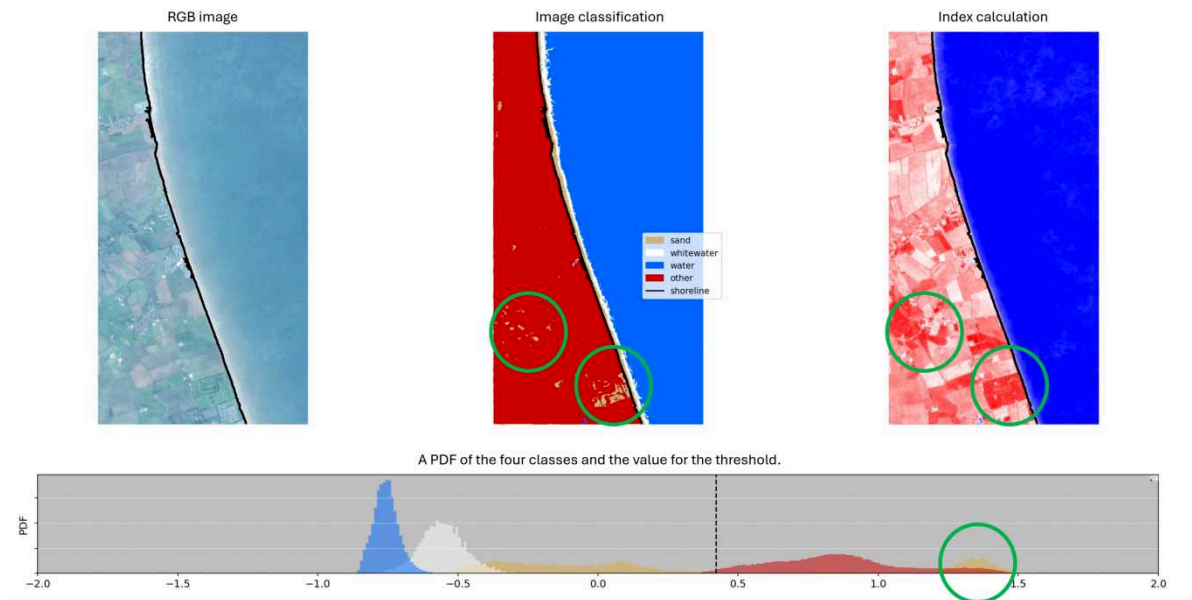


Figure C.7: A composite image of March 2019 used for finding the influence of mistakes in the classifying process, causing a variability in the timeseries.

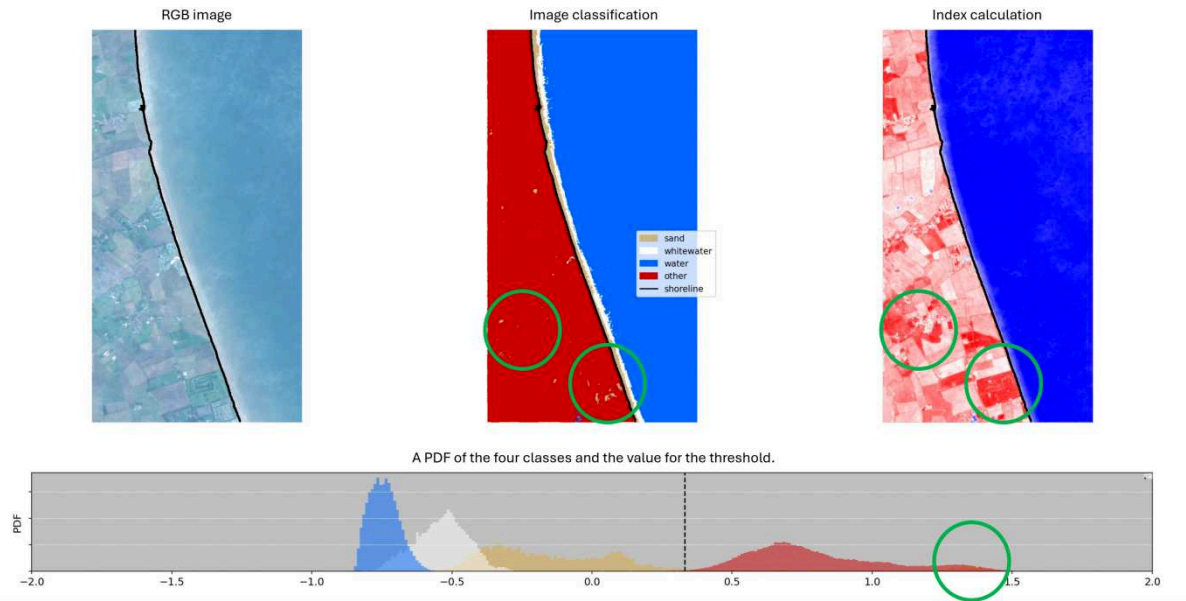


Figure C.8: A composite image of August 2019 used for finding the influence of mistakes in the classifying process, causing a variability in the timeseries.

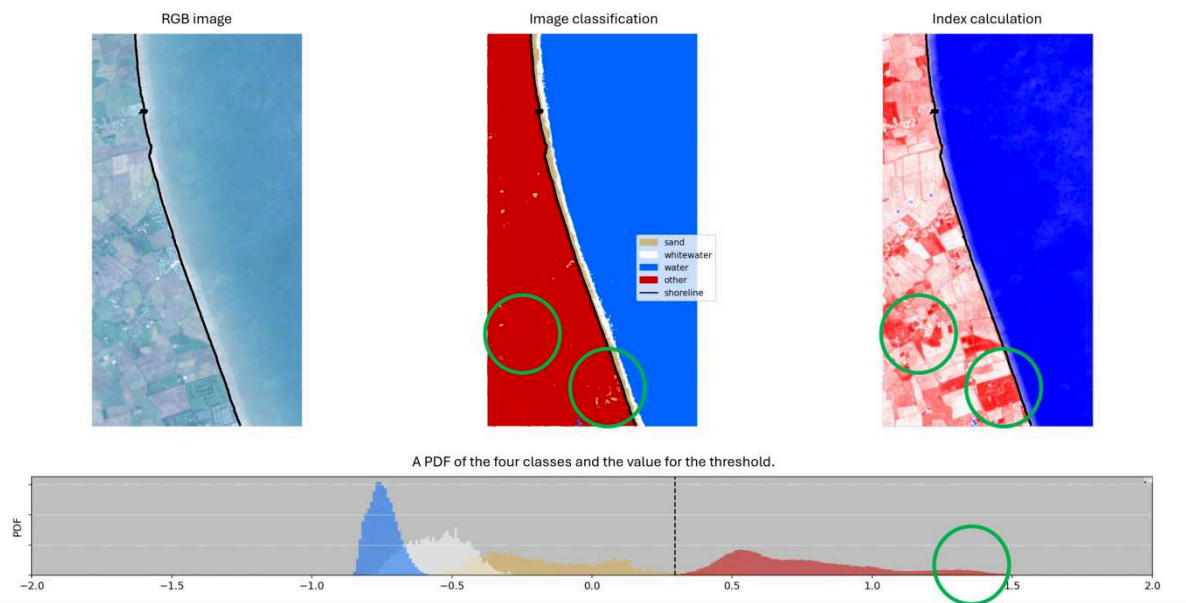


Figure C.9: A composite image of October 2019 used for finding the influence of mistakes in the classifying process, causing a variability in the timeseries.

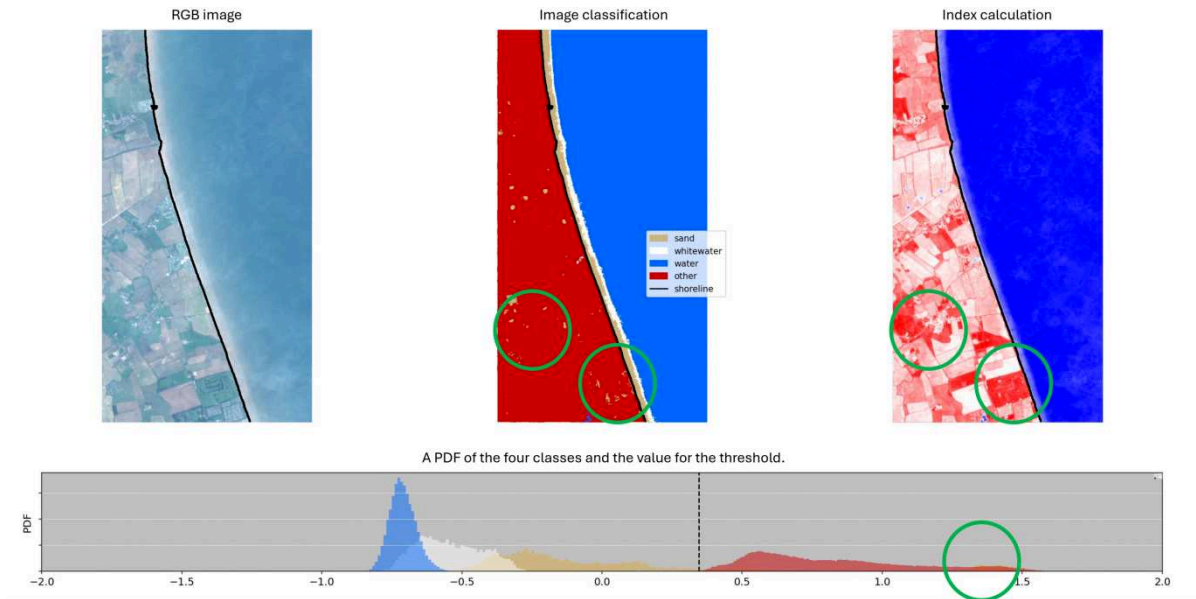


Figure C.10: A composite image of April 2020 used for finding the influence of mistakes in the classifying process, causing a variability in the timeseries.

In this series of images it can be clearly seen that the image of March 2019, presented in Figure C.7, has a lot of misclassified sand pixels. There is even a clear peak present in the probability density function, shifting the threshold to a more positive index value. In the other images, it can be seen that a lot less pixels are mistakenly classified, and it can be seen that in October 2019 (Figure C.9) the least errors are present. This is in line with the cliff line position being position the furthest away from the base point on land, as can be seen in Figure C.3.

From this evaluation can be concluded that the errors in the classification process and the subsequent thresholding calculation cause a variation for the cliff line position. The biggest difference that is observed caused by this error is less than 7.5 meters, between March and October 2019. Considering that the composite image technique causes a big difference between land and sand pictures around the cliff line, the interpolated index values between pixels have a steep transition, causing the error to be of a small magnitude. If the difference in index value between land and sand pixels near the cliff line is smaller, the error caused by this process will have a higher magnitude, as shown in Figure C.11.

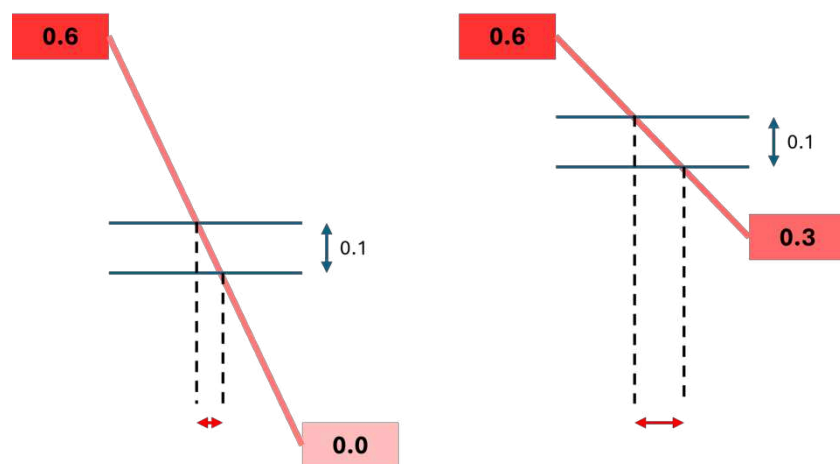


Figure C.11: A visual presentation on how the magnitude of the error is influenced by the difference in index value between pixels.

In this research, the effect of the error is limited by training classifiers for every apart region of interest, reducing the error in the classification process. It can, however, also be limited by evaluating other thresholding methods, considering there are possibly thresholding methods that are more robust for these classification errors. To make the model more robust, it is thus advised to evaluate different thresholding methods in future research.